4-6-2016

Al/Ti Nanostructured Multilayers: from Mechanical, Tribological, to Corrosion Properties

Sina Izadi
University of South Florida, sina.izadi@gmail.com

Scholar Commons Citation
Izadi, Sina, "Al/Ti Nanostructured Multilayers: from Mechanical, Tribological, to Corrosion Properties" (2016). *Graduate Theses and Dissertations.*
https://scholarcommons.usf.edu/etd/6265

Al/Ti Nanostructured Multilayers: from Mechanical, Tribological, to Corrosion Properties

by

Sina Izadi

A dissertation submitted in partial fulfillment
of the requirements for the degree of
Doctor of Philosophy in Mechanical Engineering
Department of Mechanical Engineering
College of Engineering
University of South Florida

Major Professor: Wenjun Cai, Ph.D.
Alex A. Volinsky, Ph.D.
Delcie Durham, Ph.D.
Jing Wang, Ph.D.
Andreas Muller, Ph.D.

Date of Approval:
March 21, 2016

Keywords: Nanotechnology, Nanoindentation, Residual stress, Wear, TEM

DEDICATION

This dissertation is dedicated to my parents for their endless support and sacrifice during my Ph.D. study. Their hard work, enthusiasm and resilience toward life’s difficulties was always an inspiration to me.

ACKNOWLEDGMENTS

I would like to acknowledge guidance and cooperation of staff at Nano Research and Educational Center (NREC) in University of South Florida. I want to thank NREC director, Robert Tufts, for granting access to XRD tool without any time limitation in the last two semesters of my research. I thank Dr. Yusuf Emirov for his help and guidance with FIB and TEM, Yusuf's help was definitely one of the reasons that I could maintain and run those tools for over a year without access to any technical support from FEI. I would like to thank Dr. Alex Volinsky for his insightful guidance through my graduate study in USF and specially his help with Triboindenter tool in the first year of my research.

Finally I would like to thank Dr. Wenjun Cai for her guidance through my PhD study. Starting my research in the field of mechanics of materials was not possible without her guidance, support and patience.

TABLE OF CONTENTS

LIST OF TABLES

LIST OF FIGURES

ABSTRACT

Nanostructured metallic multilayers (NMMs) are well-known for their high strength in smaller bilayer thicknesses. Six Al/Ti (NMM) with different individual layer thickness were tested for their mechanical hardness using a nanoindentation tool. Individual layer thicknesses were chosen carefully to cover the whole confined layer slip (CLS) model. Nano-hardness had a reverse relation with the square root of individual layer thickness and reached a steady state at ~ 5 nm bilayer thickness. Decreasing the layer bilayer thickness from ~ 104 nm to ~ 5 nm, improved the mechanical hardness up to ~ 101%. Residual stresses were measured using grazing incident X-ray diffraction (GIXRD). Effect of residual stress on atomic structure and dislocation propagation was then investigated by comparing the amount and type of stresses in both aluminum and titanium phases. Based on the gathered data from GIXRD scans tensile stress in Ti phases, and compressive stress in Al would increase the overall coherency of structure.

Wear rate in coatings is highly dependent on design and architect of the structure. NMM coatings are known to have much better wear resistance compare to their monolithic constituent phases by introducing a reciprocal architect. In current study wear rate of two Al/Ti NMMs with individual layer thicknesses of ~ 2.5 nm and ~ 30 nm were examined under normal loads of 30 µN, 60 µN, and 93 µN. Wears strokes were performed in various cycles of 1, 2, 3, 4 5 and 10. Wear rates were then calculated by comparing the 3D imaging of sample topology before and after tests. Nano-hardness of samples was measured pre and post each cycle of wear using a nanoindentation tool. The microstructure of samples below the worn surface was then characterized using scanning electron microscopy (SEM), transmission electron microscopy (TEM), atomic force microscopy (AFM), focus ion beam (FIB) and an optical profilometer. Orientation mapping was performed to analyze the microstructure of layers beneath the nano indents. TEM imaging from the cross section of worn samples indicated severely plastically deformed layer (SPDL) below the worn surface. Shear bands and twins are visible after wear and below the worn surface. Decreasing the layer thickness from 30 nm to 2.5 nm resulted in ~ 5 time's better wear resistance. Nanowear caused surface hardening which consequently increased nano hardness up to ~ 30% in the sample with 2.5 nm individual layer thickness.

Increasing the interfaces density of NMMs will significantly improve the corrosion resistance of coating. Reciprocal layers and consequently interfaces will block the path of aggressive content toward the substrate. Corrosion rate evolution of Al/Ti multilayers was investigated through DC corrosion potentiodynamic test. Results seem to be very promising and demonstrate up to 30 times better corrosion resistance compared to conventional sputtered monolithic aluminum. Corrosion started in the form of pitting and then transformed to the localized galvanic corrosion. Decreasing the bilayer thickness from ~ 10.4 nm to ~ 5 nm will decrease the corrosion current density (i_{corr}) of ~ 5.42×10^{-7} (A/cm^2) to ~ 6.11×10^{-10} (A/cm^2). No sign of corrosion has been seen in the sample with ~ 2.5 nm individual layer thickness. Further AFM and TEM analysis from surface and cross section of NMMs indicate that a more coherent layer by layer structure improves the corrosion rate. Interfaces have a significant role in blocking the pores and imperfections inside coating.

CHAPTER 1: AN INTRODUCTION ON NMMS

1.1 Background

The concept of creating a composite material with superior mechanical, physical, and corrosion properties than its constituent materials is as old as the history [1]. Concrete is a good example; singular cement and aggregates have limited strength under compression but mixing appropriate portion of water with them can significantly improve the final product strength [2]. This concept of mixing component to favorably manipulate their properties and characteristics is not limited to bulk materials, it can also come from micro and nanoscale modifications of atoms and grains of materials [2].

Nanostructured metallic multilayers (NMMs) are examples of such nanoscale modified materials which are wildly used in numerous fields as coatings for their excellent corrosion, scratch and wear resistance [3-10]. An important factor which contributes to such good property enhancement is that atoms are placed next to each other in an organized way to react to external stresses [11]. Figuring out that how different layering materials with different structures respond to mechanical and chemical tests at micron and sub-micron scales will facilitate the understanding of their behaviors at the macroscale.

It has been shown that metallic composite multilayers demonstrate better mechanical and chemical properties compared to their monolithic ingredients [6, 12, 13]. For example, Clemens et al. [8] showed that decreasing the individual layer thickness from 50 nm to 2.5 nm will increase the hardness of Al/Nb NMM from ~ 3.1 GPa to ~ 4.5 GPa. Although there have been several studies reporting the mechanical properties of NMMs composed of alternating face centered cubic (fcc/fcc) [14-16], body centered cubic / face centered cubic (bcc/fcc) [17] and hexagonal close packing (hcp/hcp) structures [18], limited research has been performed on fcc/hcp NMMs [19, 20]. In this thesis, we chose Al/Ti as a model system to study the structure-sensitive mechanical, tribological, and corrosion properties of fcc/hcp NMMs. The reasons for choosing aluminum and titanium as the ingredient phases in this research can be summarized as the following:

- Relatively low density of aluminum (~2.7 g/cm^3) and titanium (~ 4.5 g/cm^3), which results in an overall light composite. As a comparison, titanium which is the stiffer phase in Al/Ti multilayer specimen, has a density as low as ~1/5 of tungsten (ρ ~ 19.25 g/cm^3) in Cu/W , ~ 1/2 of nickel (ρ ~ 8.9 g/cm^3) in Cu/Ni and ~ 0.7 of vanadium (~6.11 g/cm^3) in V/Ag NMMs. It is worth mentioning that aluminum, the softer component of Al/Ti NMM, also has significantly smaller density compared to other well-studied NMMs [14-17, 21-24], with the exception of magnesium in Mg/Ti NMM [18].
- Both single phase aluminum and titanium exhibits very good corrosion resistance in their bulk form. In addition, they exhibit very similar electrode potential (-1.628 V for Ti^{2+} and -1.662 V for Al^{3+}), which is likely to minimize galvanic coupling in the Al/Ti multilayered structure.
- Finally there has been very limited research on Al/Ti NMMs, many of which primarily focus on describing only phase change [25] and structural [26] or mechanical aspects [27] of the composite while a systematic study is lacking.

1.2 Deformation Mechanisms of NMMs

The layer by layer structure of NMMs can significantly improve mechanical properties by controlling the type and amount of dislocations through interface barrier strength [21, 22]. Another important parameter along with interface that also affects the type of dislocations inside layers is the individual layer thickness of NMM [21]. Different types of dislocation can occur under external stresses based on different individual layer thickness. Basically individual layer thickness controls the population of dislocations and their propagation direction while the interface controls their path through adjacent layers. As an example, when an individual layer thickness of an NMM is thick enough to contain all dislocation from external stress, then material mechanical response is very similar to monolithic sample. Decreasing the individual layer thickness to a few nanometers will decrease the possibility of multiple chain dislocations by adding the interface barriers strength (IBS) which can block dislocations through adjacent layer or redirect them through interface of adjacent layers. It is generally accepted [22, 28, 29] that three different deformation modes may operate depending on the layer thickness h. When h is at submicron length scales, dislocations pile up against the interfaces and the Hall-Petch hardening model applies, where the strength increases with decreasing layer thickness as $H \propto h^{-1/2}$. Hall-petch model is usually defined as:

$$H = H_0 + kh^{-1/2} \tag{1}$$

where H is the material hardness, H_0 is the intercept point with y axis on H vs. $h^{-1/2}$ plot. k is Hall-Petch slope obtained from fitting the linear section of data points. k can also be calculated as:

$$k = \sqrt{\frac{\tau * \mu b}{\pi(1-\upsilon)}} \tag{2}$$

where τ^* is the interface barrier strength, μ is the shear module, b is the burgers vector, and υ is the Poisson's ratio. When h is from a few to a few tens of nanometers, there is insufficient spacing between the interfaces for dislocation pile-up; thus, Hall-Petch hardening breaks down. The deformation mechanism now involves the motion of single dislocation bowing between the interfaces, where the confined layer slip (CLS) mechanism operates. In this regime, the yield strength is found to increase with decreasing layer thickness as $\sigma \propto \ln(h)/h$ [22]. The stress reaches a maximum value at approximately $h \approx 4$ nm. After that, deformation mechanisms of NMMs become insensitive to layer thickness but highly sensitive to the structure and property of interfaces, as they represent a large volume fraction with decreasing layer thicknesses. For NNMs with coherent interfaces, such as Cu/Ni multilayers, strength depends on the coherency strains, and the maximum flow stress is equal to the coherency stress. For NNMs with incoherent interfaces, the deformation mode is associated with the transmission of single glide dislocation across interfaces [30]. While Hall-Petch and CLS models cannot predict the strength at smaller layer thickness, Misra et al. [22] suggested a modified CLS model which can predict the shear stress required to cause plastic deformation through a single dislocation. Fig 1.1 indicates three different typical dislocation regimes for NMM structures. Dislocation happens inside the softer/ductile layer and then propagates to the interfaces of adjacent layers from sides. The CLS stress is estimated as:

$$\tau_{cls} = M\frac{\mu b}{8\pi h'}\left(\frac{4-\nu}{1-\nu}\right)\left[\ln\frac{\alpha h'}{b}\right]-\frac{f}{h}+\frac{C}{\lambda}, \text{ and } C=\frac{\mu b}{(1-\nu)} \qquad (3)$$

where M is the Taylor factor (~ 3.1), μ is the shear modulus, b is the Burgers vector, h′ is the layer thickness measured parallel to the slip plane (~ h × ($\frac{1}{\cos 30}$)), f is the interface stress which has a typical value between 2 - 3 [J.m^{-2}] [18]. The core cut-off parameter α, and the spacing of the interface dislocation array λ, are two unknown parameters which can be found by fitting the experimental results. Misra et al. [22] suggested that using the H-P slope, k, it is possible to find maximum interface barrier strength (IBS) with following equation for NMFs:

$$\sigma_{IBS} = 3.06\ \tau^{*}. \tag{4}$$

Interface crossing stress or interface barrier strength (σ_{IBS}) is in fact the ultimate required stress for occurrence of any types of dislocations in NMMs. In other words all other types of dislocation including pile ups and hairpins (through CLS model) will occur at smaller stresses. Although CLS model is a good estimation of material strength, it however overlooks some important factors including elastic anisotropy and residual stress in the layers [22].

One of the important parameters which has proven to affect overall strength of NMM specimens but is usually overlooked is residual stress. Effect of residual stress on some types of multilayers with a few to dozens of layers had been previously studied [31-33]. These studies indicate a direct relationship between the amounts of compressive residual stress in deposited thin films and final material strength. It is possible to measure the amount of residual stress in crystal structure by XRD scan of specimen surface in various Ψ angles. Ψ is the angle between incident-diffracted bisector with the normal of sample surface, where Ψ rotation plane is also perpendicular to the normal of sample surface. It is possible to estimate the residual stress σ of thin films using several XRD scans through following equation:

$$\sigma = \left(\frac{d\Psi - d0}{d0}\right) \times \frac{E}{1+\upsilon} \times \frac{1}{\sin^2 \Psi} \tag{5}$$

where d_0 is the lattice parameter at $\Psi = 0$, d_Ψ is the measured d spacing when sample is tilted at Ψ, E is elastic modulus, and υ is the Poisson's ratio.

1.3 Nanowear Behavior of NMMs

Wear resistance is a system's response rather than a material property [34]. Wear rate is usually high at the beginning of the wear process and then reaches a steady state [34]. Wear mechanism can be categorized in different types including mechanical, chemical and thermal wear. Mechanical wear, which is the focus of this study, includes abrasive, adhesive and fatigue wear.

The parameters which can affect wear rate are numerous: environment, temperature [35], humidity [36], and sliding velocity, just to name a few. Thousands of studies on wear properties of material have been done and several definitions and theories have been proposed to determine wear rate. One of the most well-known methods was proposed by Archard [37] defining the wear rate (w) as:

$$\mathrm{w} = \mathrm{K} \times \frac{L}{H}, \tag{6}$$

where K is the wear coefficient, L is the normal load, and H is the material hardness. Archard's theory thus predicts a linear relationship between normal load and wear rate, as shown in Fig.1.2. Based on the type of wear, material properties of the region below wear surface can change and structure can deform. This deformation can be seen in the form of shear bands, twins, voids etc. Due to their excellent mechanical properties, NMMs often exhibit exceptional wear resistance [38]. The coating architecture, number of layers and layer thickness of NMMs can significantly affect wear rate of the structure [39]. One study [40] shows that a bilayer of TiC and WC/C coating can reduce the wear rate of Ti-6Al-4V up to 94%. Yang et al. [39] showed that in Al-N/Cr-N NMMs by switching the top layers from Al-N to Cr-N friction coefficient and wear rate of coating will be increased significantly, which shows how wear is dependent on design and architecture rather than the material. Yonekura et al. [41] indicated that multilayer structure will improve both wear and fatigue resistance but increasing the individual layer thickness will reduce the improvement rate. It has been proven that wear rate is strongly related to material overall strength [40]. Generally a sample with higher hardness to elastic module ratio (H/E) will demonstrate better wear rate. Some of the typical deformations below the worn surface of NMMs include compression of layers, crack propagation along columnar boundaries [42], and shear bands and twins formation [43].

1.4 Corrosion Resistance of NMMs

Corrosion resistance of multilayers has been found to be significantly higher than their constituent monolithic specimens in several studies [5, 9, 44]. In passive metals such as aluminum, good corrosion resistance can be achieved by creating dense microstructure with low porosity [3]. If a multilayer structure facilitates such a structure with appropriate chemical composition [45], then it can delay the corrosion process. Hovsepian et al. [45] indicates that CrN/NbN multilayer shows significantly better corrosion protection compared to its monolithic constituent because of less interconnecting pores and defects through the coating. In the case of Al/Ti NMMs, Xie et al. [44] demonstrated that it is possible to decrease current density of corrosion by two orders of magnitude in an NMM with less than 50 bilayers. This improvement in corrosion rate was made possible by keeping the titanium layers thickness at 50 nm and decreasing the aluminum thickness from 1265 nm to 200 nm. On another study of Al/Ti multilayer coating, Charrier et al. [4] concluded that corrosion resistance is improved only if the titanium is the external layer of the coating. In addition, these authors pointed out that titanium cannot improve the corrosion rate in monolithic form and aluminum will play sacrificial protection role.

While several groups [46, 47] have attempted to simulate the oxidation and corrosion process of nanostructures through molecular dynamics (MD), corrosion rate can be easily measured through a controlled potential polarization test. Figure 1.3 indicates the current vs. voltage polarization curve after a typical potentiodynamic test. If an anodic reaction metal X is simplified as

$$X = X^{n+} + ne^{-}, \qquad (7)$$

the current density and corroded mass of the specimen are related to each other through Faradaic conversion formula as

$$W = \frac{I \times t \times M}{n \times F} \tag{8}$$

W is the mass lost or gained, M is the atomic mass of metal, n is the valance of metal, , F=96485 [coulombs/mole] is the Faraday's constant, and t is the length of time that current was on. I or current in Faradays equation has the unit of Amps, which can be converted to current density by dividing current over the samples cross section area.

The goals of this research are to synthesis and characterize Al/Ti NMMs, establish a relationship between the microstructure evolutions, mechanical, tribological, and corrosion responses as a function of layer thickness. In the current work, various Al/Ti NMMs with individual layer thickness from 2.5 to 52 nm are characterized and studied. Mechanical properties along with residual stress of Al/Ti NMMs is analyzed and discussed in Chapter 2; nano wear and its effect on microstructure evolution of NMM is studied in Chapter 3; and finally corrosion resistance of different Al/Ti NMMs has been studied in Chapter 4.

1.5 References

1. Koehler, J.S., *Attempt to Design a Strong Solid.* Physical Review B, 1970. **2**(2): p. 547-551.

2. Kang, S.H., et al., *Effect of sand grain size and sand-to-cement ratio on the interfacial bond strength of steel fibers embedded in mortars.* Construction and Building Materials, 2013. **47**: p. 1421-1430.

3. Barshilia, H.C., et al., *Corrosion behavior of nanolayered TiN/NbN multilayer coatings prepared by reactive direct current magnetron sputtering process.* Thin Solid Films, 2004. **460**(1–2): p. 133-142.

4. Charrier, C., et al., *Aluminium and Ti/Al multilayer PVD coatings for enhanced corrosion resistance.* Surface and Coatings Technology, 1997. **90**(1–2): p. 29-34.

5. Creus, J., et al., *Mechanical and corrosion properties of dc magnetron sputtered Al/Cr multilayers.* Surface and Coatings Technology, 2008. **202**(16): p. 4047-4055.

6. Liu, C., et al., *Effects of Ti/TiN multilayer on corrosion resistance of nickel–titanium orthodontic brackets in artificial saliva.* Corrosion Science, 2007. **49**(10): p. 3783-3796.

7. Chan, Y.-C., et al., *Texture, microstructure and anti-wear characteristics in isostructural CrAlSiN/W2N multilayer coatings.* Thin Solid Films, 2013. **544**: p. 265-269.

8. Clemens, B.M., H. Kung, and S.A. Barnett, *Structure and Strength of Multilayers.* MRS Bulletin, 1999. **24**(02): p. 20-26.

9. Guan, X., et al., *Toward high load bearing capacity and corrosion resistance Cr/Cr2N nano-multilayer coatings against seawater attack.* Surface and Coatings Technology, 2015. **282**: p. 78-85.

10. Economy, D.R., et al., *Identifying Deformation and Strain Hardening Behaviors of Nanoscale Metallic Multilayers Through Nano-wear Testing.* Metallurgical and Materials Transactions A, 2016. **47**(3): p. 1083-1095.

11. Wang, J., et al., *Atomistic modeling of the interaction of glide dislocations with "weak" interfaces.* Acta Materialia, 2008. **56**(19): p. 5685-5693.

12. Misra, A. and H. Krug, *Deformation Behavior of Nanostructured Metallic Multilayers.* Advanced Engineering Materials, 2001. **3**(4): p. 217-222.

13. Izadi, S., H. Mraied, and W. Cai, *Tribological and mechanical behavior of nanostructured Al/Ti multilayers.* Surface and Coatings Technology, (0).

14. Zhang, J.Y., et al., *Mechanical properties of fcc/fcc Cu/Nb nanostructured multilayers.* Materials Science and Engineering: A, 2012. **545**: p. 118-122.

15. Yu, K.Y., et al., *Strengthening mechanisms of Ag/Ni immiscible multilayers with fcc/fcc interface.* Surface and Coatings Technology, 2013. **237**: p. 269-275.

16. McKeown, J., et al., *Microstructures and strength of nanoscale Cu–Ag multilayers.* Scripta Materialia, 2002. **46**(8): p. 593-598.

17. Misra, A., R.G. Hoagland, and H. Kung ‡, *Thermal stability of self-supported nanolayered Cu/Nb films.* Philosophical Magazine, 2004. **84**(10): p. 1021-1028.

18. Lu, Y.Y., et al., *The microstructure and mechanical behavior of Mg/Ti multilayers as a function of individual layer thickness.* Acta Materialia, 2014. **63**: p. 216-231.

19. Zhang, B., K.M. Krishnan, and R.F.C. Farrow, *Crystallography of Co/Pt multilayers and nanostructures.* Ultramicroscopy, 1993. **51**(1): p. 298-305.

20. Ahuja, R. and H.L. Fraser, *Structure and mechanical properties of nanolaminated Ti-Al thin films.* JOM. **46**(10): p. 35-39.

21. Fu, E.G., et al., *Mechanical properties of sputtered Cu/V and Al/Nb multilayer films.* Materials Science and Engineering: A, 2008. **493**(1–2): p. 283-287.

22. Misra, A., J.P. Hirth, and R.G. Hoagland, *Length-scale-dependent deformation mechanisms in incoherent metallic multilayered composites.* Acta Materialia, 2005. **53**(18): p. 4817-4824.

23. Wei, Q.M., et al., *Suppression of irradiation hardening in nanoscale V/Ag multilayers.* Acta Materialia, 2011. **59**(16): p. 6331-6340.

24. Chen, Y., et al., *Microstructure and strengthening mechanisms in Cu/Fe multilayers.* Acta Materialia, 2012. **60**(18): p. 6312-6321.

25. Banerjee, R., et al., *Phase stability in Al/Ti multilayers.* Acta Materialia, 1999. **47**(4): p. 1153-1161.

26. Shechtman, D., D. van Heerden, and D. Josell, *fcc titanium in Ti-Al multilayers.* Materials Letters, 1994. **20**(5): p. 329-334.

27. Levashov, E.A., et al., *Multilayer nanostructured heat-generating coatings. Preparation and certification of mechanical and tribological properties.* Metallurgist, 2011. **54**(9-10): p. 623-634.

28. Misra, A., et al., *Deformation mechanism maps for polycrystalline metallic multiplayers.* Scripta Materialia, 1999. **41**(9): p. 973-979.

29. Misra, A. and H. Kung, *Deformation behavior of nanostructured metallic multilayers.* Advanced Engineering Materials, 2001. **3**(4): p. 217-222.

30. Wang, J. and A. Misra, *An overview of interface-dominated deformation mechanisms in metallic multilayers.* Current Opinion in Solid State & Materials Science, 2011. **15**(1): p. 20-28.

31. Labat, S., et al., *Interdependence of elastic strain and segregation in metallic multilayers: An x-ray diffraction study of (111) Au/Ni multilayers.* Journal of Applied Physics, 2000. **87**(3): p. 1172-1181.

32. Berger, S. and F. Spaepen, *The Ag/Cu interface stress.* Nanostructured Materials, 1995. **6**(1–4): p. 201-204.

33. Bain, J.A., et al., *Elastic strains and coherency stresses in Mo/Ni multilayers.* Physical Review B, 1991. **44**(3): p. 1184-1192.

34. Kato, K., *Classification of Wear Mechanisms/Models*, in *Wear – Materials, Mechanisms and Practice*. 2005, John Wiley & Sons Ltd. p. 9-20.

35. Gåård, A., et al., *Temperature effects on adhesive wear in dry sliding contacts.* Wear, 2010. **268**(7–8): p. 968-975.

36. Lancaster, J.K., *A review of the influence of environmental humidity and water on friction, lubrication and wear.* Tribology International, 1990. **23**(6): p. 371-389.

37. Archard, J.F., *Contact and Rubbing of Flat Surfaces.* Journal of Applied Physics, 1953. **24**(8): p. 981-988.

38. Abdolrahim, N., H.M. Zbib, and D.F. Bahr, *Multiscale modeling and simulation of deformation in nanoscale metallic multilayer systems.* International Journal of Plasticity, 2014. **52**: p. 33-50.

39. Yang, Y.-S., T.-P. Cho, and Y.-C. Lin, *Effect of coating architectures on the wear and hydrophobic properties of Al–N/Cr–N multilayer coatings.* Surface and Coatings Technology, 2014. **259, Part B**: p. 172-177.

40. Pawlak, W., et al., *Wear resistant multilayer nanocomposite WC1−x/C coating on Ti–6Al–4V titanium alloy.* Tribology International, 2015. **82, Part B**: p. 400-406.

41. Yonekura, D., J. Fujita, and K. Miki, *Fatigue and wear properties of Ti–6Al–4V alloy with Cr/CrN multilayer coating.* Surface and Coatings Technology, 2015. **275**: p. 232-238.

42. Tsai, Y.-Z. and J.-G. Duh, *Tribological behavior of CrAlSiN/W2N multilayer coatings deposited by DC magnetron sputtering.* Thin Solid Films, 2010. **518**(24): p. 7523-7526.

43. Izadi, S., H. Mraied, and W. Cai, *Tribological and mechanical behavior of nanostructured Al/Ti multilayers.* Surface and Coatings Technology, 2015. **275**: p. 374-383.

44. Xie, T., et al., *Structure, corrosion, and hardness properties of Ti/Al multilayers coated on NdFeB by magnetron sputtering.* Vacuum, 2012. **86**(10): p. 1583-1588.

45. Hovsepian, P.E., D.B. Lewis, and W.D. Münz, *Recent progress in large scale manufacturing of multilayer/superlattice hard coatings.* Surface and Coatings Technology, 2000. **133–134**: p. 166-175.

46. Verners, O. and A.C.T. van Duin, *Comparative molecular dynamics study of fcc-Ni nanoplate stress corrosion in water.* Surface Science, 2015. **633**: p. 94-101.

47. Zou, C., et al., *Molecular dynamics simulations of the effects of vacancies on nickel self-diffusion, oxygen diffusion and oxidation initiation in nickel, using the ReaxFF reactive force field.* Acta Materialia, 2015. **83**: p. 102-112.

1.6 Figures

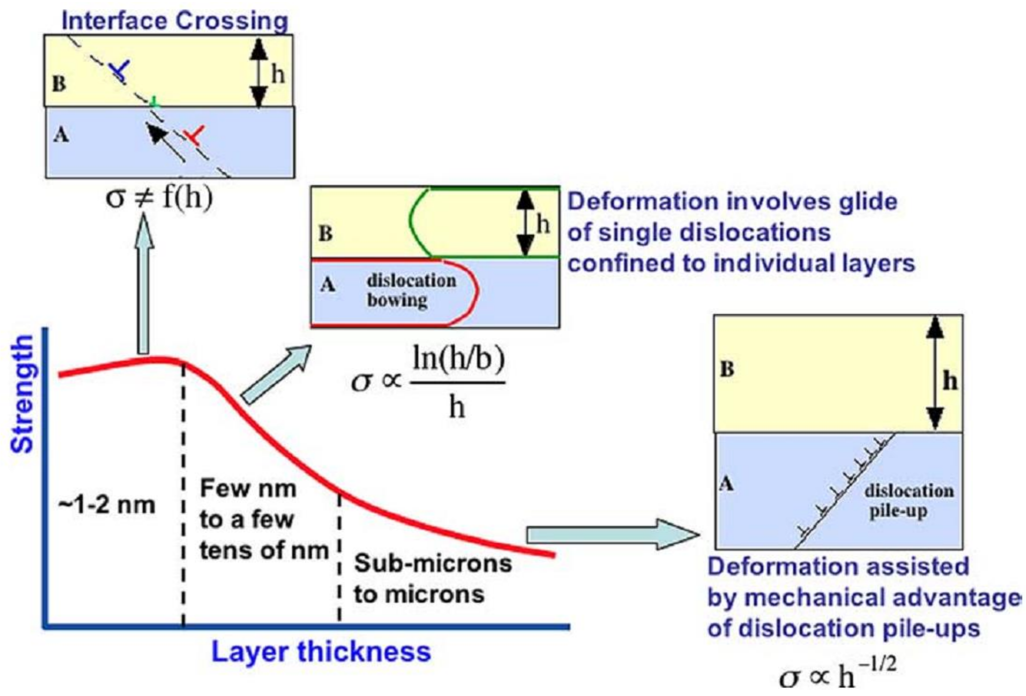

Figure 1.1 Dislocations mechanism through different length scale individual layer thicknesses [22].

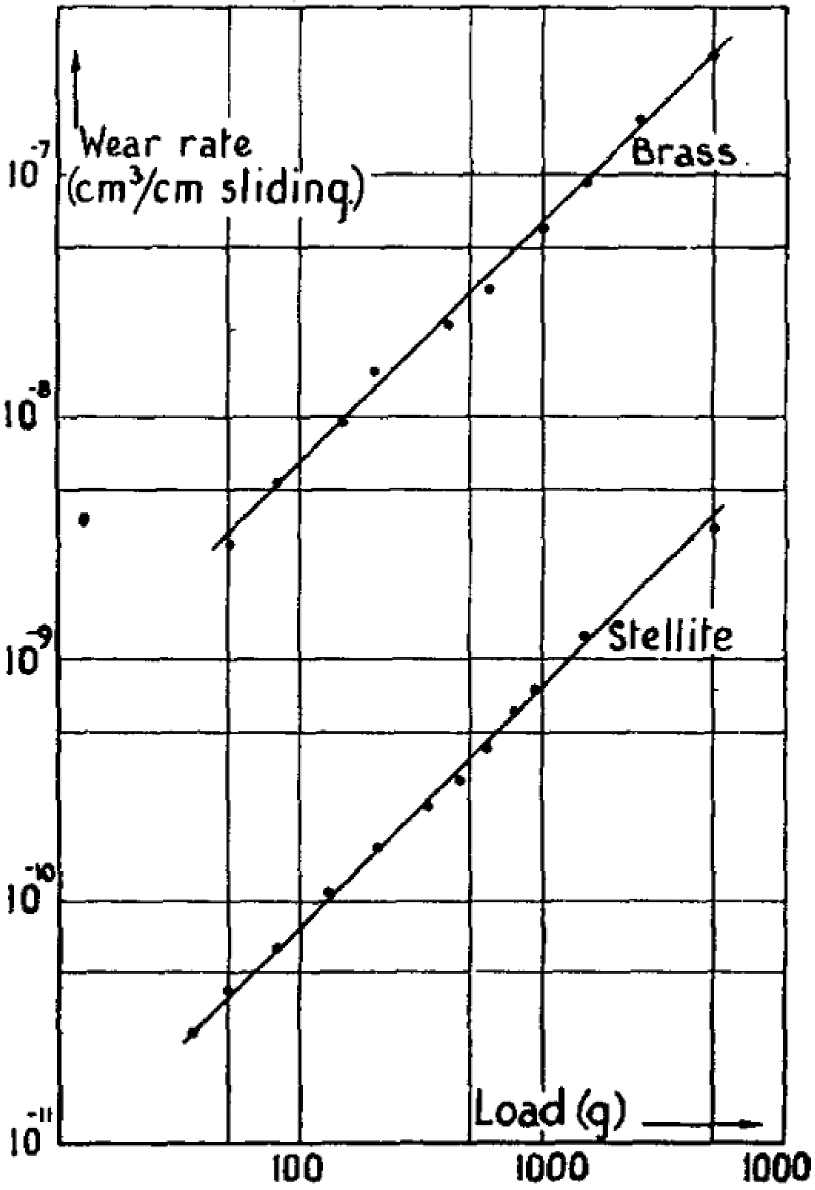

Figure 1.2 Wear rate increase with increase of normal load with a steady slope based on the Archard's theory [37].

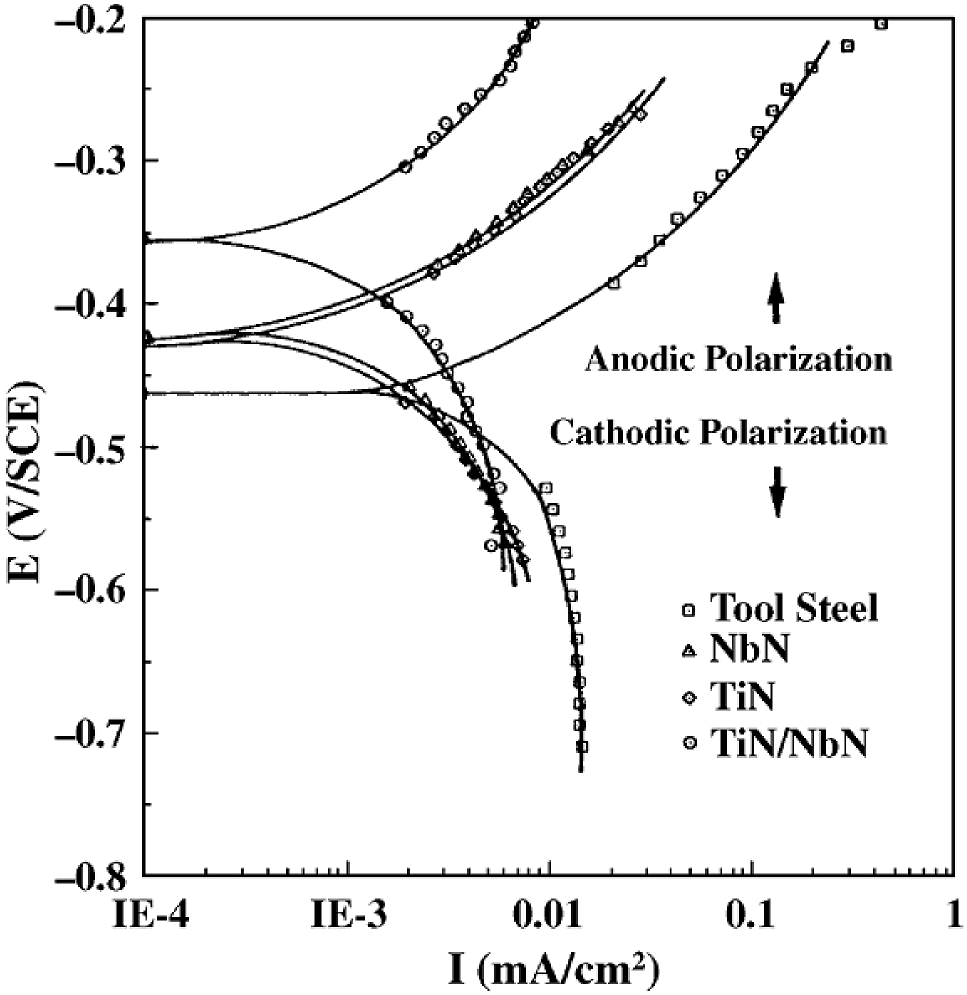

Figure 1.3 Potentiodynamic polarization curve which is generated after the test and indicates current density and open circuit voltage [3].

CHAPTER 2: MICROSTRUCTURE AND MECHANICAL PROPERTIES OF AL/TI NMMS

2.1 Introduction

Nanostructured metallic multilayers (NMMs) represent a new class of engineering materials that exhibit excellent physical, mechanical, and tribological properties due to the nano-scale layered structure. They are widely used in x-ray optics, thin film magnets, wear-resistant coatings, microelectromechanical devices, and as radiation damage tolerant materials. Extensive research has been carried out to study the relationship between the microstructure and mechanical properties of NMMs. In particular, it was discovered that near-theoretical strength can be achieved at extremely small layer thicknesses [1]. The deformation behavior and strengthening mechanism of NMMs are sensitive to layer thickness and interface structure. It is generally accepted that three different deformation modes may operate, depending on the layer thickness h [1-3]. When h is at submicron length scales, dislocations pile up against the interfaces and the Hall-Petch hardening model applies, where the strength increases with decreasing layer thickness as $\sigma \propto h^{-1/2}$. When h is from a few to a few tens of nanometers, there is insufficient spacing between the interfaces for dislocation pile-up; thus, Hall-Petch hardening breaks down. The deformation mechanism now involves the motion of single dislocation bowing between the interfaces, where the confined layer slip (CLS) mechanism operates. In this regime, the yield strength is found to increase with decreasing layer thickness as $\sigma \propto \ln(h)/h$ [1]. The stress reaches a maximum value at approximately $h \approx 5$ nm. After that, deformation mechanisms of NMMs become insensitive to layer thickness but highly sensitive to the structure and property of interfaces, as they represent a large volume fraction with decreasing layer thicknesses. For NNMs with coherent interfaces, such as Cu/Ni multilayers, strength depends on the coherency strains, and the maximum flow stress is equal to the coherency stress. For NNMs with incoherent interfaces, the deformation mode is associated with the transmission of single glide dislocation across interfaces [4].

Extensive previous research highlights the fact that novel deformation physics control plasticity in the NMMs. However, the vast majority of these studies focus on multilayers consisting of face-centered cubic (fcc) and body-centered cubic (bcc) structures, while those of fcc/hcp (hexagonal close-packed) multilayers remain limited. In this study, we chose Al/Ti as a model system to study the structure-sensitive mechanical and tribological properties of fcc/hcp NMMs. Al/Ti NMMs have been studied previously for their self-propagating reactions [5], but there has been very limited prior research on the mechanical and tribological behavior of this system [6]. Due to the low densities of the constituent materials ($\rho_{Al} = 2.7$ g/cm^3 and $\rho_{Ti} = 4.5$ g/cm^3), the Al/Ti NMMs, with nominal density of ~ 3.6 g/cm^3, are also promising novel lightweight high strength materials. In the current work, Al/Ti NMMs were synthesized with six representative layer thicknesses, 2.5 nm, 5.2 nm, 11.4 nm, 30 nm, 36 nm and 52 nm, to reveal the structural evolution when different deformation mechanism operates. The goals of the current work are to (1) synthesize and characterize Al/Ti NMMs at various layer thicknesses, (2) investigate the mechanical properties of Al/Ti NMMs, and (3) establish the relationship between the microstructure evolution and mechanical responses as a function of layer thickness.

2.2 Experimental Procedure

After defining the principal deposition parameters and physical properties of specimens, six Al/Ti NMMs were prepared using modified SFI cluster sputter tool. Earton 8210 power supply with direct current was used to deposit multilayers on Si (100) substrate. S-Gun toroidal Al target with 99.999% purity and 9” diameter along with the S-gun toroidal Ti target with 99.999% purity and 3” diameter were used in two sequential chambers. Argon gas flow maintained the chamber pressure at ~ 5 mTorr. The observed pressure for Ti and Al deposition was ~ 5.9 mTorr and 4.2 mTorr respectively. Post-deposition NMMs were covered using a thin positive photoresist to act as a protective layer during dicing and through storage. Specimen wafers were then diced in half. The first half of specimens were then used for nondestructive grazing incident X-ray diffraction (GIXRD) tests and the second half was diced into multiple 1 cm × 1 cm pieces for destructive tests including wear, indentation and corrosion. Figure 2.1 indicates a schematic of NMM, photos of the sputtering tool and deposited NMMs. Primary GIXRD was performed on all six samples using PANAlytical X’Pert PRO diffractometer (Cu Kα, 154.06 pm) from Philips with a voltage of 45 kV and 40 mA current. The main reason for not using typical XRD method (Bragg-Brentano configuration) was to keep the substrate peak intensity proportionally low compared to constituent phases. Also considering that some of the samples have less than 1 µm in overall thickness, GI-XRD turned out to be a better choice over B-B configuration. Incident beam optic was chosen to be Cu mirror, and the diffracted beam receiver was parallel plate collimator (PPL). Divergence slit was $\frac{1}{8}$ ° fixed slit and depending on the size of the sample, a mask of 10 mm to 20 mm was used. Step size was set to be at most 0.01° and time per step was 10 seconds. The grazing incident was chosen to be 3° for all samples and scan span was from 2θ=32° to 2θ=85°.

For the purpose of measuring residual stress in NMMs several sets of GIXRD were performed on all six samples with a step size in the range of 0.01 ° to 0.001 °. Time per step of scans was in the range of 15 to 70 seconds depending on total thickness and ψ or φ tilt angles. Scans were performed in at least 7 different ψ angles from a combination of: 0°, ±10, ± 15°, ± 30°

and ± 35°. Several different methods were examined including conventional $\mathrm{Sin}^2\psi$ method (in both psi and chi angles), Perry method [7] based on Seemann-Bohlin X-ray diffraction and Marion-Cohen method [8] were evaluated. Finally $\mathrm{Sin}^2\psi$ method was chosen for measuring the stresses in non-textured specimens and Marion-Cohen method was used when the specimen was highly textured. Because almost half of the samples demonstrated textured behavior it was necessary to scan the whole peak span for post processing of integrated intensities. XRD patterns were then analyzed using OriginPro, Highscore Plus and X′Pert view software. Scanning electron microscopy (SEM) was performed using Hitachi SU-70 with a maximum acceleration voltage of 30 kV for a pre-evaluation of surface smoothness and recording grain size of top aluminum layers before AFM test. Arithmetic surface roughness (*Ra*) was measured and mapped using DI AFM tool and *Nanoscope* software. For each sample, at least, three different surface scans with a different scan size of 2 µm, 5 µm and 10 µm were performed. The scan rate was kept as low as 0.5 Hz and sample line was set to be at maximum possible 512 lines to produce a smooth image. Data was gathered in two different formats of Height and Phase. It is common to keep arithmetic surface roughness (Ra) less than 5% of maximum penetration depth in indentations to produce valid nanoindentation results. These values of surface roughness along with the 1/10s method [9] were then implemented during nanoindentation tests.

Nanoindentation was performed using Hysitron Ti900 Triboindenter equipped with a standard Berkovich tip with a curvature radius of ~150 nm to determine the reduced elastic module (E_r) and hardness (H). Before nanoindentation, the machine was calibrated using standard fused quartz for machine compliance and tip area function. After calibration, a hardness of ~ 9.5 ± 0.15 GPa (expected to be 9.5 GPa with 10 % allowable deviation) and reduced young's module of ~ 69.57 ± 0.54 GPa (supposed to be 69.6 GPa with 5 % allowable deviation) was found for the fuse quartz. A standard trapezoidal loading pattern was used for all the specimens with loading, hold and unloading times of 3, 2 and 3 seconds respectively. 20 indents were performed in a range of 500 µN – 10 mN. The target loads were then chosen based on piezo displacement under a specific load for each NMM. The final ranges of loads from 1 mN to 3 mN were varied based on sample thickness and penetration depth of indenter tip into sample. After selecting optimal loads, at least, 20 indents were performed on each NMM with a pre-selected optimal load while there was, at least, 15 μm spacing between indents to prevent any interactions. Finally, 15+ of initial indents were chosen based on the loading vs. time profiles to be considered for the purpose of measuring hardness and young's module of the specimen. Nanoindentation raw data analysis was obtained using Triboscan software which analyzes nanoindentation data based on Oliver and Pharr method [10]. Several calibration including tip area function, air calibration and machine compliance before and after the experiments were performed on standard fused quartz to make sure that the obtained results are as much as possible accurate. Final maximum penetration depth for each sample was kept less than 15% of the total film thickness.

Cross-sectional transmission electron microscopy (TEM) samples were prepared following the standard lift-out procedure in a FEI Quanta dual beam microscope. Wide range of currents from 30 pA to 3 µA for ion beam were used depending on the purpose of milling and amount of protection layers over the coatings. If the purpose of milling was only measuring the overall thickness then only platinum (Pt) was used on top of NMM layers. For the purpose of TEM cross section lift-out before ion beam deposition, there was, at least, one more protection layer deposited using an electron beam or an overall thin layer of carbon deposition over a large surface around the target location. Initial deposition using E-beam produced a thickness up to ~100 nm. E-beam Pt deposition was performed by using selective area scan with a low beam current (as low as 50 pA) and high-speed scan rate (up to 100 ns). Standard lift-out procedure was then continued by depositing ~1.5 µm - 3 µm of Pt using ion beam over the targeted region. After depositing protective layers, milling of top and bottom sections of target region was started using ion beam currents of 5 µA, 3 µA and 1 µA respectively until the target cross section thickness reaches ~500 nm. Undercutting was then performed by tilting the sample and milling bottom and right side of it using relatively low ion beam currents to prevent damage to the unprotected cross section. Fig. 2.2 demonstrates different steps of sample preparation using focused ion beam (FIB) for the purpose of TEM imaging and analysis.

2.3 Results and Discussion

2.3.1 XRD Results

GIXRD patterns are shown in Fig. 2.3 for sample A through sample F with the peak annotations. Highest peak intensities belong to Si (311) which comes from the silicon substrates. Although a relatively low angle of the grazing incident was chosen (3°) substrates peaks presence were inevitable in XRD patterns. Decreasing the grazing incident to overcome the mentioned issue would also reduce other peaks intensity. By decreasing the individual layer thickness through different NMMs, two different changes were noticed in GIXRD patterns: (1) peak intensity is declining while the time per step is the same for all samples; (2) peak broadening is visible while the individual layer thickness is decreasing. The decrease of intensity with individual layer thickness was reported previously [11, 12] in different metallic multilayers with small individual (and overall) thicknesses and peak broadening is a sign of smaller crystal size in samples with smaller individual layer thickness [13]. GIXRD results indicate the formation of aluminum and titanium phases in all NMMs as represented by the superposition of Al (111)/Ti (00.2) at $2\theta \sim 38.5°$, Al (220) at $2\theta \sim 65.1°$ and Ti (311) at $2\theta \sim 70.1°$.

2.3.2 Surface Morphology Characterization Using SEM and AFM

SEM images of as-deposited samples are shown in Fig. 2.4. SEM images indicate nodules with a size in the range of 150 nm - 450 nm in diameter. Because of low resolution in high magnifications it’s hard to report exact size of grain on the surface of specimens based on SEM images. For more accurate analysis atomic force microscopy (AFM) was implemented to scan all NMMs and monolithic sample surfaces. AFM scan indicated an increasing trend for surface roughness and grain size from sample A to F. Figure 2.5 shows the difference in surface roughness of specimens by comparing AFM scans while keeping the scan scale of 5 μm for all samples. Fig. 2.6 compares the arithmetic surface roughness (Ra) and grain size of all NMM and monolithic samples, each data point was extracted from an average of 100 measurements using Image J software over AFM phase images. While all the samples were deposited with the similar physical condition and rate of deposition, monolithic aluminum shows significantly higher grain size (more than three times) compared to monolithic titanium. Similar behavior was also observed for the surface roughness c. On the other hand multilayer structures in NMMs seem to be decreasing both the grain size and surface roughness when the individual layer thickness is less than 30 nm. Similar behavior has been observed before in Al/Cr NMM coatings [14]. Based on previous works [15-17], it was concluded that the presence of titanium in Al/Ti NMMs will limit the size of aluminum columnar by interrupting their growth through multilayer structure [18].

2.3.3 TEM Analysis

TEM images from NMMs cross-sections reveal the total and individual layer thickness along with the columnar grain size of specimens. On thicker NMMs a well-established layer by layer structure with clear interfaces is visible but decreasing the bilayer thickness will cause wavy behavior in interfaces and especially in columnar grain boundaries. Sample A and sample D with individual layer thickness of 2.5 nm and 30 nm respectively were chosen for more detailed analysis. Fig. 2.7 indicates the TEM image from the cross section of samples A and D, where the titanium and aluminum layers corresponds to the dark and bright layers respectively. Furthermore analysis using Gatan Digital micrographs over the cross-section images indicate the in-plane grain size are in good agreement with the AFM results reported in the previous section.

2.3.4 Nanoindentation Results

Based on the overall thickness of specimen an acceptable range of penetration [9] was defined for each NMM to prevent any substrate effects during nanoindentation. Table 2.1 indicates the physical and mechanical properties of as-deposited specimens based on TEM, SEM and nanoindentation results. Nano indentation hardness (H) versus the inverse of individual layer thickness ($h^{-1/2}$) of Al/Ti NMMs are plotted in Fig. 2.8 along with several other NMM structures [19-22]. Almost all of other NMMs presented in Fig. 2.8 contain aluminum or titanium as a phase in their multilayer structure. Except for Al/TiN which has a ceramic structure experimental results from the current study over Al/Ti NMMs demonstrate a much better mechanical hardness. The linear section of data pints (indicated with red trend line) represents the NMMs with thicker bilayers. This section of data points follow the Hall-Petch model with k ~ 15.23 GPa $(nm)^{1/2}$ and H_0 ~ 0.32 GPa. As predicated before [1], it however overestimates other NMMs hardness with smaller bilayers. As suggested by prior studies [12, 19, 23, 24], deformation mechanism of NMMS with individual layer thickness in the range of 35 nm –50nm for switches from Hall-Petch to CLS. Decreasing the individual layer thickness in NMMs structure to less than 50 nm will increase the structure strength. At these range of layer thicknesses, the strength of NMM can be estimated from the CLS model as:

$$\sigma_{cls} = M\frac{\mu b}{8\pi h'}\left(\frac{4-\nu}{1-\nu}\right)\left[\ln\frac{\alpha h'}{b}\right]-\frac{f}{h}+\frac{C}{\lambda}\text{, and } C=\frac{\mu b}{(1-\nu)} \qquad (1)$$

where M is the Taylor factor, υ is the Poisson's ratio, μ is the shear modulus, b is the Burgers vector , and h′ = h/sin (φ) where φ is the angle between the interface and slip plane. f, α and λ are interface stress, core cut-off parameter and interfaces spacing respectively and can be found through curve fitting the experimental data. In the current work, the following values were used: M = 3.1, υ = 0.32, μ = 44 GPa and b = 0.17 nm. Material strength was then estimated by using equantion (1) and fitting the experimental data. Fitting results show a very consistent match between experimental results from nanoindentation and theoretical calculations based on CLS model, with fitting parameters in the pre-defined ranges [22]. NMMs hardness was then achieved by multiplying Tabor factor and flow stress (σ). Figure 2.9 demonstrates the experimental nanoindentation hardness along with the theoretical predictions based on CLS model for Al/Ti NMMs. Experimental results indicate that the maximum strength was achieved in specimen A with a hardness of ~ 4.94 GPa, which is comparable to the hardness of monolithic titanium although half of the NMM is made from soft aluminum phase. Thus the nanoindentation results indicate the formation of lightweight Al/Ti NMMs with exceptional mechanical properties achieved by tailoring the individual layer thickness.

2.3.5 Residual Stress Measurement

The residual stress in NMM originates from the difference in thermal expansion coefficients between the film and substrate or from the lattice misfit between alternating layers [25]. Residual stress was measured in two constituent phases of aluminum and titanium separately using GI-XRD scans. As indicated by prior studies [26-28] aluminum and titanium layers have a preferred growth direction in <111> and <00.2> respectively. TEM analysis along with XRD results confirm the growth direction from previous studies. Fig. 2.3 indicates the XRD results from all six NMMs. Peaks scattered from Ti (00.2) and Al (111) planes have a superposition at ~ 38.5°, which makes it impossible to distinguish them. So determining the residual stress based on the shift of peak at 38.5° is not possible. Thus in the current study, residual stresses were calculated from the the Al (220) and Ti (01.3) peaks.

Stress measurement procedure for Ti phase was based on Ti (01.3) peaks shift and calculations indicate a uniform positive (tensile) stress for titanium phase in all six NMMs. Monolithic Ti specimen was also tested and demonstrated the same type of (tensile) stress. Tensile stress for Ti phase is in agreement with prior study [29] on sputtered titanium deposited at the same pressure (~ 5.9 mTorr) and deposition rate. In fact achieved residual stress (~ 180 MPa) for monolithic titanium film with ~ 1.2 µm thickness is comparable to the literature report (~ 210 MPa) for a ~ 1 µm film of sputtered titanium. The decrease of residual stress with an increase of thickness is as expected due to increased relaxation of the thin film. It is expected that residual stress ultimately becomes independent of layer thickness at larger layer thickness [30].

Sputtered aluminum is expected to have an increasing compressive stress while its layer thickness is increasing from a few nanometer to tens of nanometer [31]. Such behavior however was not observed here. Instead, by decreasing the bilayer size, the compressive stress in Al increases. The higher amount of compressive stress of Al phase in smaller bilayer thicknesses is due to the compression by denser Ti particles during deposition. This behavior is similar to what happens during shot peening and has been reported for the aluminum phase in Al/SiC multilayers [32]. It is common in low-pressure deposition of multilayers with only a few nanometer bilayer thickness.

The overall residual stress of NMM films with two phases of X and Y can be determined through the following equation:

$$\sigma_{NMM} = \sigma_{phase\ X} + \sigma_{phase\ Y} + \sigma_{Coh\ X} - \sigma_{Coh\ Y} \quad (2)$$

where $\sigma_{phase\ X}$ and $\sigma_{phase\ Y}$ represent the residual stress in X and Y phase respectively measured from XRD scans, and $\sigma_{Coh\ X}$ and $\sigma_{Coh\ Y}$ are the coherency stress of the noted phases. The coherency stress in multilayers with equal layer thicknesses have the same magnitude [33] so they will cancel out each other and as a result, the final film stress will be an average of residual stresses of the two phases. The overall film residual stresses are indicated by green columns in Fig. 2.10, which reaches a maximum value of ~ 1.34 GPa at an individual layer thickness of 5.2 nm.

Multilayer structure will change the expected mechanical properties, typically attributed to residual stress in both Al and Ti phases. As an example, more positive (or tensile) residual stress in monolithic Ti reduces the overall strength of coating [34] and in monolithic aluminum a more compressive stress will increase the strength of specimen [35]. As it was indicated, this is not the case for Al/Ti multilayers. Based on nanoindentation and XRD tests in examined NMMs, overall strength is constantly increasing while the tensile stress in the coating is increasing. The increase of tensile stress with a decrease of bilayer size has also been reported before [33, 36]. For gold layers in Au/Ni NMMs, when the individual layer thickness is ~ 9 $\dot{A}$, residual stress approaches to ~ 3.9 GPa, which is significantly higher than the yield stress of bulk Au [37]. Same high stress has also been observed for tungsten in W/Cu multilayer with a maximum stress of 6.4 GPa at 4.2 nm thick layers of W [38]. In smaller bilayers effect of interfaces becomes more important. It is important to know how the interface acts to decrease or increase the overall residual stress. It was indicated by Hull that mismatch strains are significantly dependent on the misfit dislocation at interfaces [39]. So decreasing the bilayer will significantly amplify the effect of interfaces. In a study of sliver and nickel multilayer [33] increase of interfaces density was, in fact, the source of more positive (tensile) stress. More interfaces induce higher interface stress which was measured to be ~ -2.27 ±0.67 (J/m^2). There is no direct method for measuring the interface stress in NMMs but it can be calculated through the following equation:

$$\sigma_{SC} - < \sigma > = \frac{2f}{\lambda} \quad (3)$$

where σ_{SC} is the stress measured from the substrate curvature using Stoney method [40], σ is the stress of coating measured using XRD scans; f is the interface stress, and λ is the bilayer thickness. Unfortunately, no data from the substrate curvature was gathered before deposition, so evaluation of substrate curvature and consequently interface stress is not possible here.

Figure 2.10 indicates the residual stress of both Al and Ti phases for all Al/Ti NMMs. An important factor here is that how does the type (tensile or compressive) and magnitude of stress affect the crystal structure of the film. On a study of Au/Ni metallic multilayers [41] a negative and positive strains in Au and Ni were reported respectively. While the bilayer thickness was decreasing, because of the residual stress the coherency of the system was increasing which resulted in reducing the difference in the lattice parameter of two phases.

Figure 2.16 indicated the d-spacing variation for both aluminum and titanium phases in Al/Ti NMMs measured at $\psi = 0$. By reducing the bilayer thickness Al d-spacing decreases from ~0.1432 nm to ~ 0.1428 nm. Ti d-spacing is also increased with a decrease of bilayer thickness from ~ 0.13335 nm to ~ 0.134 nm. To evaluate the coherency of interfaces two adjacent planes d-spacing (or lattice constant) need to be compared but as it was indicated at the beginning comparing the Ti (00.2) and Al (111) is not possible because of the superposition. Since the measured residual stress in this study is an average of stress in a volume of materials [42] the same type of size change in the d-spacing of adjacent interfaces can be expected.

Another important issue here is that both aluminum and titanium might go through a partial [27, 28] phase transformation while the bilayer thickness is changing. Rajarshi et al. [43] indicates that for AL/Ti NMM at a bilayer thickness of 5.2 nm, both Al and Ti phases exhibit HCP structure while their d spacing is almost identical at ~ 0.2314 nm. Mentioned bilayer thickness for Al/Ti is very much close to NMM A with a bilayer of ~ 5 nm. Indeed, Sample A demonstrated the maximum nano hardness in nanoindentation tests and as it was pointed out at the beginning, a more coherent interface will eventually increase the multilayer structure strength [44].

2.4 Summary and Conclusions

Six Al/Ti NMMs along with their monolithic constituents were deposited separately on silicon substrates. SEM and AFM analysis of sample surfaces indicate that the grain size and surface roughness generally decreases with decreasing individual layer thickness. Nanoindentation test indicates exceptional strength of NMM at 2.5 nm layer thickness, comparable to bulk titanium. The increase of strength of NMMs with decreasing layer thickness were in good agreement with s modified CLS model. Residual stress measurement performed using GIXRD indicated negligible stress for samples with thicker bilayers. This trend changes with decreasing individual layer thickness. Significant tensile residual was present in the Ti phase at small layer thickness (2.5 and 5 nm) while aluminum phases exhibited compressive stress. The nature and magnitude of residual stresses in Al and Ti layers were believed to be governed by the deposition conditions such as deposition pressure. These stresses may decrease the misfit strain and ultimately result in a more coherent interface which leads to higher strength of NMMs.

2.5 References

1. Misra, A., J.P. Hirth, and R.G. Hoagland, *Length-scale-dependent deformation mechanisms in incoherent metallic multilayered composites.* Acta Materialia, 2005. **53**(18): p. 4817-4824.

2. Misra, A., et al., *Deformation mechanism maps for polycrystalline metallic multiplayers.* Scripta Materialia, 1999. **41**(9): p. 973-979.

3. Misra, A. and H. Kung, *Deformation behavior of nanostructured metallic multilayers.* Advanced Engineering Materials, 2001. **3**(4): p. 217-222.

4. Wang, J. and A. Misra, *An overview of interface-dominated deformation mechanisms in metallic multilayers.* Current Opinion in Solid State & Materials Science, 2011. **15**(1): p. 20-28.

5. Gachon, J.C., et al., *On the mechanism of heterogeneous reaction and phase formation in Ti/Al multilayer nanofilms.* Acta Materialia, 2005. **53**(4): p. 1225-1231.

6. Levashov, E.A., et al., *Multilayer Nanostructured Heat-Generating Coatings. Preparation and Certification of Mechanical and Tribological Properties.* Metallurgist, 2011. **54**(9-10): p. 623-634.

7. Valvoda, V., et al., *Structural analysis of tin films by Seemann-Bohlin X-ray diffraction.* Thin Solid Films, 1990. **193**: p. 401-408.

8. Paulik, S.W., et al., *Residual stress in ceramics with large thermal expansion anisotropy.* Journal of Materials Research, 1996. **11**(11): p. 2795-2803.

9. Saha, R. and W.D. Nix, *Effects of the substrate on the determination of thin film mechanical properties by nanoindentation.* Acta Materialia, 2002. **50**(1): p. 23-38.

10. Oliver, W.C. and G.M. Pharr, *An improved technique for determining hardness and elastic modulus using load and displacement sensing indentation experiments.* Journal of Materials Research, 1992. **7**(06): p. 1564-1583.

11. Chen, Y., et al., *Microstructure and strengthening mechanisms in Cu/Fe multilayers.* Acta Materialia, 2012. **60**(18): p. 6312-6321.

12. Yu, K.Y., et al., *Strengthening mechanisms of Ag/Ni immiscible multilayers with fcc/fcc interface.* Surface and Coatings Technology, 2013. **237**: p. 269-275.

13. Langford, J.I. and A.J.C. Wilson, *Scherrer after sixty years: A survey and some new results in the determination of crystallite size.* Journal of Applied Crystallography, 1978. **11**(2): p. 102-113.

14. Creus, J., et al., *Mechanical and corrosion properties of dc magnetron sputtered Al/Cr multilayers.* Surface and Coatings Technology, 2008. **202**(16): p. 4047-4055.

15. Barshilia, H.C., et al., *Corrosion behavior of nanolayered TiN/NbN multilayer coatings prepared by reactive direct current magnetron sputtering process.* Thin Solid Films, 2004. **460**(1–2): p. 133-142.

16. Li, J., et al., *AlN/Al dual protective coatings on NdFeB by DC magnetron sputtering.* Journal of Magnetism and Magnetic Materials, 2009. **321**(22): p. 3799-3803.

17. Liu, C., et al., *Effects of Ti/TiN multilayer on corrosion resistance of nickel–titanium orthodontic brackets in artificial saliva.* Corrosion Science, 2007. **49**(10): p. 3783-3796.

18. Xie, T., et al., *Structure, corrosion, and hardness properties of Ti/Al multilayers coated on NdFeB by magnetron sputtering.* Vacuum, 2012. **86**(10): p. 1583-1588.

19. Fu, E.G., et al., *Mechanical properties of sputtered Cu/V and Al/Nb multilayer films.* Materials Science and Engineering: A, 2008. **493**(1–2): p. 283-287.

20. Ham, B. and X. Zhang, *High strength Mg/Nb nanolayer composites.* Materials Science and Engineering: A, 2011. **528**(4–5): p. 2028-2033.

21. Bhattacharyya, D., et al., *A transmission electron microscopy study of the deformation behavior underneath nanoindents in nanoscale Al–TiN multilayered composites.* Philosophical Magazine, 2010. **90**(13): p. 1711-1724.

22. Lu, Y.Y., et al., *The microstructure and mechanical behavior of Mg/Ti multilayers as a function of individual layer thickness.* Acta Materialia, 2014. **63**: p. 216-231.

23. Wen, S.P., et al., *Nanoindentation investigation of the mechanical behaviors of nanoscale Ag/Cu multilayers.* Journal of Materials Research, 2007. **22**(12): p. 3423-3431.

24. Zhang, J.Y., et al., *Tailoring nanostructured Cu/Cr multilayer films with enhanced hardness and tunable modulus.* Materials Science and Engineering: A, 2012. **543**: p. 139-144.

25. Hsueh, C.-H., *Modeling of elastic deformation of multilayers due to residual stresses and external bending.* Journal of Applied Physics, 2002. **91**(12): p. 9652-9656.

26. Izadi, S., H. Mraied, and W. Cai, *Tribological and mechanical behavior of nanostructured Al/Ti multilayers.* Surface and Coatings Technology, (0).

27. Shechtman, D., D. van Heerden, and D. Josell, *fcc titanium in Ti-Al multilayers.* Materials Letters, 1994. **20**(5): p. 329-334.

28. Banerjee, R., et al., *Phase stability in Al/Ti multilayers.* Acta Materialia, 1999. **47**(4): p. 1153-1161.

29. Ljungcrantz, H., et al., *Residual stresses and fracture properties of magnetron sputtered Ti films on Si microelements.* Journal of Vacuum Science & Technology A, 1993. **11**(3): p. 543-553.

30. Moridi, A., et al., *Residual stresses in thin film systems: Effects of lattice mismatch, thermal mismatch and interface dislocations.* International Journal of Solids and Structures, 2013. **50**(22–23): p. 3562-3569.

31. Pletea, M., et al., *In situ stress evolution during and after sputter deposition of Al thin films.* Journal of Physics: Condensed Matter, 2009. **21**(22): p. 225008.

32. Singh, D.R.P., et al., *Residual stress characterization of Al/SiC nanoscale multilayers using X-ray synchrotron radiation.* Thin Solid Films, 2010. **519**(2): p. 759-765.

33. Ruud, J.A., A. Witvrouw, and F. Spaepen, *Bulk and interface stresses in silver-nickel multilayered thin films.* Journal of Applied Physics, 1993. **74**(4): p. 2517-2523.

34. Chang, R.C., et al., *Residual stresses of sputtering titanium thin films at various substrate temperatures.* J Nanosci Nanotechnol, 2010. **10**(7): p. 4562-7.

35. Huber, N. and J. Heerens, *On the effect of a general residual stress state on indentation and hardness testing.* Acta Materialia, 2008. **56**(20): p. 6205-6213.

36. Girault, B., et al., *X-ray diffraction analysis of the structure and residual stresses of W/Cu multilayers.* Surface and Coatings Technology, 2006. **201**(7): p. 4372-4376.

37. Thomas, O., et al., *Residual Stresses in Metallic Multilayers*. Vol. 06. 1996. C7-125-C7-134.

38. Goudeau, P., et al., *Determination of the residual stress tensor in Cu/W multilayers by x-ray diffraction.* Applied Physics Letters, 1993. **62**(3): p. 246-248.

39. Hull, R. and J.C. Bean, *Misfit dislocations in lattice-mismatched epitaxial films.* Critical Reviews in Solid State and Materials Sciences, 1992. **17**(6): p. 507-546.

40. Stoney, G.G., *The Tension of Metallic Films Deposited by Electrolysis.* Proceedings of the Royal Society of London A: Mathematical, Physical and Engineering Sciences, 1909. **82**(553): p. 172-175.

41. Labat, S., et al., *Interdependence of elastic strain and segregation in metallic multilayers: An x-ray diffraction study of (111) Au/Ni multilayers.* Journal of Applied Physics, 2000. **87**(3): p. 1172-1181.

42. Revie, R.W., *Oil and gas pipelines : integrity and safety handbook*. 2015: Hoboken, New Jersey : John Wiley & Sons Inc., [2015].

43. Banerjee, R., R. Ahuja, and H.L. Fraser, *Dimensionally Induced Structural transformations in Titanium-Aluminum Multilayers.* Physical Review Letters, 1996. **76**(20): p. 3778-3781.

44. Hoagland, R.G., R.J. Kurtz, and C.H. Henager Jr, *Slip resistance of interfaces and the strength of metallic multilayer composites.* Scripta Materialia, 2004. **50**(6): p. 775-779.

2.6 Tables and Figures

Table 2.1 Physical and mechanical properties of all samples.

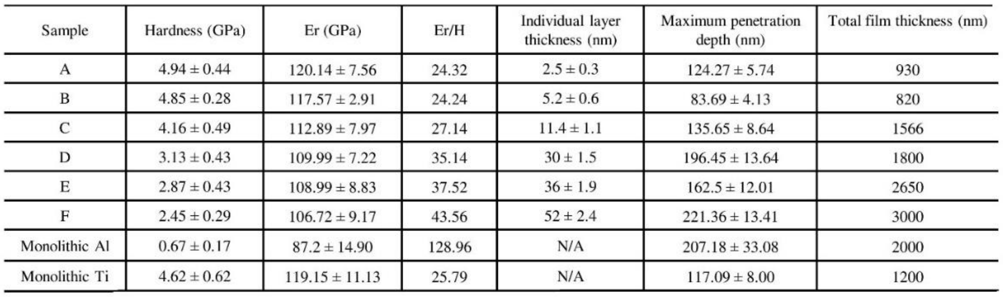

Sample	Hardness (GPa)	Er (GPa)	Er/H	Individual layer thickness (nm)	Maximum penetration depth (nm)	Total film thickness (nm)
A	4.94 ± 0.44	120.14 ± 7.56	24.32	2.5 ± 0.3	124.27 ± 5.74	930
B	4.85 ± 0.28	117.57 ± 2.91	24.24	5.2 ± 0.6	83.69 ± 4.13	820
C	4.16 ± 0.49	112.89 ± 7.97	27.14	11.4 ± 1.1	135.65 ± 8.64	1566
D	3.13 ± 0.43	109.99 ± 7.22	35.14	30 ± 1.5	196.45 ± 13.64	1800
E	2.87 ± 0.43	108.99 ± 8.83	37.52	36 ± 1.9	162.5 ± 12.01	2650
F	2.45 ± 0.29	106.72 ± 9.17	43.56	52 ± 2.4	221.36 ± 13.41	3000
Monolithic Al	0.67 ± 0.17	87.2 ± 14.90	128.96	N/A	207.18 ± 33.08	2000
Monolithic Ti	4.62 ± 0.62	119.15 ± 11.13	25.79	N/A	117.09 ± 8.00	1200

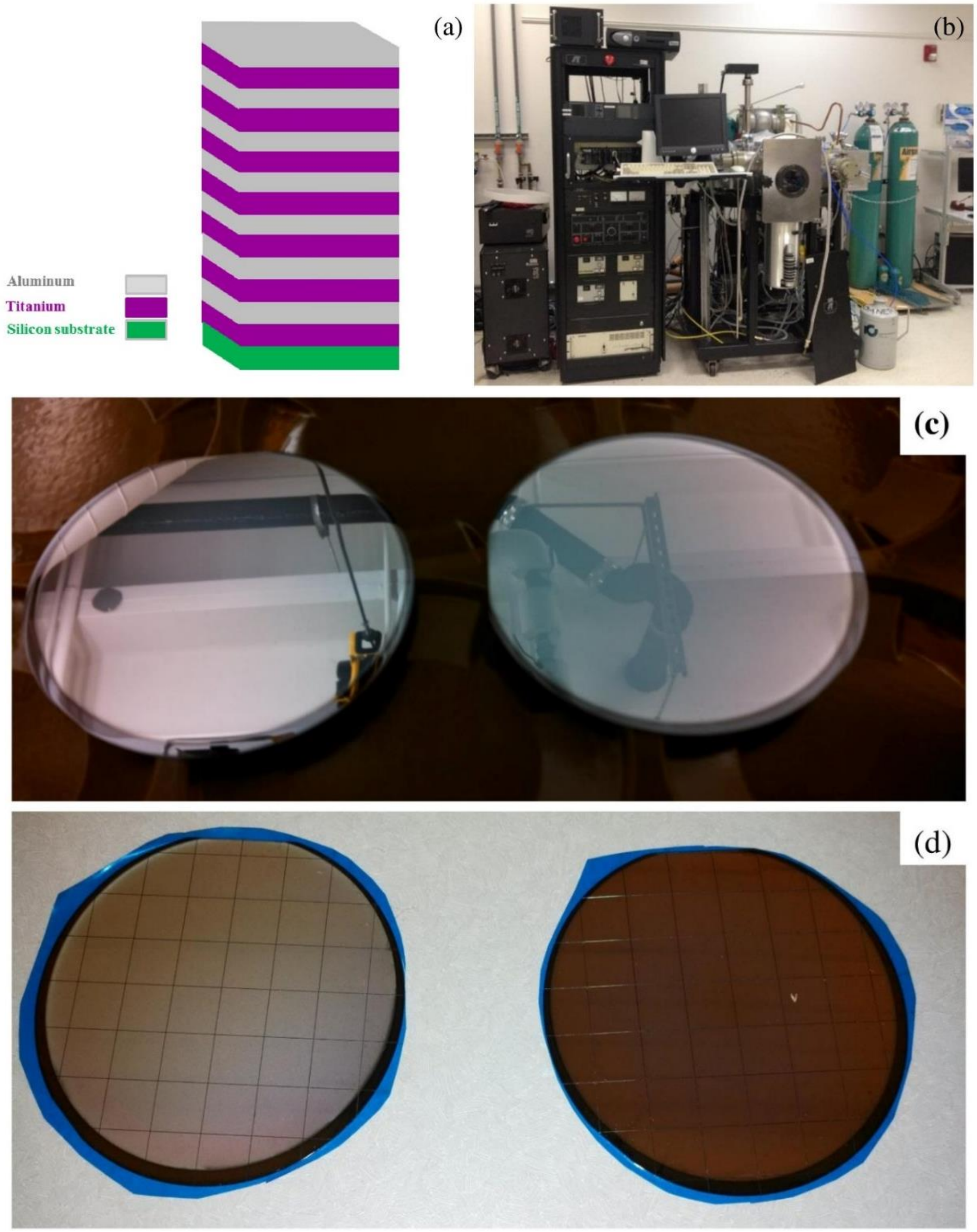

Figure 2.1 NMMS schematic, deposition tool and dicing. (a) A schematic layer by layer structure of equal-layered NMM. The bottom layer was always titanium for better adhesion with the silicon substrate. (b) Photo of modified SFI sputtering tool at nano research and educational center (NREC) at USF. Photos of (c) as-deposited Al/Ti NMMs, and (d) diced Al/Ti NMMs with photoresist protective layer on top.

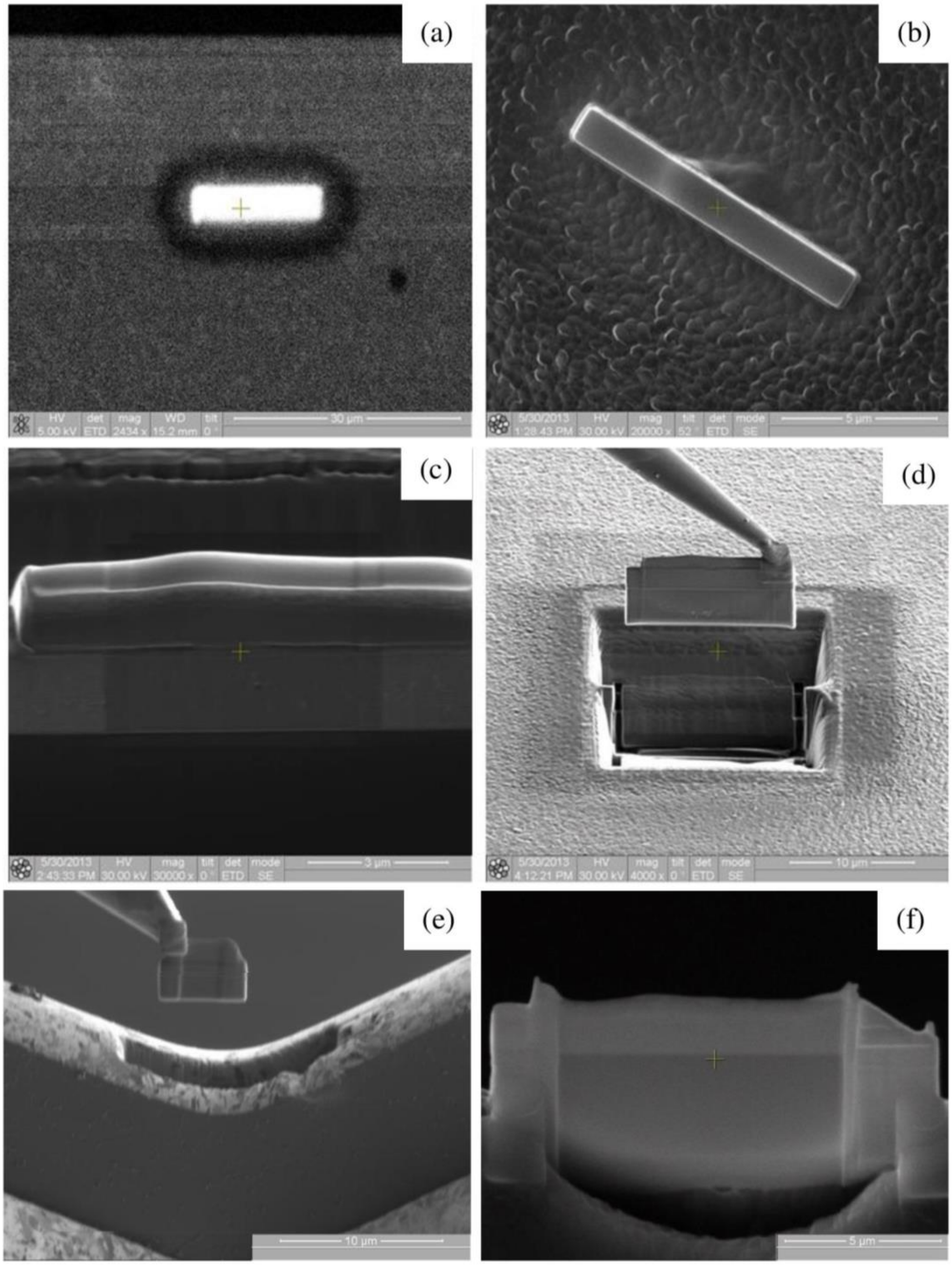

Figure 2.2 SEM images of FIB lift out procedure. (a) Deposition of platinum on sample surface using E-Beam, (b) deposition of platinum on larger cross section and over pervious protective layer using ion beam, (c) removing the side of deposited region using ion beam in several steps, (d) milling the sample cross section to OmniProbe needle and removing cross section for milling and mounting over copper grid, (e) transferring the sample over copper grid, and (f) milling the sample over copper grid followed by final thinning.

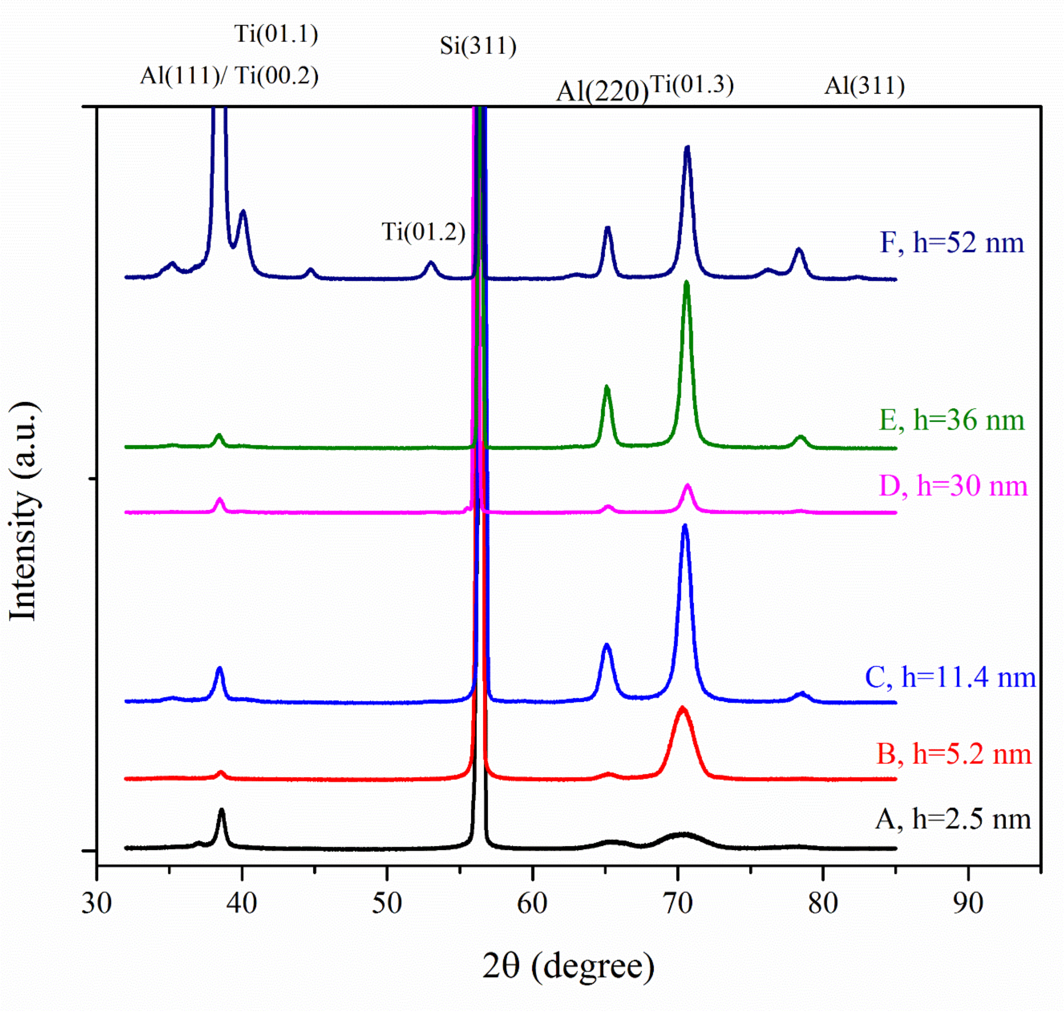

Figure 2.3 GIXRD patterns for sample A through F. Intensity of peaks is increasing proportional to individual layer thickness.

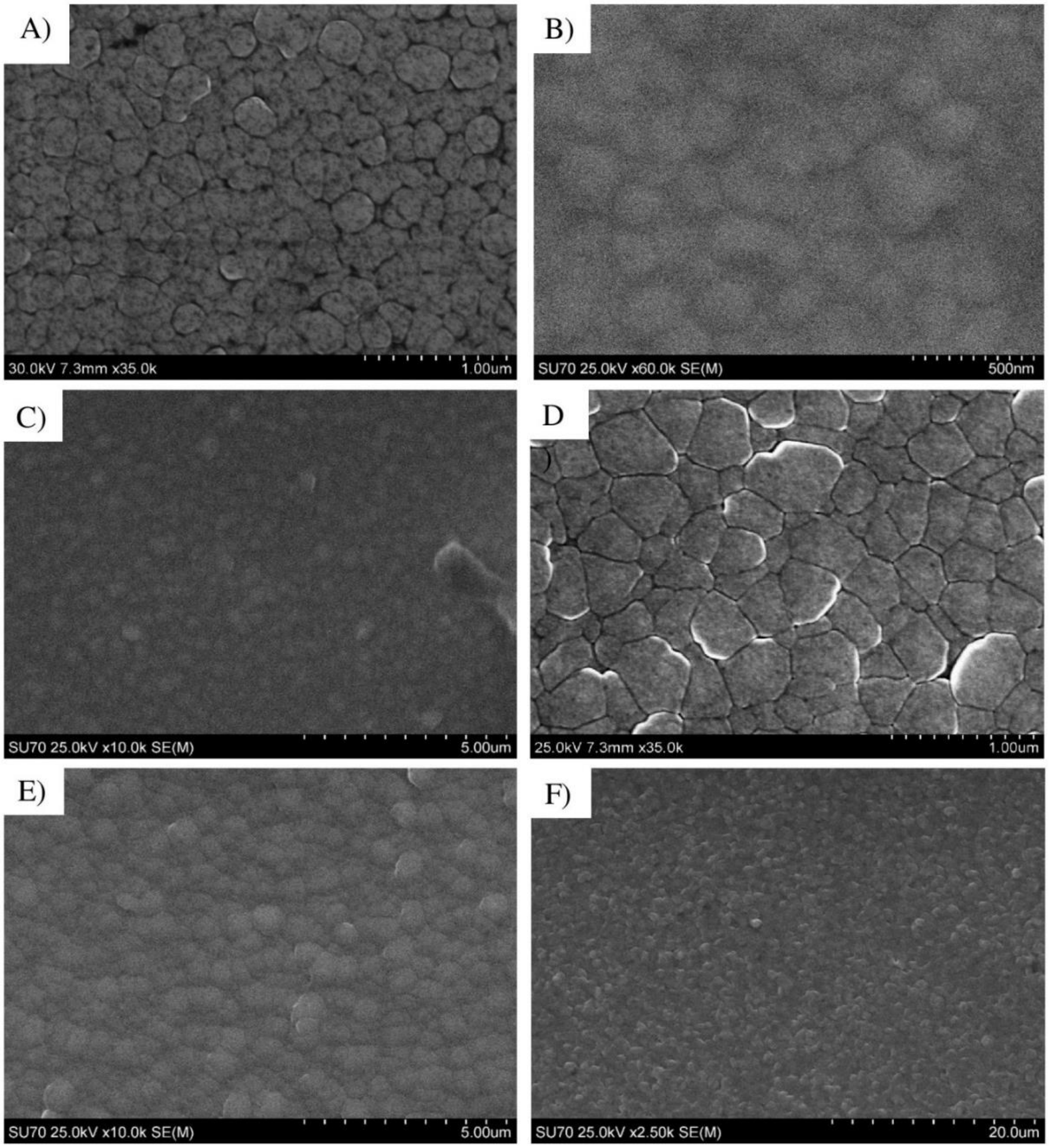

Figure 2.4 SEM image from surface of as-deposited Al/Ti NMMs.

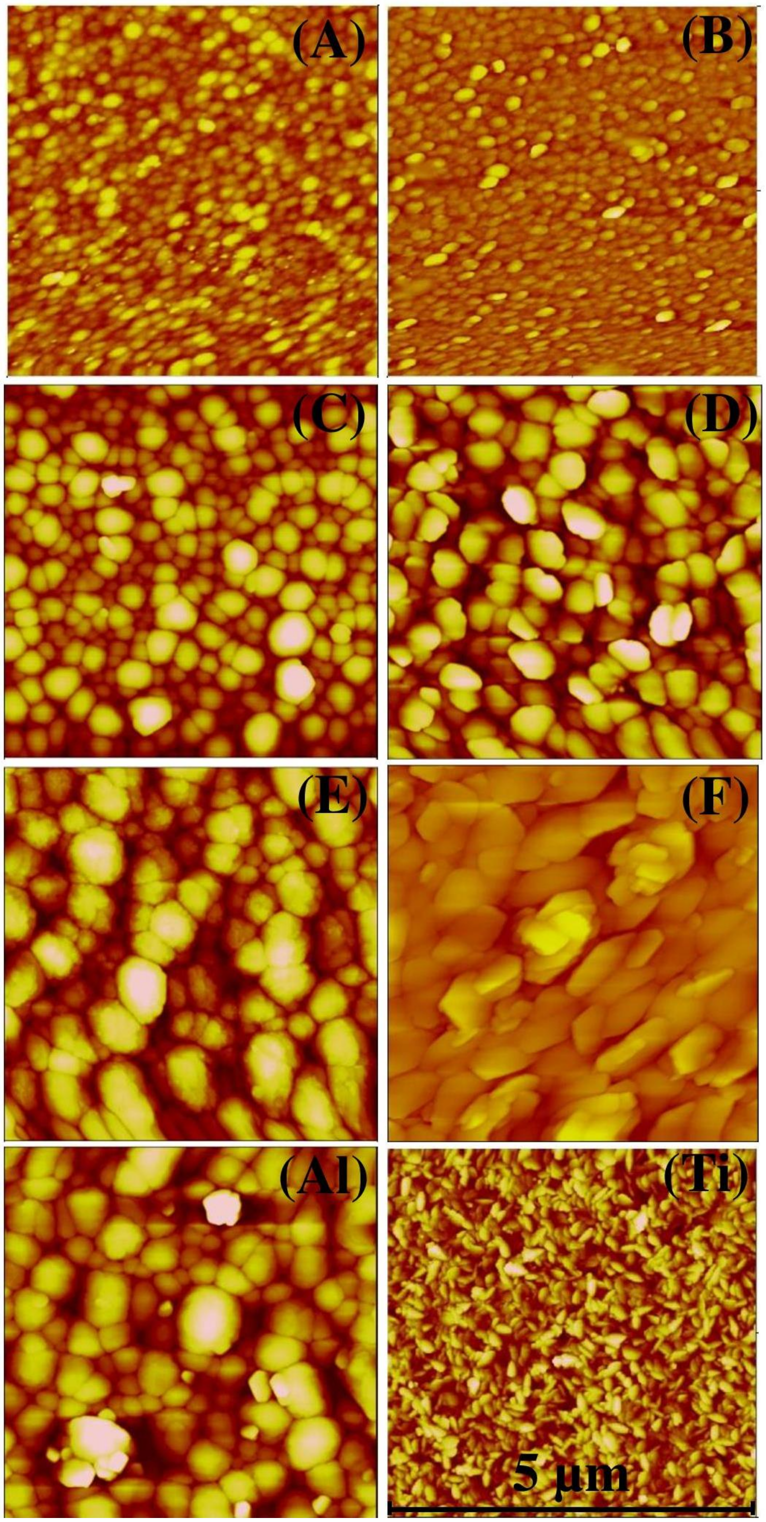

Figure 2.5 AFM images of specimens. NMM A, B, C, D, E, F, monolithic aluminum and monolithic titanium respectively shown as a, b, c, d, e, f, g and h. All scans were performed over areas of 5 × 5 µm^2.

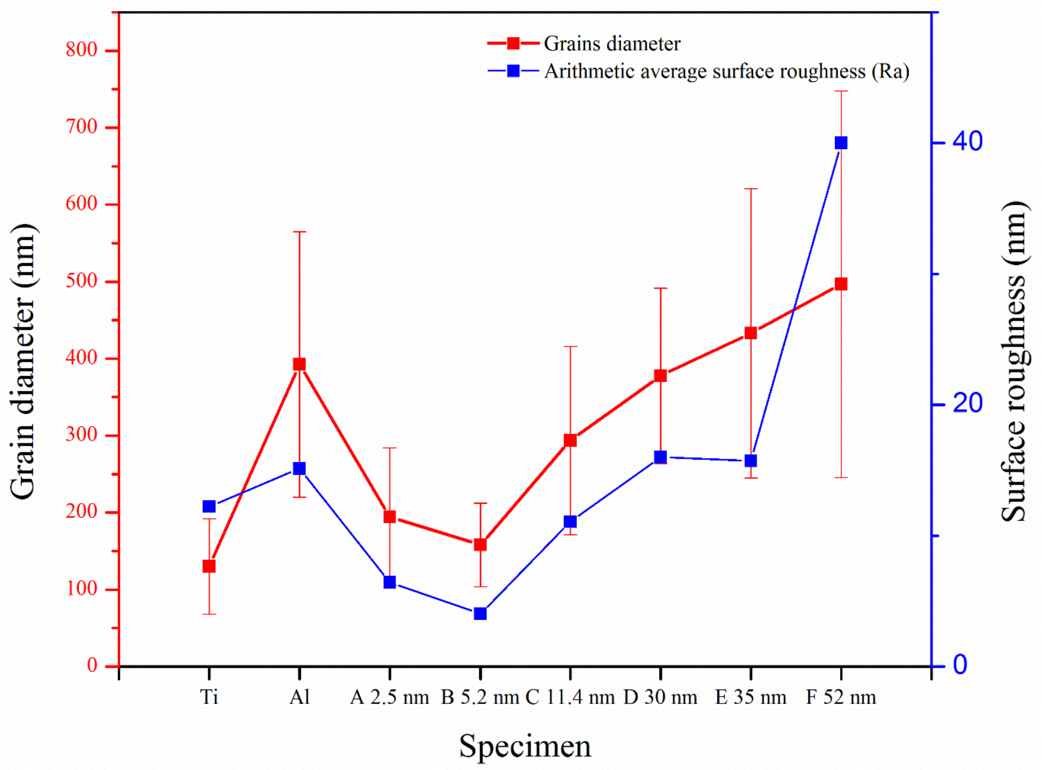

Figure 2.6 Arithmetic average of surface roughness and grain size of as-deposited samples. Grain size and surface roughness demonstrate a similar trend for both NMMs and monolithic specimens.

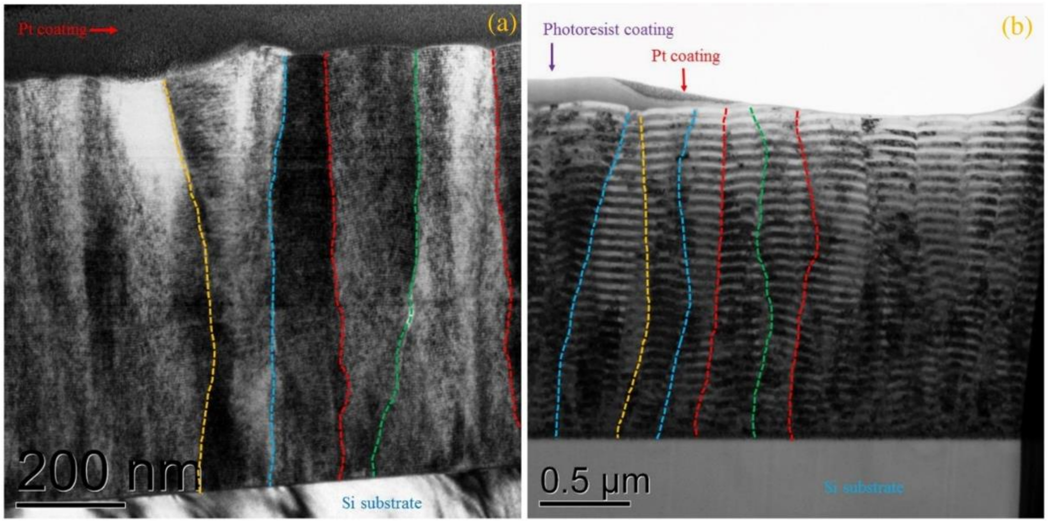

Figure 2.7 TEM images from the cross section of specimen (a) A and (b) D respectively.

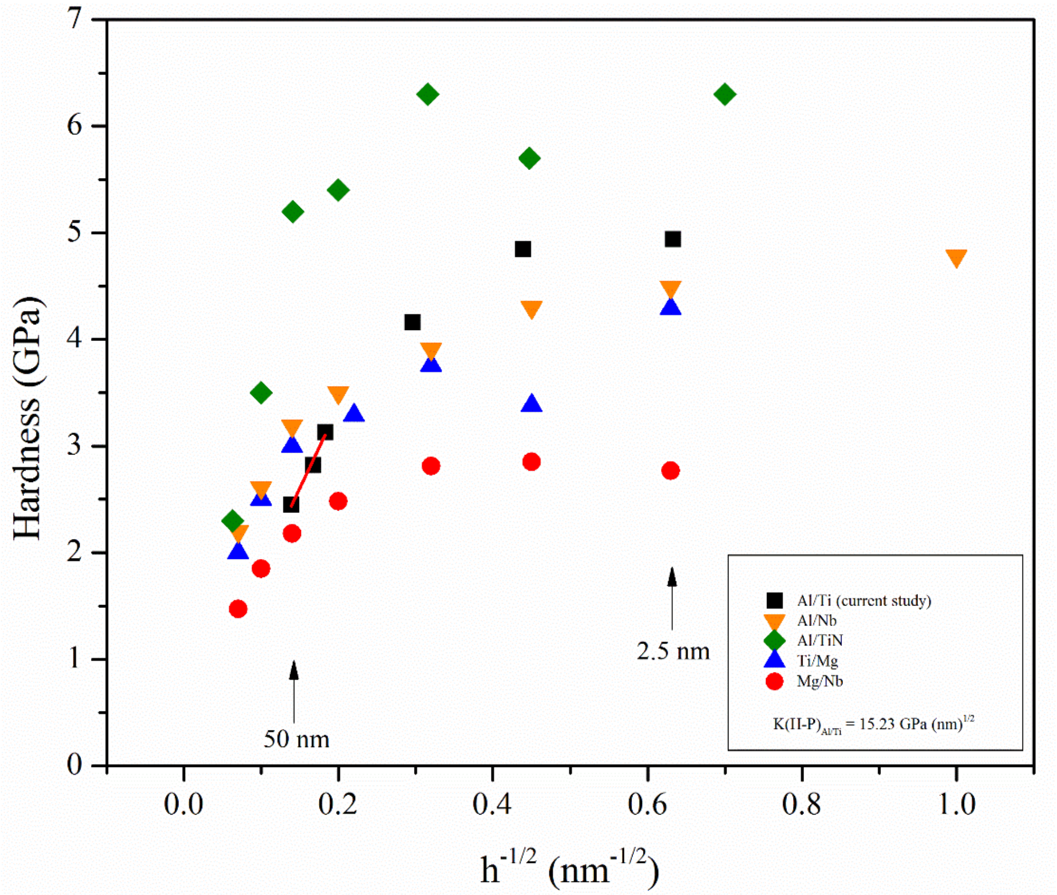

Figure 2.8 Summary of nanoindentation results from this study (black squares) with other NMMs containing Al or Ti layers.

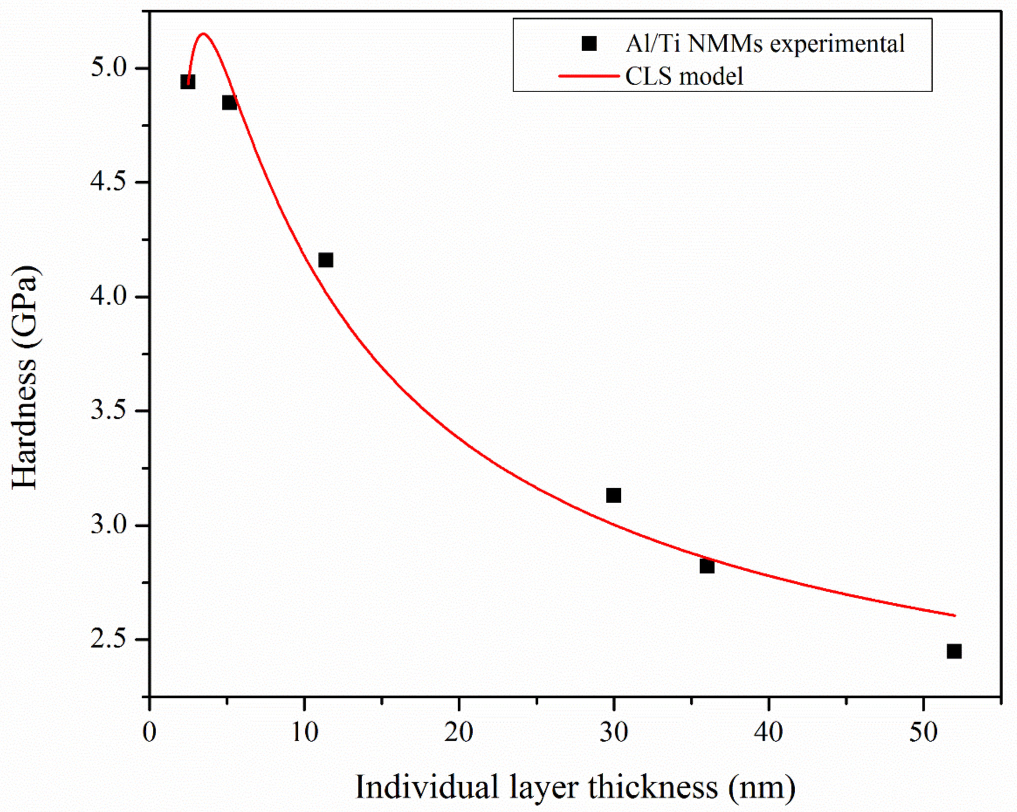

Figure 2.9 Hardness of Al/Ti NMMs v.s. individual layer thickness of all NMMs. The scattered data corresponds to experimental measurents and the solid line corresponds to predications by CLS model.

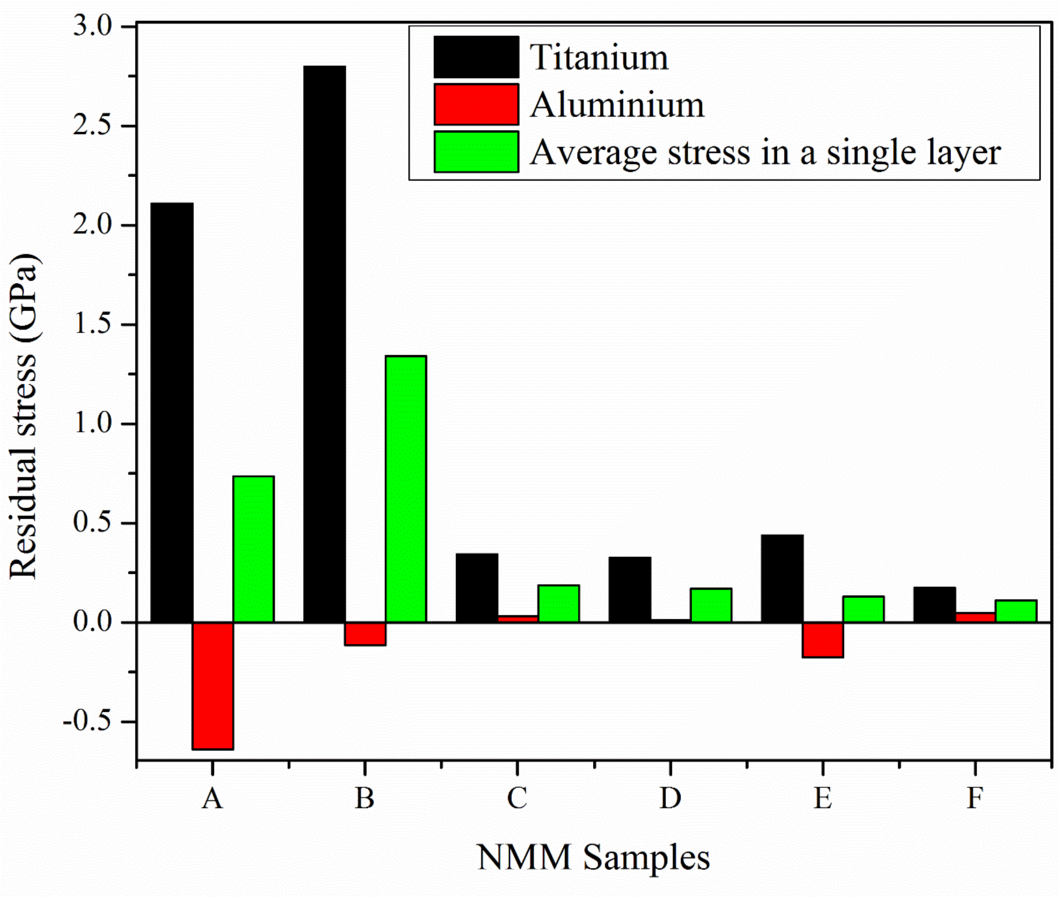

Figure 2.10 Summary of residual stress measured from XRD analysis for both aluminum and titanium phases of all NMMs.

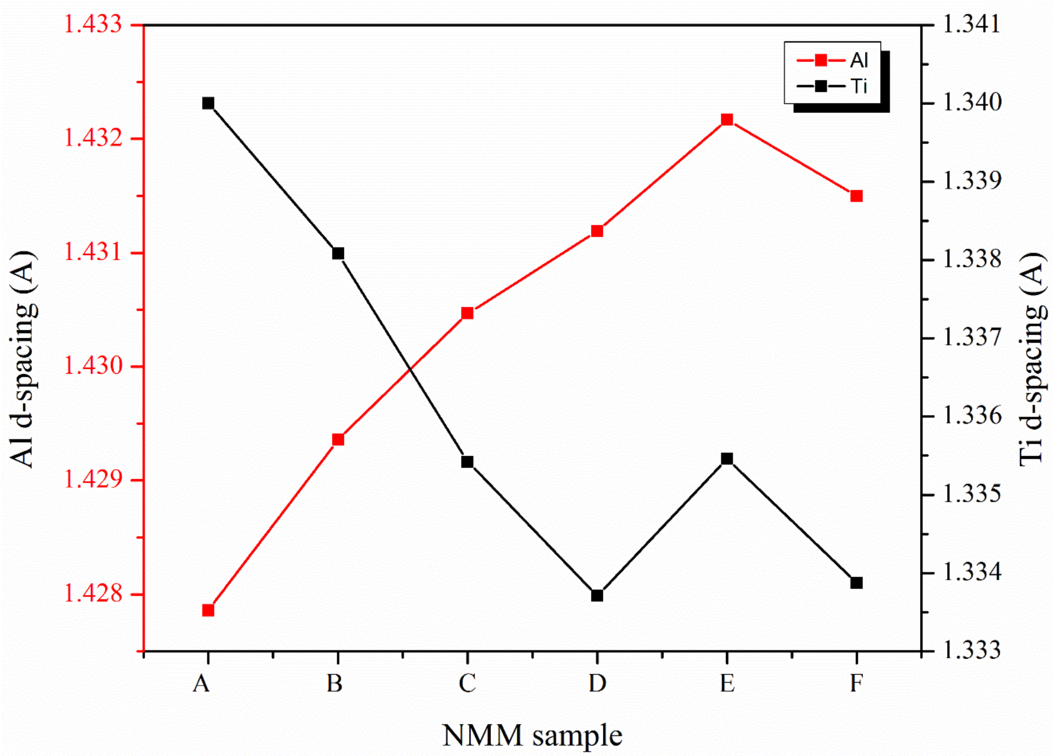

Figure 2.11 Summary of d-spacing of Al and Ti layers for all Al/Ti NMMs. Scans were performed at ψ = 0.

CHAPTER 3: NANOWEAR BEHAVIOR OF AL/TI NMMS

3.1 Note to Reader

Portion of this chapter has been previously published in the journal of Surface and Coating Technology, Volume 53, Issue 18, October 2005, Pages 4817–4824, and have been reproduced with permission from Elsevier. Permission is included in Appendix A.1.4.

3.2 Introduction

Nanostructure metallic multilayers (NMMs) are widely used as protective coatings due to their excellent mechanical properties [1, 2], corrosion resistance [3-5], and wear resistance [6]. Although there are extensive studies on the structural and mechanical properties of NMMs [6-8], those on the tribological studies of NMMs, especially Al/Ti NMMs remain limited [9, 10]. In tribology, one of the most implemented definitions for wear has been proposed by Archard [11], relating the mechanical wear rate to material's hardness, wear coefficient and normal load. Based on this definition, material hardness (H) and wear rate (W) have an inverse relationship ($W \propto H^{-1}$). This law has been found to be highly successful for monolithic bulk materials during dry sliding wear. However, it remains unclear how does hardness of the NMMs affect its wear resistance. In addition, it is still unknown how does the individual layer thickness affect the microstructure evolution and wear resistance of NMMs.

In the current study, two representative Al/Ti NMMs with 2.5 nm and 30 nm individual layer thicknesses are chosen as the test samples. Nanowear behavior of the two NMMs and their corresponding microstructure evolution were evaluated. This study will address the following topics: (1) characterization of microstructure of as-deposited Al/Ti NMMs with 2.5 and 30 nm layer thickness, (2) investigating the tribological and mechanical properties of NMMs through nanowear and nanoindentation tests, and (3) establishing the relationship between the mechanical and tribological properties through post-wear material characterizations.

3.3 Experimental Procedure

Al/Ti NMMs with equal-spaced Al and Ti layers were deposited on Si (100) substrates in a modified SFI cluster sputter tool using an Eratron 8210 DC power supply. Two types of NMMs were deposited, hereafter denoted as AT2.5 and AT30 (as listed in Table 3.1), with individual layer thicknesses of 2.5 nm and 30 nm and total film thickness of 930 ± 16 nm and 1.8 ± 0.02 μm, respectively. The arithmetic average surface roughness (Ra) of AT2.5 and AT30 is 5.96 nm and 8.67 nm, respectively, measured using Digital Instruments atomic force microscopy.

Grazing incidence x-ray diffraction (GIXRD) was performed using PANalytical X'Pert PRO diffractometer (Cu Kα, 154.06 pm) at 45 kV and 40 mA with an incidence angle of 3° and step size of 0.025°. The penetration depth (PD, the depth at which the intensity is attenuated by a factor of 1/e) was estimated from PD = $\sin\alpha/\mu$ [12], where α is the grazing incidence angle and μ is the linear adsorption coefficient, ~ 523.8 cm^{-1} estimated from $Al_{50}Ti_{50}$ composite [13]. The calculated PD is ~ 1.0 μm, comparable to the total film thickness and much larger than the individual layer thickness of both samples. Sample surfaces were examined using a Hitachi SU70 scanning electron microscopy (SEM) at accelerating voltage of 30 kV. Electron backscattered diffraction (EBSD) analysis was performed on a JEOL ARM transmission electron microscope (TEM) operated at 200 kV coupled with Topspin data acquisition system. The phase and orientation mappings were obtained using ASTAR software with a precession angle of 0.5° and a step size of 5 nm. TEM analysis was performed using TECNAI G2 in bright-field (BF), dark-field

(DF), and selected area diffraction (SAD) modes. TEM samples were prepared using the standard lift-out method in a FEI Quanta 200 focused ion beam (FIB) microscope.

Film hardness and elastic modulus were measured using a Hysitron triboindenter Ti900 with a Berkovich tip following the Oliver and Pharr method [14]. The tip area function was calibrated using a standard fused quartz sample. For each nanoindentation test, a trapezoidal loading profile was used with 2 or 3 mN maximum load, 2 sec holding time, and 3 sec loading/unloading time. This maximum load was chosen to ensure that the total penetration depth was less than 15% of the total sample thickness to minimize the substrate effect [15]. Average spacing between the indents was kept at least 8 μm apart to minimize indentation interactions.

Nanowear tests were performed using the triboindenter with a 1 μm cono-spherical tip. Wear tests were performed under 30, 60 and 93 μN normal loads and up to 10 cycles over areas of 2×2 μm^2. Wear volume (V) is calculated by multiply the wear area by the wear scar height, which was determined from the height difference between the unworn and worn surfaces using Hysitron Triboview software. Under a specific normal load (F), the wear rate (w) is defined as the ratio between wear volume and the number of cycles (n). Post-wear nanoindentation tests were performed on selected samples with worn area of 35×35 μm^2 to probe the subsurface hardness, using the same loading profiles defined previously in the nanoindentation tests.

3.4 Results

3.4.1 Microstructure of As-Deposited Al/Ti NMMs

GIXRD line scans of as-deposited AT2.5 and AT30 are shown in Fig. 3.1. The high intensity peak located at $2\theta = 56.2°$ is ascribed to Si (311) from the substrate. It can be seen that for both samples, fcc Al phase co-exists with hcp Ti phase. The peak at $2\theta \approx 38.5°$ arises from superposition of Al (111) and Ti (00.2). The lattice constants are $a_{Al} = 4.046$ Å for fcc-Al, and a_{Ti}

= 2.969 Å and c_{Ti} = 4.666 Å for hcp-Ti. Significant peak-broadening was observed in AT2.5 due to its ultra-fine layer thickness and, very likely, bi-axial micro strain [16]. Unfortunately, a good estimation of the micro strain is not possible here due to insufficient Bragg diffractions and overlapping of Al(111) and Ti (00.2). SEM images of the as-deposited samples are shown in Fig. 3.2(a) and (b). The surface morphology of both samples consists mainly of spherical nodules around 200–500 nm in diameter. Cross-sectional TEM images of AT2.5 and AT30 in Fig. 3.2(c) and (d) reveal the equal-spaced layered structure, where the bright and dark stripes correspond to the Al and Ti layers, respectively. The average layer thickness (h) is 2.5 ± 0.3 nm and 30 ± 1.5 nm for AT2.5 and AT30, respectively, measured from cross-sectional TEM images. Low magnification TEM images (not shown here) reveal that through thickness columnar grains are present for both samples, similar to those reported previously [17]. The in-plane grain size (d) is ~ 140 nm for both samples, much larger than their respective layer thicknesses. Thus, in the present study, the layer thickness is considered as the critical structural length scale that governs the mechanical and tribological behavior [18].

HRTEM image of AT30 in Fig. 3.3(a) shows an orientation relationship of Al (111) || Ti (00.1), both parallel to the interface plane. The interface is semi-coherent, with out-of-plane edge dislocations separated by ~ 2.44 ± 0.65 nm (see IFFT images in Fig. 3.3(b) and (d)), in agreement with a previous report [19]. These quasi-periodically spaced edge dislocations also lead to a misorientation of ~ 3.2^{o} between Al (111) and Ti (00.1) planes. The HRTEM image in Fig. 3.3(c) shows Al (200) || Ti (10.1), both inclined to the interface plane at an angle of ~55^{o}, with a measured misfit strain of ~ 8%. According to the Al/Ti multilayers bi-phase diagram [19], the interface between the hcp-Ti and fcc-Al layer transforms from incoherent to coherent when the bilayer thickness becomes smaller than ~ 12.5 nm [19]. However, for AT2.5 (with a bilayer thickness of

~ 5 nm), a coherent interface is not observed. Instead, semi-coherent interfaces with dislocation spacing of ~ 2.23 ± 0.50 nm are observed. Interestingly, Fig. 3.4(b) shows that the hcp-Ti layer of as-deposited AT2.5 exhibited fcc structure (Fig. 3.4(b) and (c)) under TEM analysis. Similar polymorphic transformation was reported previously in Al/Ti [20] and Ni/Ti [21] multilayers with h_{Ti} around 30 − 500 nm, where the as-deposited hcp-Ti layers transformed to fcc structure after ion milling during TEM sample preparation. The measured lattice constant ratio between the fcc-Al and fcc-Ti phases is $a_{Ti}/a_{Al} = 1.08$, very close to the value of 1.09 reported previously for Al/Ti multilayers [20]. In addition, the HRTEM image and SAD patterns in Fig. 3.4 indicate that the fcc-Ti and fcc-Al layers were twinned with noncoherent twin boundaries, as indicated by white arrows in Fig. 3.4(a).

3.4.2 Nanoindentation of As-Deposited Al/Ti NMMs

Representative loading/unloading curves of AT2.5 and AT30 are shown in Fig. 3.5. No obvious “pop-in” was observed from the load-displacement curves of both samples, indicating the absence of macroscopic shear band formation. A higher penetration depth is observed for AT30 than AT2.5 under the same loading condition, indicating a higher resistance to plastic deformation of the latter. The reduced Young’s modulus (E_r) and hardness (H) of as-deposited samples are listed in Table 3.1. In particular, AT2.5 exhibits a high hardness of 4.59 GPa, ~ 50% of the theoretical strength (~ G/10) of a $Al_{50}Ti_{50}$ composite. It is also interesting to note that AT2.5 exhibits a smaller E_r/H value than AT30, which indicates a higher wear resistance of the former sample [11, 22, 23].

Insets in Fig. 3.5 show the post-indentation surface topographies of both samples. Whereas indents of AT30 exhibit high contrast from the undeformed surface, those of sample AT2.5 are hardly visible due to the small penetration depths. After careful SEM analysis, it was not possible to differentiate the indents of AT2.5 from the as-deposited surface roughness. Thus, post-indentation microstructure characterization was performed only for AT30. Fig. 3.6(b) shows the phase map of the box area in Fig. 3.6(a), where the red and green colors represent the fcc-Al and hcp-Ti phases, respectively. It can be seen that immediately below the indent, Al layer thicknesses are reduced to ~ 10 nm (corresponds to a local compressive strain ~ 67%), while Ti layer thicknesses remain almost unaffected. For multilayers consisting of two phases with different strengths, plastic deformation typically occurs in the softer phase first until the stress is high enough to transfer or generate dislocations in the harder phase. Thus, in the present study, it is not surprising that plastic deformation is mainly accommodated by the softer Al layers. In addition to layer compression, several shear bands (SBs) are observed, as indicated by the dashed lines in Fig. 3.6(b). During co-deformation of multilayers, shear bands are often observed due to the difference in flow stresses and hardening behaviors of the adjacent layers, such as those seen in the Al/W [24] and Cu/Ta multilayers [25, 26]. Fig. 3.7 shows the orientation maps of AT30 after nanoindentation. From Fig. 3.7(b), it can be seen that $(111)_{Al}$ || $(00.2)_{Ti}$ || film growth direction (y-axis as defined in Fig. 3.6(a) inset). This is not surprising as preferred growth in <111> and <00.2> directions for fcc and hcp thin films have been commonly observed to minimize surface energy during deposition [16]. Just below the indent, grains with orientations different from the original were observed, as indicated by the white arrows in Fig. 3.7(c). The orientation change of these sub-grains clearly indicates local grain rotation and formation of cell boundaries perpendicular to the layer interfaces.

3.4.3 Nanowear Tests and Subsurface Microstructure Evolution

Fig. 3.8 shows typical surface topographies of the two samples after 10 cycles of wear tests under 93 μN load. Surface height profiles in Fig. 3.8(c) show that both the wear scar depth and the pile-up height are lower for AT2.5, indicating smaller material loss and higher wear resistance than AT30. Fig. 3.9(a) and (b) shows that the wear rate is initially high during the running-in period, which then reaches steady-state wear after ~ five cycles. Fig. 3.9(c) shows the wear rates increase almost linearly with the applied load, in agreement with Archard's law [11]. In addition, the wear rate of AT30 is at least two times that of AT2.5, as expected due to its lower hardness and higher E_r/H ratio [27]. It was noticed that increasing the wear track dimensions from 2 × 2 μm^2 to 35 × 35 μm^2 leads to an increase of wear scar depth. This is not surprising given that the conical tip radius (1 μm) is close to the smaller wear track dimensions. For example, the wear scar depth of AT30 after 10 cycles of wear under 93 μN load increased from ~ 110 nm to ~ 650 nm when the wear track dimension was changed from 2 × 2 μm^2 to 35 × 35 μm^2.

Fig. 3.10 shows a montage BF cross-sectional TEM image of AT30 after 10 cycles of wear tests under 93 μN load. The worn and unworn areas and the pile-up can be seen clearly. Within the top ~ 100 – 150 nm, a severely plastically-deformed layer (SPDL) was observed. During nano contacts, the plastic zone size c can be estimated from Johnson's spherical cavity model as [28]

$$c = \sqrt{\frac{3P}{2\pi\sigma_y}}, \quad (1)$$

where P is the normal load, and σ_y is the yield strength (approximated as $\frac{1}{3}H$ from Tabor relationship). The estimated c from eqn. (1) is ~ 207 nm for AT30, close to the size of SPDL observed by TEM. Within the SPDL, significant layer compression and shearing are observed, and the well-defined interfaces between Al and Ti layers are lost. Wear debris and pile-ups are mainly generated by material removal from the SPDL. Fig. 3.11(a) and (b) show the BF and DF TEM images of a wear debris attached to the unworn surface of AT30. It can be seen that the majority of the debris contains severely-refined layers, with the minimum layer thickness ~ 3.8 nm for both the Al and Ti layers, corresponding to a local compressive strain of ~ 87%. The interfaces of the deformed layers are wavy due to shear band formation, as shown in the pile-up in Fig. 3.11 (c) and (d). A similar wavy layered structure also was reported in dual phase Ag-Cu alloy after severe sliding wear [29]. In addition, vortex-like features are often observed in the SPDL, as shown in Fig. 3.11(c) and (d), which resembles the Kelvin-Helmoltz instability [30]. Using molecular dynamics simulations, Kim et al. [30] have demonstrated that these subsurface vorticities was developed due to wear-induced shear instability at the contacting surfaces.

The subsurface microstructure of AT2.5 was drastically different from AT30. Fig. 3.12 shows the TEM images of AT2.5 after 10 cycles of wear under 93 μN load. Unlike AT30, no shear band formation was observed and all layers remained planar. The SPDL is ~ 30 nm, significantly smaller than the plastic zone size of ~ 170 nm estimated from eqn. (1). HRTEM image in Fig. 3.12 (c) shows that just below the surface, the contrast between adjacent Al and Ti layers diminished, indicating the interfaces are more relaxed with fewer misfit dislocations. IFFT images at depths ~ 10 nm (inset 1 in Fig. 3.12 (c)) and 40 nm (inset 2 in Fig. 3.12 (c)) confirm that the lattice mismatch and the edge dislocation density are reduced near the top of the SPDL. These results suggest that the non-equilibrium interfaces of Al/Ti NMMs, which contain excess free volume and dislocations, were relaxed during abrasive wear, similar to the relaxation of non-equilibrium grain boundaries after cyclic mechanical loading [16]. Finally, it is noted that while the γ-AlTi and Al_3Ti intermetallic phases were found in Al/Ti NMMs after ion irradiation [10] or high pressure torsion [31], no intermixing were observed after indentation or wear in the present work.

3.5 Discussion

3.5.1 Phase Stability of Ti in Al/Ti NMMs

An interesting observation of the present work is that the Ti layers of as-deposited AT2.5 transform from hcp to fcc structure after TEM sample preparation. A similar behavior was not observed in AT30, indicating that phase stability of Ti is related to the layer thickness of NMM. Even though fcc-Ti is not predicted by the equilibrium phase diagram, metastable fcc-Ti has been reported in epitaxial Ti thin films (with < 50 nm film thickness) [32] and Ti powders after high energy mechanical milling [31], where compressive residual stresses were both present. Chakraborty et al. [16] showed that a compressive stress of more than 2.5 GPa was developed in Ti at low film thicknesses. This high stress is likely to generate Shockley partials on basal planes that can alter the stacking sequence, similar to what occurred during martensitic phase transformation. The phase stability of fcc-Ti and hcp-Ti can be further understood by considering the change of total free energy, which includes the change in bulk free energy, elastic strain energy, and surface free energy, during the hcp to fcc transformation. At large film thicknesses, the bulk free energy term dominates and hcp-Ti is more stable (~ 0.065 - 0.07 eV/atom lower than fcc-Ti [16]); at low film thicknesses, the elastic strain energy and surface free energy dominates and fcc-Ti becomes more stable. A previous study [16] showed that the strain energy density of fcc-Ti thin film is about one order of magnitude lower than that of hcp-Ti at thicknesses smaller than 144 nm. Thus, there exists a critical film thickness, below which fcc-Ti is more stable than hcp-Ti. For Al/Ti multilayers, this critical film thickness was found to increase with decreasing volume fraction of Ti [19]. According to Banerjee et al. [19], for Al/Ti multilayers with 50% volume fraction of Ti, the estimated critical layer thickness is around 1.4 – 1.8 nm, which is comparable to the layer thickness of AT2.5, and much smaller than that of AT30. Thus, in the present work, metastable fcc-Ti was seen only in the former.

3.5.2 Al/Ti Interface Structure

An orientation relationship of $(111)_{Al}$ || $(00.2)_{Ti}$ || interface plane was observed in both as-deposited samples (note the $(00.2)_{Ti}$ plane of AT2.5 transformed to $(111)_{Ti}$ after TEM sample preparation). The interfaces were always semi-coherent, separated by edge dislocations with spacing around 2.2–2.4 nm (see section 3.1 for details). For NMMs, the degree of interface coherency depends on the layer thickness, and there exists a critical layer thickness (h_c) for epitaxial growth. If $h \leq h_c$, the interface is fully coherent; if $h > h_c$, dislocations will be formed to relax the misfit strain, and semi-coherent or incoherent interfaces will be formed. This critical layer thickness h_c can be estimated as [33]

$$h_c = \frac{b}{2\pi\varepsilon_m} \ln\left(\frac{\sqrt{2}h_c}{b}\right), \quad (2)$$

where b is the Burgers vector and ε_m is the lattice misfit strain. In the current Al/Ti system, assume <a> type Burgers vector for Ti, $\vec{b} = \frac{1}{3} < 11\bar{2}0 >$ = 0.17 nm, the misfit strain ε_m = 8%, the calculated value of h_c is 0.43 nm, comparable to a few monolayers. Previous experimental work shows that Ti grows epitaxially on Al (100) up to 5.5 monolayers [21], and on Al (111) up to 2 monolayers [34]. This small h_c indicates that misfit dislocations are inevitable to accommodate for the misfit strain for Al/Ti NMMs with nanometer scale layer thicknesses. The spacing between misfit dislocations, λ, can be estimated as $\lambda = \frac{b}{\varepsilon_m}$ = 2.1 nm, which agrees very well with the HRTEM observation.

3.5.3 Wear Induced Subsurface Work-Hardening

As presented in section 3.3, wear leads to characteristically different microstructure evolutions for AT2.5 and AT30. To evaluate how these microstructure evolutions affect the subsurface mechanical properties, nanoindentation tests were performed on worn surfaces of AT2.5 and AT30 after wear tests under 60 µN normal load up to five cycles. The results are shown in Fig. 3.13. It can be seen that both AT2.5 and AT30 experienced significant work-hardening, reaching a hardness of 6.80 ± 0.16 GPa and 4.35 ± 0.17 GPa, respectively, after five cycles of wear. Quite remarkably, this subsurface hardening is more significant for AT2.5, where the hardness increased by ~ 30% despite its small microstructural change. As discussed in the introduction, at layer thickness of 2.5 nm, the flow stress is related to the interface barrier stress, which is highly sensitive to the interface structure. As shown in Fig. 3.12 (c), with decreasing distance from the surface, a decrease of interface dislocation density was observed. In other words, wear increased the interface coherency right below the contact surface. Thus higher coherency stress needs to be overcome for dislocations to transmit to the other layers [32]. For AT30, the hardness increased by ~ 16 % after five cycles of wear. At this layer thickness, the operative strengthening mechanism is CLS (or modified CLS). Consider the greatest layer thickness refinement (~ 3.8 nm) in the SPDL of AT30, it can be estimated that the maximum strength is increased by ~ 2.1 times compared to the bulk material. However, since these ultrafine structures were only observed in the topmost subsurface material, the measured hardness is much lower and represents an average value over the entire SPDL. Finally, it is worth noting that Al/Ti NMM studied here is a promising lightweight high strength material. Given the low density of Al and Ti, the estimated specific strength of Al/Ti NMM is around 320–500 kN·m/kg (assuming a Tabor factor of three), well in excess of steel (130 kN·m/kg), Al-6061 (110 kN·m/kg), and Ti-6Al-4V (240 kN·m/kg) [35].

3.6 Conclusions

In summary, equal-spaced Al/Ti NMMs with individual layer thickness (*h*) of 2.5 and 30 nm were deposited on Si substrate by physical vapor deposition. Semi-coherent interfaces between the Al and Ti layers were observed in both samples, with an orientation relationship of Al (111) || Ti (00.2), parallel to the interface plane. The misfit strain was ~ 8%, and the nominal misfit dislocation spacing was ~ 2.2–2.4 nm for both samples. The hcp-Ti layer was unstable at lower layer thicknesses (2.5 nm) and transformed to metastable fcc structure after TEM sample preparation. Both hardness and wear resistance increased with decreasing layer thickness. The wear rate approached a steady state after five cycles and scaled linearly with applied load, in agreement with Archard’s law. Wear induced severe plastic deformation of the subsurface material and led to the formation of a SPDL of 100–150 nm and 30 nm for AT30 and AT2.5, respectively. The deformation mechanism was found to strongly depend on layer thickness. At $h = 30$ nm, severe compression and shearing of Al and Ti layers led to shear band and vorticities formation in the SPDL. At $h = 2.5$ nm, wear-induced plastic deformation relaxed the interface and lowered misfit dislocation density. These relaxed interfaces of AT2.5 led to an increase in surface hardness by ~ 30% after five cycles of wear.

3.7 References

1. Fu, E.G., et al., *Mechanical properties of sputtered Cu/V and Al/Nb multilayer films.* Materials Science and Engineering: A, 2008. **493**(1–2): p. 283-287.

2. McKeown, J., et al., *Microstructures and strength of nanoscale Cu–Ag multilayers.* Scripta Materialia, 2002. **46**(8): p. 593-598.

3. Barshilia, H.C., et al., *Corrosion behavior of nanolayered TiN/NbN multilayer coatings prepared by reactive direct current magnetron sputtering process.* Thin Solid Films, 2004. **460**(1–2): p. 133-142.

4. Creus, J., et al., *Mechanical and corrosion properties of dc magnetron sputtered Al/Cr multilayers.* Surface and Coatings Technology, 2008. **202**(16): p. 4047-4055.

5. Guan, X., et al., *Toward high load bearing capacity and corrosion resistance Cr/Cr2N nano-multilayer coatings against seawater attack.* Surface and Coatings Technology, 2015. **282**: p. 78-85.

6. Yonekura, D., J. Fujita, and K. Miki, *Fatigue and wear properties of Ti–6Al–4V alloy with Cr/CrN multilayer coating.* Surface and Coatings Technology, 2015. **275**: p. 232-238.

7. Yang, Y.-S., T.-P. Cho, and Y.-C. Lin, *Effect of coating architectures on the wear and hydrophobic properties of Al–N/Cr–N multilayer coatings.* Surface and Coatings Technology, 2014. **259, Part B**: p. 172-177.

8. Xu, S., et al., *Wear resistance of superior structural WS2–Sb2O3/Cu nanoscale multilayer film.* Materials & Design, 2016. **93**: p. 494-502.

9. Banerjee, R., et al., *Phase stability in Al/Ti multilayers.* Acta Materialia, 1999. **47**(4): p. 1153-1161.

10. Milosavljevic, M., et al., *Ion irradiation induced Al-Ti interaction in nano-scaled Al/Ti multilayers.* Applied Surface Science, 2012. **258**(6): p. 2043-2046.

11. Archard, J.F., *Contact and Rubbing of Flat Surfaces.* Journal of Applied Physics, 1953. **24**(8): p. 981-988.

12. Josell, D., et al., *Tensile testing low density multilayers: Aluminum/titanium.* Journal of Materials Research, 1998. **13**(10): p. 2902-2909.

13. Yadav, S.K., et al., *First-principles study of shear behavior of Al, TiN, and coherent Al/TiN interfaces.* Journal of Applied Physics, 2012. **111**(8).

14. Oliver, W.C. and G.M. Pharr, *An improved technique for determining hardness and elastic modulus using load and displacement sensing indentation experiments.* Journal of Materials Research, 1992. **7**(06): p. 1564-1583.

15. Saha, R. and W.D. Nix, *Effects of the substrate on the determination of thin film mechanical properties by nanoindentation.* Acta Materialia, 2002. **50**(1): p. 23-38.

16. Rupert, T.J. and C.A. Schuh, *Mechanically driven grain boundary relaxation: a mechanism for cyclic hardening in nanocrystalline Ni.* Philosophical Magazine Letters, 2012. **92**(1): p. 20-28.

17. Ahuja, R. and H.L. Fraser, *Microstructural Transitions in Titanium-Aluminum Thin-Film Multilayers.* Journal of Electronic Materials, 1994. **23**(10): p. 1027-1034.

18. Misra, A., et al., *Deformation mechanism maps for polycrystalline metallic multiplayers.* Scripta Materialia, 1999. **41**(9): p. 973-979.

19. Banerjee, R., S.A. Dregia, and H.L. Fraser, *Stability of f.c.c. titanium in titanium/aluminum multilayers.* Acta Materialia, 1999. **47**(15-16): p. 4225-4231.

20. Shectman, D., D. Vanheerden, and D. Josell, *Fcc Titanium in Ti-Al Multilayers.* Materials Letters, 1994. **20**(5-6): p. 329-334.

21. Saleh, A.A., et al., *Epitaxial growth of fcc Ti films on Al(001) surfaces.* Physical Review B, 1997. **56**(15): p. 9841-9847.

22. Tang, L., et al., *Dry sliding friction and wear behaviour of hardened AISI D2 tool steel with different hardness levels.* Tribology International, 2013. **66**(0): p. 165-173.

23. Siddharth Sharma, A., K. Biswas, and B. Basu, *Microstructure-hardness-fretting wear resistance correlation in ultrafine grained Cu–TiB2–Pb composites.* Wear, 2014. **319**(1–2): p. 160-171.

24. Xie, J.Y., et al., *Strain Rate Dependent Shear Banding Deformation in Al/W Nanomultilayers.* Integrated Ferroelectrics, 2013. **146**(1): p. 168-176.

25. Wang, F., et al., *Shear banding deformation in Cu/Ta nano-multilayers.* Materials Science and Engineering: A, 2011. **528**(24): p. 7290-7294.

26. Li, Y.P., J. Tan, and G.P. Zhang, *Interface instability within shear bands in nanoscale Au/Cu multilayers.* Scripta Materialia, 2008. **59**(11): p. 1226-1229.

27. Leyland, A. and A. Matthews, *Design criteria for wear-resistant nanostructured and glassy-metal coatings.* Surface and Coatings Technology, 2004. **177–178**(0): p. 317-324.

28. Kramer, D., et al., *Yield strength predictions from the plastic zone around nanocontacts.* Acta Materialia, 1998. **47**(1): p. 333-343.

29. Cai, W. and P. Bellon, *Subsurface microstructure evolution and deformation mechanism of Ag-Cu eutectic alloy after dry sliding wear.* Wear, 2013. **303**(1-2): p. 602-610.

30. Kim, H.J., S. Karthikeyan, and D. Rigney, *A simulation study of the mixing, atomic flow and velocity profiles of crystalline materials during sliding.* Wear, 2009. **267**(5-8): p. 1130-1136.

31. Bahmanpour, H., et al., *Microstructural evolution of cryomilled Ti/Al mixture during high-pressure torsion.* Journal of Materials Research, 2014. **29**(4): p. 578-585.

32. Abdolrahim, N., H.M. Zbib, and D.F. Bahr, *Multiscale modeling and simulation of deformation in nanoscale metallic multilayer systems.* International Journal of Plasticity, 2014. **52**: p. 33-50.

33. Matthews, J.W. and A.E. Blakeslee, *Defects in epitaxial multilayers: I. Misfit dislocations.* Journal of Crystal Growth, 1974. **27**(0): p. 118-125.

34. Kim, Y.W., et al., *Growth and structure of hcp Ti films on Al(111) surfaces.* Surface Review and Letters, 1999. **6**(5): p. 775-780.

35. *ASM Metals Reference Book, third ed.*, ed. M. Bauccio. 1993, Ohio: ASM International.

3.8 Tables and Figures

Table 3.1 Summary of microstructure and mechanical properties of Al/Ti multilayers. Layer thickness (h) and in-plane grain size (d) were measured from TEM analysis. Mechanical properties including maximum penetration depth (h_{max}), hardness (H), and reduced modulus (E_r) were measured from nanoindentation under 2 − 3 mN load.

Sample	h (nm)	d (nm)	h_{max} (nm)	H (GPa)	E_r (GPa)	E_r/H
AT2.5	2.5 ± 0.3	138 ± 43	142.2 ± 8.0	4.59 ± 0.53	118.5 ± 7.8	25.8
AT30	30.0 ± 1.5	140 ± 30	214.1 ± 9.3	3.08 ± 0.25	116.7 ± 6.4	37.9

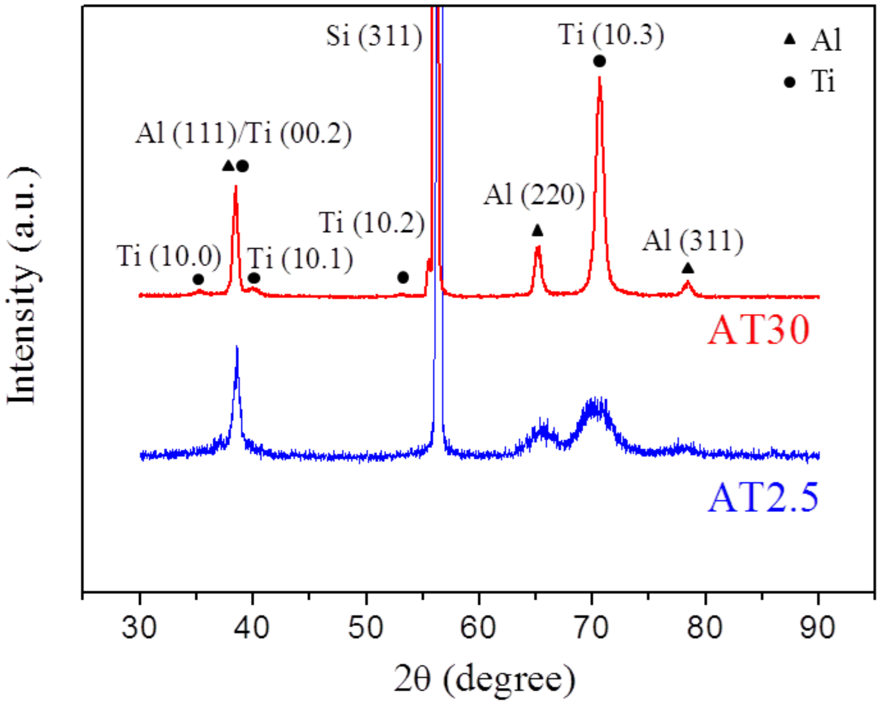

Figure 3.1 Grazing-incidence XRD line scans of as-deposited AT2.5 and AT30.

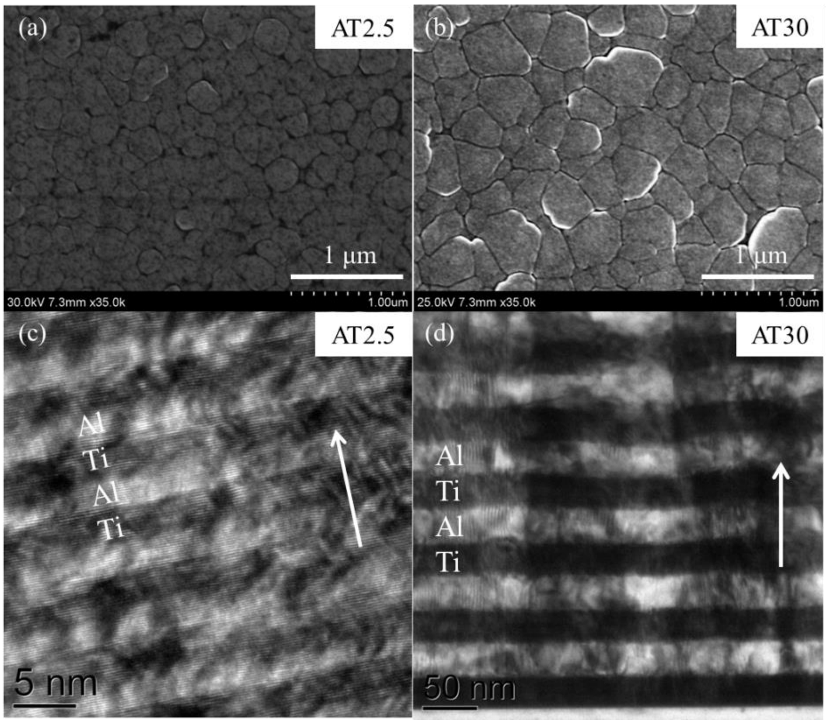

Figure 3.2 SEM images of surface morphology of as-deposited (a) AT2.5 and (b) AT30. Cross-sectional TEM images of as-deposited (c) AT2.5 and (d) AT30. Arrows in (c) and (d) indicate film growth direction.

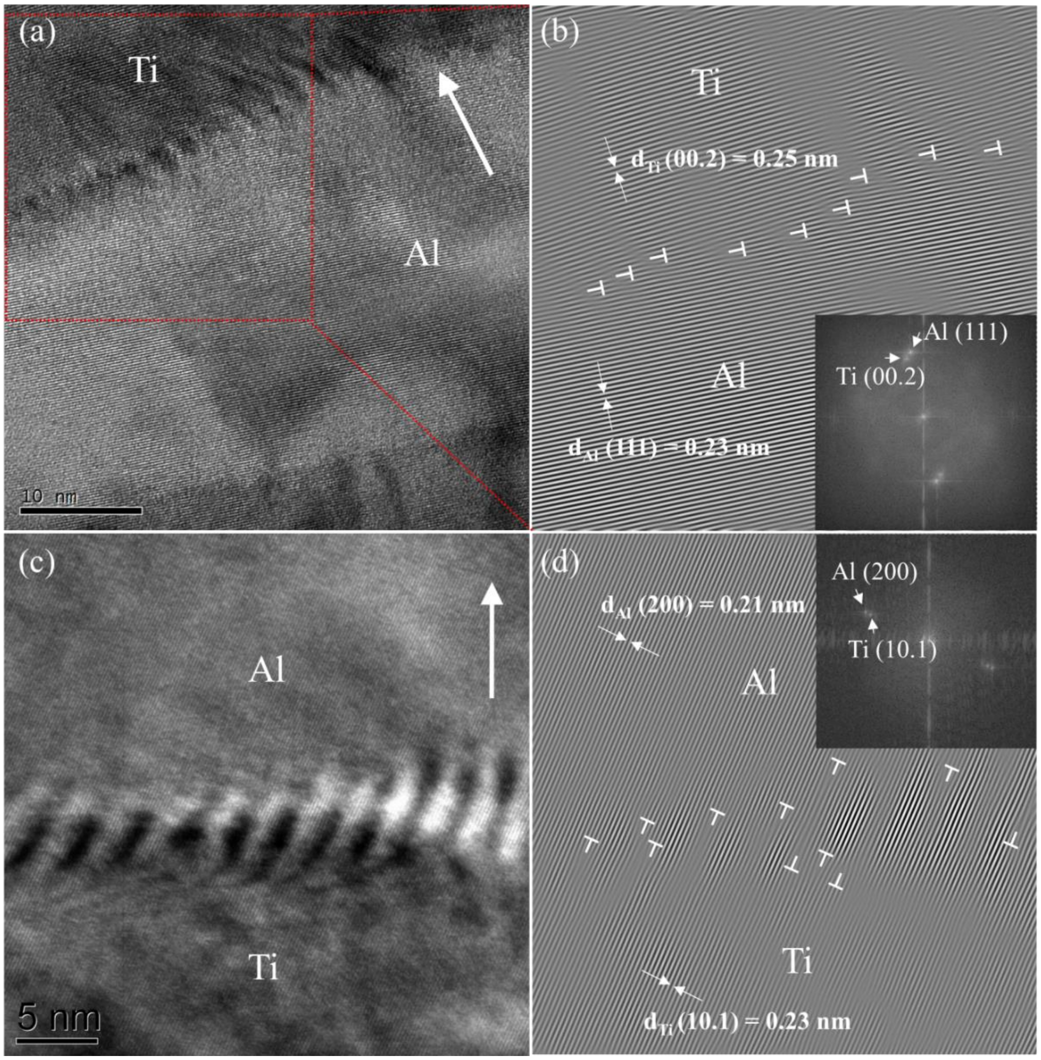

Figure 3.3 (a) and (c) HRTEM images of as-deposited AT30, (b) inverse fast Fourier transforms (IFFT) image of box area in (a), and (d) IFFT of image (c). Insets in (b) and (d) show the FFT of images (a) and (c), respectively. Arrow in (a) and (c) indicates film growth direction.

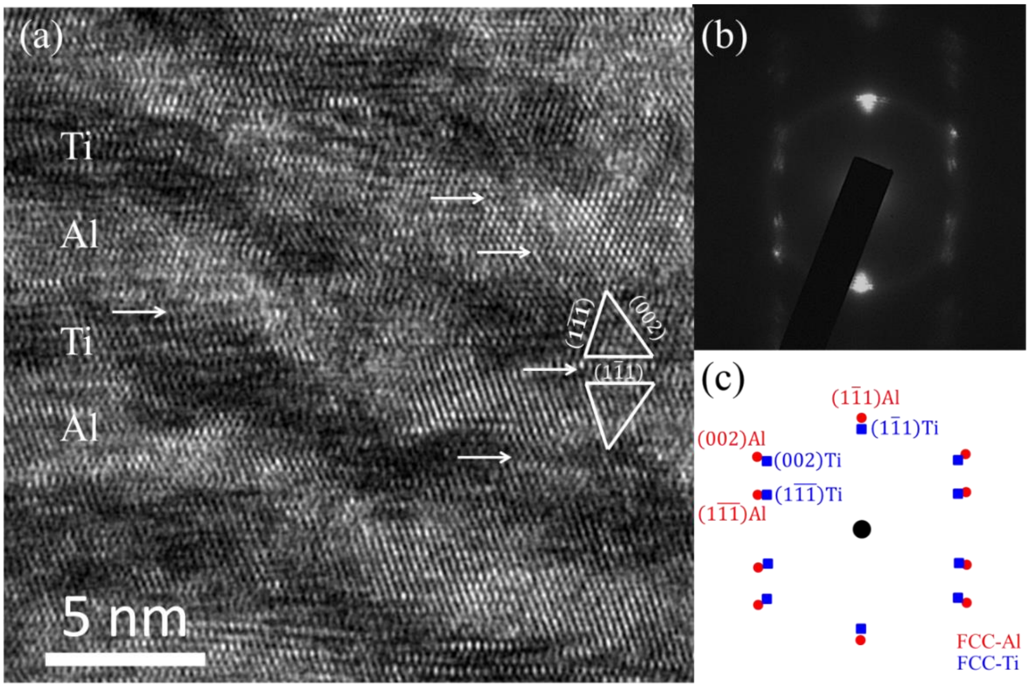

Figure 3.4 (a) HRTEM image of as-deposited AT2.5, (b) corresponding selected area diffraction of image (a), and (c) schematic of diffraction patterns from twinned fcc-Al and fcc-Ti along <1$\bar{1}$0> axis.

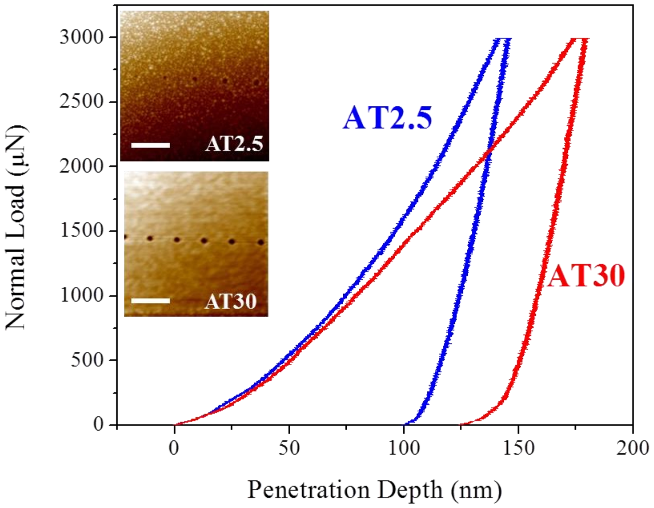

Figure 3.5 Typical nanoindentation load-displacement profiles of AT2.5 and AT30 under 3 mN load. Insets show surface topographies of the two samples after nanoindentation. Scale bar in both insets is 10 μm.

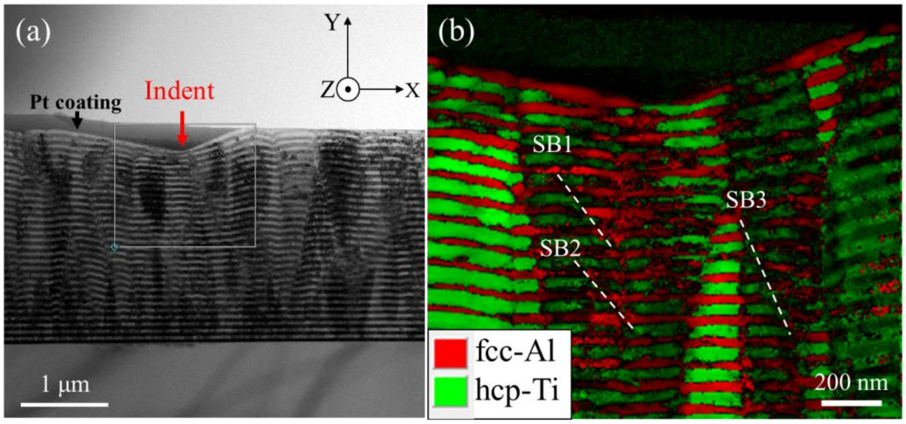

Figure 3.6 (a) Cross-sectional BF TEM image of AT 30 after nanoindentation, and (b) orientation phase map from box area in (a). Red and green in (b) represent the Al and Ti phases respectively.

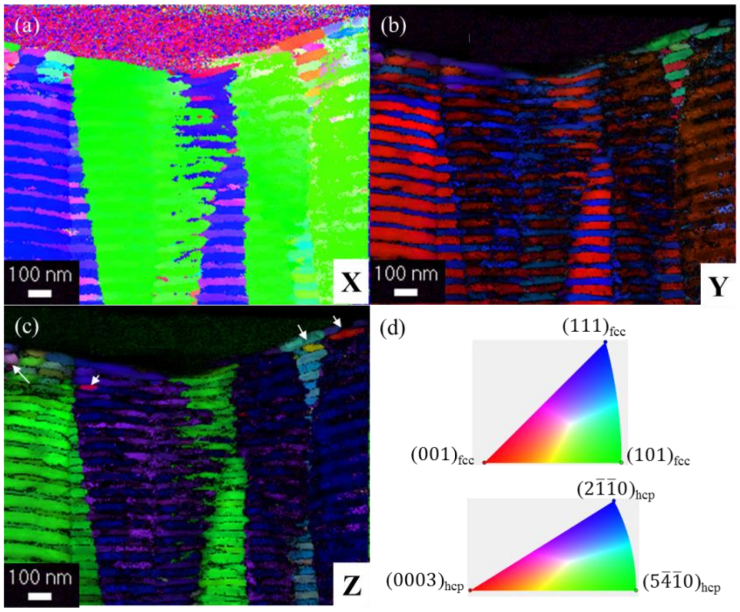

Figure 3.7 Orientation maps in (a) X, (b) Y, and (c) Z direction. This is as defined in Fig. 6(a) of AT30 after nanoindentation test. The orientations are color coded according to the triangle legend in (d).

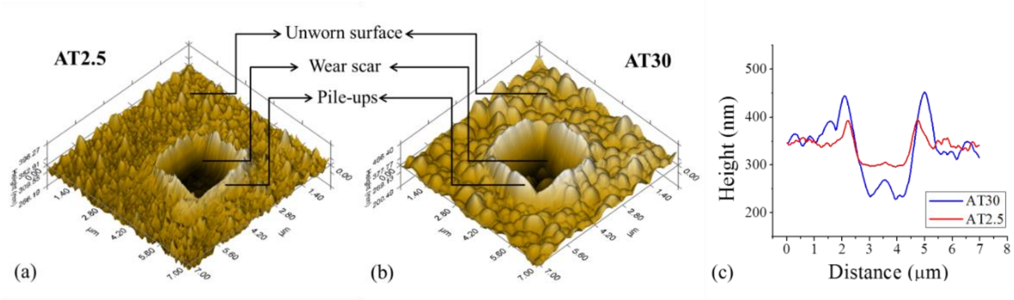

Figure 3.8 Surface topographies of (a) AT2.5 and (b) AT30 after 10 cycles of wear with 93 µN load. (c) Surface height profiles of samples AT2.5 and AT30 measured from images (a) and (b).

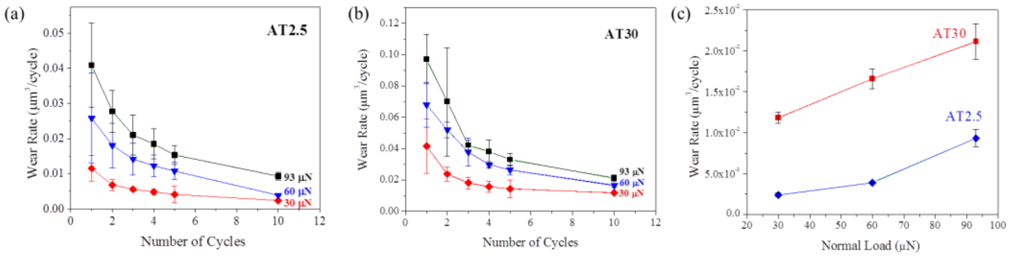

Figure 3.9 Wear rates as a function of number of cycles for samples (a) AT2.5 and (b) AT30. (c) Wear rates of AT2.5 and AT30 after 10 cycles of wear test under 30, 60 and 93 µN load.

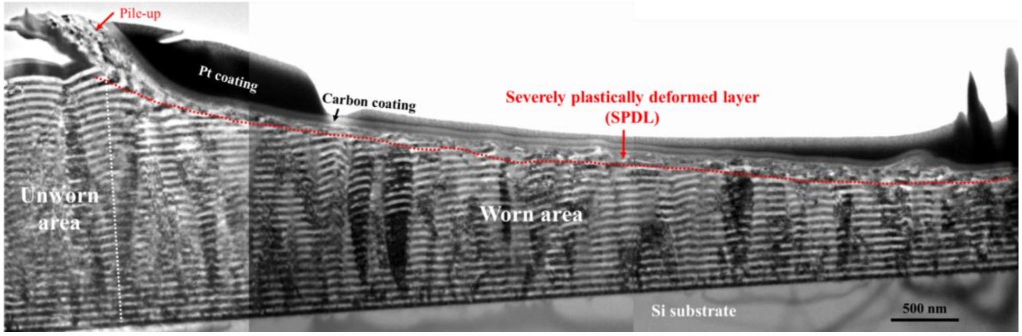

Figure 3.10 Montage BF TEM image of AT30 after 10 cycles of wear under 93 µN load. The wear scar area is 35 × 35 μm^2. The bright and dark contrast corresponds to the Al and Ti layers respectively. Carbon and Pt was used as protective coatings during TEM sample preparation using FIB.

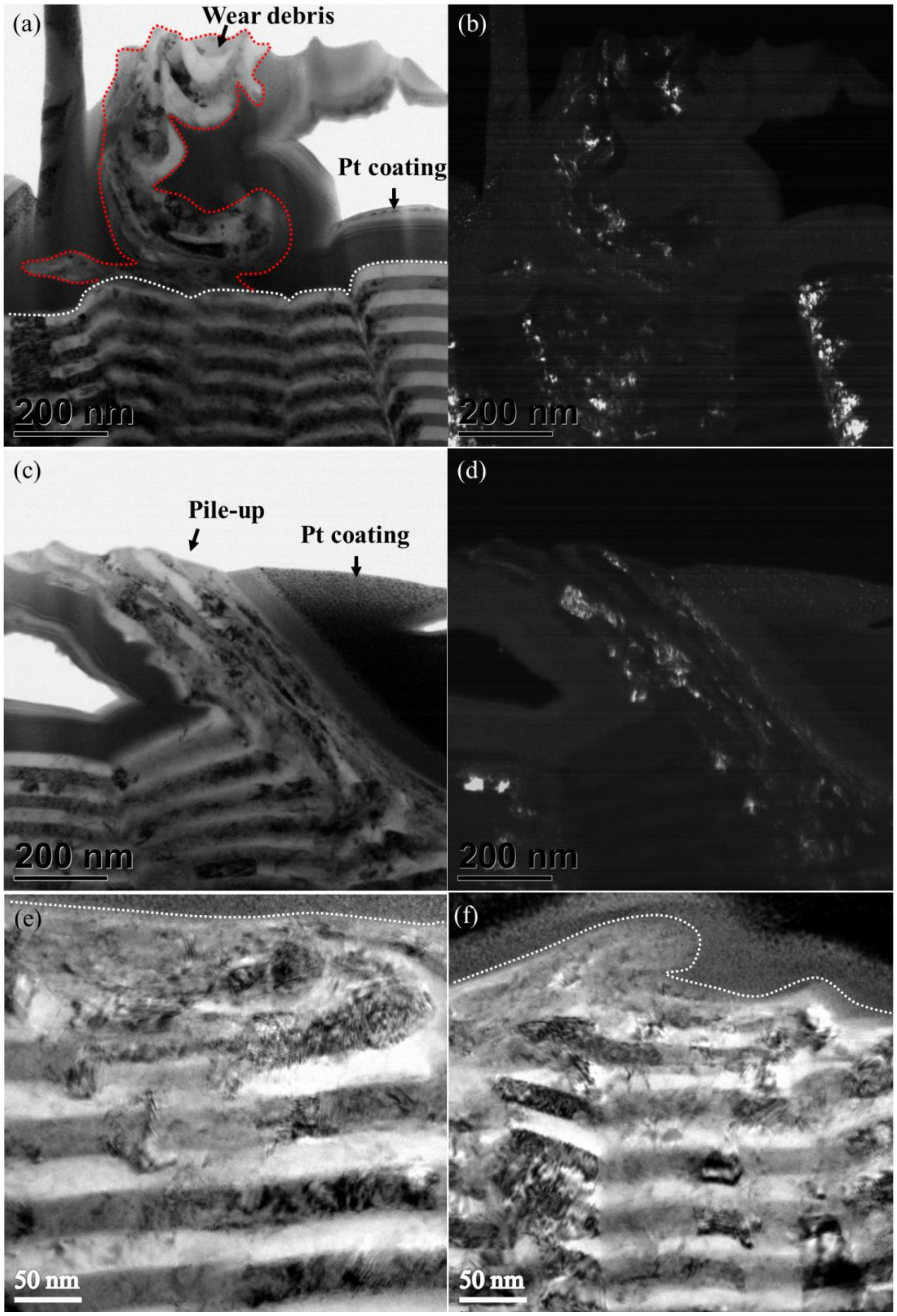

Figure 3.11 (a) BF, and (b) DF TEM images of a wear debris attached to the surface of AT30 after 10 cycles of wear under 93 μN load. White dashed lines represent the wear surface. (c) BF and (d) DF TEM images of pile-up, (e) and (f) BF TEM images of subsurface material from the same sample.

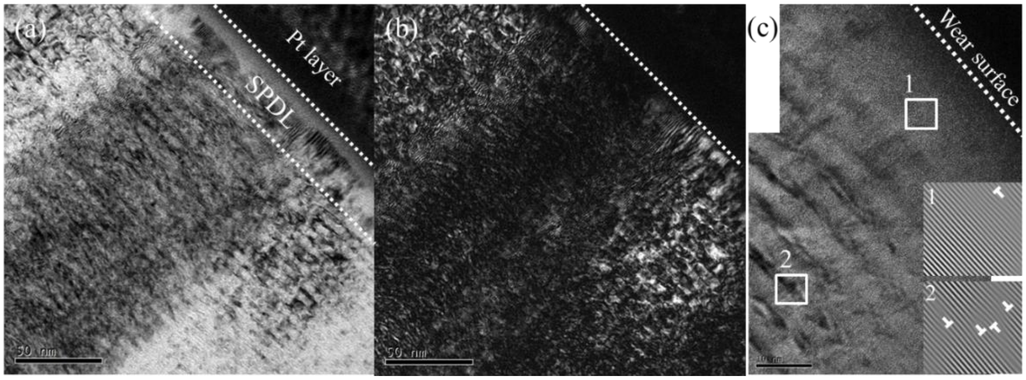

Figure 3.12 (a) BF, and (b) DF TEM images of AT2.5 after 10 cycles of wear under 93 μm load. (c) Montage HRTEM image from the SPDL (as indicated in (a)). The wear scar area is 35 × 35 μm^2. Dashed lines represent the wear surface. Insets 1 and 2 in (c) correspond to the IFFT of box area 1 and 2 respectively.

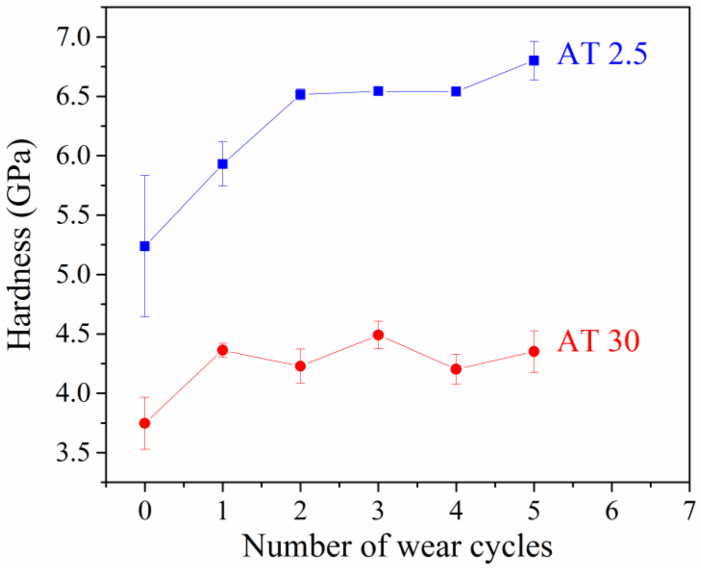

Figure 3.13 Nanoindentation hardness measured on wear scars (35 × 35 μm^2) of AT2.5 and AT30 after wear tests under 60 μN load up to five cycles.

CHAPTER 4: CORROSION PROPERTIES OF AL/TI NMMS

4.1 Introduction

Nanoscale Metallic Multilayer (NMM) coatings are widely used as protective layers because of their excellent mechanical and tribological properties [1-3]. One of the important issues which may limit applications of these coatings is how they corrode in different environments which have aggressive components such as chloride. A multilayer coating which demonstrates excellent wear resistance and high hardness but poor corrosion resistance is hardly useful for industrial applications in severe environment. Although aluminum coatings are often used as the cathodic protection of steel structures, their low mechanical performance is usually a drawback. To overcome this limitation, Creus et al. [4] has studied the effect of chrome alloying on the corrosion resistance of Al coatings. They found that an amorphous Al-Cr coating offers better corrosion resistance by limiting the galvanic corrosion of Al and steel. Li et al. [5] found that adding a second layer of AlN over a protective Al coating on NdFeB substrate could significantly decrease the corrosion rate by creating a denser structure in both layers with better metrology bounding between substrate and the overall coating. Similar to aluminum coatings, titanium is well known for its excellent corrosion resistance in chloride containing environments. In this study Al and Ti are used as two constituent phases in four nanoscale metallic multilayer (NMM) structures with individual layer thickness from 2.5 to 30 nm. The effect of microstructure on the corrosion resistance of these Al/Ti NMMs will be evaluated in simulated saline environment at room temperature [1, 2, 6, 7]. Aluminum and titanium have very similar electrode potential (-1.628 V for Ti^{2+} and -1.662 V for Al^{3+}) so galvanic corrosion between adjacent layers, which is the most likely type of corrosion in a multi metallic structure, may be limited. Crevice corrosion is unlikely to happen since the layer by layer structure was made through a vacuum process and similar phases are separated from each other with a layer of second phase (component). Finally, it is noted that pitting instead of uniform corrosion of Al/Ti NMMs is expected as the electrolyte was controlled at a pH ~7.

4.2 Experimental Procedure

Four Al/Ti NMMs with different individual layer thicknesses were deposited using direct current sputtering machine with Earton 8210 as the power supply. In each NMM, all layers (including both Al and Ti) had the same individual layer thickness. Samples were deposited on Si (100) wafers using aluminum and titanium S-gun toroidal with purities of 99.999%. Argon gas maintained the deposition chamber pressure at ~ 5 mTorr. A dicing tool from Micro Automation was used to cut the wafers into small pieces. Grazing incident X-ray diffraction (GIXRD) test was performed on all NMMs to confirm the crystal structure of as-deposited samples. Scanning electron microscopy (SEM, Hitachi SU-70) was used for surface characterization pre and post corrosion tests. Cross-section samples of NMMs were prepared using focus ion beam (FIB, FEI) and characterized using transmission electron microscopy (TEM, Tecnai 20). Hardness and module of elasticity were measured using Hysitron TI900 triboindenter with a standard Berkovich tip. At least four 1 × 1 cm^2 specimens from each NMM samples were utilized for the corrosion test. Each specimen went under several sealing steps before potentiodynamic test using heat shrink wrap, stop-off brazing aid and polyurethane M-Coat (Fig. 4.1. shows these steps toward specimen preparation). There was at least 24 hours gap between sealing specimens and potentiodynamic tests. NaCl in the form of powder was solved into deionized (DI) water to achieve 0.6 M solution at 25 °C. For consistency, all tests were performed using the same batch of a solution as the electrolyte. Standard NaCl reference electrode (CHI111) and mixed metal oxide coated titanium mesh counter electrode were implemented for this test. The corrosion cell was a non-conductive clear plastic or glass beaker. A camcorder was used to record any changes over the surface of samples in the whole examination procedures. Initial conditions potentiodynamic tool were defined as:

- Initial E (V) = - 0.25 - + 0.3
- Scan rate (mv/s) = 0.167
- Sample period (s) = 1
- Sample Area= different depending on samples sealing condition.
- Density (g/cm^3) = 3.6
- Equiv. wt= 11.9
- 0.6 M Nacl electrolyte

All specimens were immersed into 0.6 M NaCl solution for at least 1 hour before starting the test to reach a steady-state open circuit potential.

4.3 Results and Discussion

4.3.1 Morphology and Characterization of Al/Ti NMMs

Fig. 4.2 shows the TEM images from cross-sections of specimen A and D, which have the smallest and largest bilayer thickness of ~ 5 nm and ~ 60 nm respectively, among all samples investigated here (as listed in Table 4.1). Both samples show a coherent multilayer structure where the white and dark regions correspond to the aluminum and titanium phase in the multilayer structure respectively. Interfaces of two constituent phases are distinguishable, demonstrating a clear layer by layer structure. Cross section images also indicate the columnar structure of grains with epitaxial growth of layer, similar to that reported by Josell et al. [8]. The presence of titanium as the second phase reduced the overall columnar grain size of deposited layers which is a common behavior in monolithic aluminum growth [6, 9]. Figure 4.3 summarizes the arithmetic average of surface roughness (Ra) and grain size of all NMMs and monolithic samples. By decreasing the bilayer thickness from specimen D to B, both surface roughness and grain size are decreasing although the trend changes slightly from sample B to A where a small increase is observed.

Fig. 4.4 demonstrates the GIXRD patterns of all four Al/Ti NMMs. Silicon peak Si (311) coming from the substrates is visible at 57°. Strong fcc Al (220) at ~ 65° and hcp Ti (10.3) at ~ 70.6° were observed for sample B, C and D, indicating the main crystal structure content of these NMMs, while an overlap of Al (111)/ Ti (00.2) can be observed at 38.48° with relatively lower intensity compared to the other two peaks. GIXRD patterns from Specimen A, on the contrary, have a stronger overlapping of Al (111) and Ti (00.2) at 38.48° while it shows much weaker Al (220) and Ti (10.3). Nanoindentation results indicate that decreasing the individual layer thickness increases the NMM hardness; specimen A demonstrates the highest hardness of ~ 4.94 GPa while specimen D shows the smallest hardness of ~ 3.13 GPa. Table 4.1 summarizes the physical and mechanical properties of NMMs and monolithic specimen studied in this research.

4.3.2 Corrosion Behavior of Al/Ti NMMs

Mechanical properties, interface properties, porosity and microstructure will significantly affect NMMs corrosion rate [10]. For example, an inverse relationship has often been found between corrosion rate and porosity of NMMs. Figure 4.5 summarizes the typical potentiodynamic polarization curves of all NMMs as well as monolithic Al. It can be seen that, samples C and D with a bilayer thicknesses of ~ 22.8 nm and ~ 60 nm respectively, behaves similar to monolithic Al. For these samples, active corrosion starts right after E_{oc}, in the anodic region, with no signs of passivation. On the other hand, samples A and B, with individual layer thickness of 2.5 nm and 5.2 nm, exhibit much lower corrosion current density and well-defined passive region above open circuit potential, indicating a significant improvement of corrosion resistance and enhanced passivation ability of NMM at smaller layer thickness.

S.H. Ahn et al. [11] suggested five different types of corrosion in multilayers including pitting, galvanic and crevice corrosion, etc., among which, penetration of defects into coating was identified as the main reason for corrosion of multilayers. Several factors including pinholes, pores and other types of porosity of coating will significantly degrade corrosion resistance of multilayer coatings. Next all major possible types of corrosion in Al/Ti multilayers are discussed as following:

- Galvanic corrosion between coating and substrate: Since the silicon substrate will remain passive [12] through the whole electrochemical test, no significant galvanic coupling between substrates and coatings is expected to occur in the current study.
- Pitting corrosion: Pitting or localized corrosion was observed by polarization curves for samples B, C, D and monolithic aluminum. SEM images (Fig. 4.6) from specimen surface after potentiodynamic tests confirm the presence of pitting corrosion. No sign of pitting was observed in polarization curves (in the measured potential range) or post-test SEM images of sample A surface (Fig. 4.6).
- Crevice corrosion inside coating: this type of corrosion usually occurs when droplets, pores and pin holes are present in deposited coating. Based on the TEM analysis from the cross-section of multilayer there is no sign of droplets or pinholes in any of as-deposited NMM structures. Considering the deposition type (sputtering PVD) these observations were normal. Droplets and pin holes are typical of electron beam depositions [13]. Thus crevice

corrosion would unlikely be a primary reason for initiation of corrosion in the coating although it may later accelerate the corrosion process.

- Galvanic corrosion between adjacent layers of Al and Ti: considering standard hydrogen electrode (SHE) as the reference, aluminum and titanium have very similar electrode potential (-1.628 V for Ti^{2+} and -1.662 V for Al^{3+}). These two elements are coming right after each other in standard electrode potential table. On a study of Al/Ti multilayers deposited on NdFeB, T. Xie et al. [9] undermines the galvanic corrosion based on electro-potential of Al and Ti, but does not rule it out. These authors reported pitting as the primary reason for corrosion initiation in Al/Ti multilayers. In a different study Charrier et al. [14] reported galvanic corrosion in Al/Ti multilayers as one of the active types of corrosion in the electrochemical test. Based on SEM images after the tests and polarization curves, corrosion starts in the form of pitting and then will be followed by galvanic corrosion in samples B, C, and D. Creus et al. [6] showed that cavity depth, which is defined as the gap between interconnected nodules will accelerate corrosion. Cavity depth exposes several layers on top layers with electrolyte and its aggressive particles of Cl^- ions. Two phases of metal connected to each other and in contact with an electrolyte, is, in fact, a suitable situation for an occurrence of galvanic corrosion. To address the cavity depth issue, AFM scans were analyzed using the Nanoscope software. Deepest and highest spots over AFM image were located. A cross section profile which contained both spots was generated to determine maximum cavity depths. Table 4.2 summarizes the results from polarization tests along with the cavity depth in four Al/Ti NMMs. Considering the individual layer thickness of NMMs and their cavity depth, it can be concluded that there is a direct relation between bilayer thickness and amount of exposed cross section from two phases with electrolyte. Cavity depth could potentially assist galvanic corrosion. More analysis after corrosion tests using SEM indicates that in all tested sample, corrosion starts in the form of pitting. In multilayers, a galvanic coupling of layers can be spotted through delamination of layers after corrosion. This behavior was not observed initially in samples B, C and D but did finally happen after pitting corrosion. Based on polarization curves, the required time for occurrence of pitting were ~ 2,000 s, and ~ 3,400s for sample D and C respectively. The potentiodynamic test was stopped for half of the samples of each specimen right after detecting pitting corrosion. For the other half of samples, test was kept running until the limits of predefined conditions were reached. A camcorder capable of recording videos with up to 50X magnifications recorded hydrogen release from the surface of samples within 60 seconds of what polarization curves indicated. SEM images from surface of samples confirm the localized pitting corrosion. For the second half of samples which went through the complete test, samples corroded until the potentiostat tool reached its predefined parameters. For all samples (except for sample A), a complete corrosion over the entire surface was observed in less than 5 minutes after the first signs of pitting corrosion occurred. This rapid growth of corrosion along with delamination of layers can be attributed to the galvanic corrosion between adjacent Al and Ti layers, which was facilitated by pin holes and pits generated on the top Al layer. Such comprehensive corrosion in the form of layer delamination was similar to that reported in TiN/CrN multilayer by Nordin et al. [12]. EDS test was performed at the delaminated surfaces of specimen B and C right after the corrosion test. Additional EDS test was performed on the same location after removing the delaminated layers using a soft brush and compressed nitrogen. The results are shown in Fig. 4.8. Comparing the two EDS results reveals that corrosion and the delamination does not engage all the layers in the coating. Five abundant elements detected in the coating by EDS were Al, Ti, Si, Cl, Na and Oxygen. Comparing the second EDS results with the first one indicates that, all five components do exist over the same spot, only with slightly smaller intensity in the second EDS scan. Figure 4.8 indicates the EDS scans from a surface of sample C before and after removing the delamination. Full polarization curve of sample C (showed in Figure Fig. 4.9) indicates two steps of pitting corrosions in the anodic region. The first set of pitting defected top layers and eventually caused layers delamination by accelerating galvanic corrosion. The second set of pitting initiated beneath the delaminated layers and will engage the rest of intact layers.

Based on Tafel analysis specimen A and B demonstrated the best corrosion resistance. Specimen B with bilayer thickness of 10.4 nm had a corrosion current density (i_{corr}) of ~ 7.24 × 10^{-9} (A/cm^2) with an open circuit potential (V_{oc}) of ~ - 330 mV. Specimen A with ~ 5 nm bilayer thickness showed a corrosion current density of ~ 0.61 × 10^{-9} (A/cm^2) and open circuit potential of ~ -0.164 mV, suggesting an improvement in corrosion resistance by more than an orders of magnitude compared to pure Al. Sample A also demonstrated a much noble behavior through more positive V_{oc}. Creus et al. showed that Al/Cr multilayer with an overall thickness of ~ 7.9 µm, exhibit a corrosion current density of i_{corr} ~ 0.2 × 10^{-6} (A/cm^2) and V_{oc} ~ - 610 mV[6]. Both samples demonstrate much better corrosion resistance and noble behavior compared to Al/Cr multilayers [6]. Sample A and B also demonstrated superior corrosion properties compared to an Al/Ti multilayer with much higher overall thickness. For example, Charrier et al. [14] showed that Al/Ti multilayer with ~ 15 µm thickness resulted in a corrosion current density of ~ 0.2 × 10^{-6} (A/cm^2) and V_{oc} ~ - 715 mV.

4.3.3 Effect of Layer Thickness and Interfaces on Corrosion Resistance

Finally, we discuss the effect of layer thickness and total film thickness on the corrosion resistance of NMMs.

- Increasing the bilayer and overall thickness will not improve the corrosion rate. This can be simply concluded by comparing the results from current study with Charrier et al. work over a ~ 15 μm thick Al/Ti multilayer [14].
- Adding the number of interfaces is likely to decrease i_{corr} and increase $V_{oc.}$ In a test of Al/Ti NMMs, Xie et al. compared corrosion properties of two multilayers with 5 and 25 bilayers. Overall thickness of coating remained the same at ~ 4.6 μm. Polarization data showed that i_{corr} decreased from ~ 1.8×10^{-5} (A/cm^2) to ~ 7.9×10^{-8} (A/cm^2), while E_{corr} increased from -0.98 V to -0.81 V [9]. In the current study, specimen A, B, C and D had 374, 156, 136 and 60 layers respectively and the corrosion resistance was found to increase with the number of layers. Comparing the current study with those from Xie et al. and Charrier et al. suggests that increasing the overall number of layers (and consequently interfaces) favors an improvement in the corrosion properties. Adding more layers and hence more interfaces might assist blocking pores and defects in the coating, which will push the polarization curve toward more positive potentials. [6, 15] .
- Prior research shows that for precipitate containing alloys, precipitates smaller than ~ 4 nm becomes 'invisible' during corrosion, i.e. these fine precipitates will not form micro-galvanic coupling with the matrix [16], Thus the alloy behaves as if it were a chemically homogeneous alloy. In a very similar fashion, in the current study, when the individual layer thickness was below ~ 5 nm, an improved corrosion resistance was observed in the Al/Ti NMMs, as if the layer structure became invisible to corrosion. In this case, galvanic

coupling between adjacent Al and Ti layers, which contributes to the high corrosion rate in Al/Ti NMMs with larger layer thicknesses (samples B, C and D), was completely eliminated. Thus the present work suggests a novel way of enhancing corrosion resistance of NMMs via layer thickness control. In addition to enhanced mechanical and tribological properties at small layer thicknesses, these NMMs may be used as novel tribocorrosion resistant coatings for future applications in severe environment.

4.4 Conclusions

Corrosion resistance of four Al/Ti NMMs was examined through potentiodynamic corrosion test in simulated sea water. Corrosion starts in the form of pitting followed by galvanic corrosion between adjacent layers of NMMs with layer thickness above 2.5 nm. Samples A and B, which had the smallest individual layer thickness of 2.5 nm and 5.4 nm respectively and high amounts of interfaces demonstrated much better corrosion resistance compared to their counterparts (samples C and D). Based on the observations in the current study, the presence of large population of interfaces and the ultra-fine layer thickness in samples A and B could be the main reason for blocking the aggressive ions path through coating [10, 17]. Higher amount of interfaces and refined layer thickness, which were proven to be improving mechanical properties of NMMs by controlling dislocations [18, 19], will also act as a barrier to block pores and defects and ultimately enhance corrosion resistance. The presented approach offers an opportunity to create novel NMMs with high specific strength, excellent tribological and corrosion resistance, which may find potential applications as tribocorrosion resistant coatings for metals in complex service conditions.

4.5 References

1. Chen, Y., et al., *Microstructure and strengthening mechanisms in Cu/Fe multilayers.* Acta Materialia, 2012. **60**(18): p. 6312-6321.

2. Ham, B. and X. Zhang, *High strength Mg/Nb nanolayer composites.* Materials Science and Engineering: A, 2011. **528**(4–5): p. 2028-2033.

3. Liu, Y., et al., *Mechanical properties of highly textured Cu/Ni multilayers.* Acta Materialia, 2011. **59**(5): p. 1924-1933.

4. Creus, J., A. Billard, and F. Sanchette, *Corrosion behaviour of amorphous Al–Cr and Al–Cr–(N) coatings deposited by dc magnetron sputtering on mild steel substrate.* Thin Solid Films, 2004. **466**(1–2): p. 1-9.

5. Li, J., et al., *AlN/Al dual protective coatings on NdFeB by DC magnetron sputtering.* Journal of Magnetism and Magnetic Materials, 2009. **321**(22): p. 3799-3803.

6. Creus, J., et al., *Mechanical and corrosion properties of dc magnetron sputtered Al/Cr multilayers.* Surface and Coatings Technology, 2008. **202**(16): p. 4047-4055.

7. Fu, E.G., et al., *Mechanical properties of sputtered Cu/V and Al/Nb multilayer films.* Materials Science and Engineering: A, 2008. **493**(1–2): p. 283-287.

8. Josell, D., et al., *Tensile testing low density multilayers: Aluminum/titanium.* Journal of Materials Research, 1998. **13**(10): p. 2902-2909.

9. Xie, T., et al., *Structure, corrosion, and hardness properties of Ti/Al multilayers coated on NdFeB by magnetron sputtering.* Vacuum, 2012. **86**(10): p. 1583-1588.

10. Guan, X., et al., *Toward high load bearing capacity and corrosion resistance Cr/Cr2N nano-multilayer coatings against seawater attack.* Surface and Coatings Technology, 2015. **282**: p. 78-85.

11. Ahn, S.H., et al., *Localized corrosion mechanisms of the multilayered coatings related to growth defects.* Surface and Coatings Technology, 2004. **177–178**: p. 638-644.

12. Nordin, M., M. Herranen, and S. Hogmark, *Influence of lamellae thickness on the corrosion behaviour of multilayered PVD TiN/CrN coatings.* Thin Solid Films, 1999. **348**(1–2): p. 202-209.

13. Wang, H.W., et al., *The corrosion behaviour of macroparticle defects in arc bond-sputtered CrN/NbN superlattice coatings.* Surface and Coatings Technology, 2000. **126**(2–3): p. 279-287.

14. Charrier, C., et al., *Aluminium and Ti/Al multilayer PVD coatings for enhanced corrosion resistance.* Surface and Coatings Technology, 1997. **90**(1–2): p. 29-34.

15. Kirilova, I., I. Ivanov, and S. Rashkov, *Anodic behaviour of composition modulated Zn-Co multilayers electrodeposited from single and dual baths*.

16. Ralston, K.D., et al., *The effect of precipitate size on the yield strength-pitting corrosion correlation in Al–Cu–Mg alloys.* Acta Materialia, 2010. **58**(18): p. 5941-5948.

17. Song, G.-H., et al., *The corrosive behavior of Cr/CrN multilayer coatings with different modulation periods.* Vacuum, 2013. **89**: p. 136-141.

18. Misra, A., R.G. Hoagland, and H. Kung ‡, *Thermal stability of self-supported nanolayered Cu/Nb films.* Philosophical Magazine, 2004. **84**(10): p. 1021-1028.

19. Misra, A. and H. Krug, *Deformation Behavior of Nanostructured Metallic Multilayers.* Advanced Engineering Materials, 2001. **3**(4): p. 217-222.

4.6 Tables and Figures

Table 4.1 Summary of structure and mechanical properties of Al/Ti NMMs.

NMM specimen	Individual layer thickness (nm)	Total film thickness (nm)	H (GPa)	E_r (Gpa)	Er/H
A	2.5 ± 0.3	930	4.94 ± 0.44	120.14 ± 7.56	24.32
B	5.2 ± 0.6	820	4.85 ± 0.28	117.57 ± 2.91	24.24
C	11.4 ± 1.1	1566	4.16 ± 0.49	112.89 ± 7.97	27.14
D	30 ± 1.5	1800	3.13 ± 0.43	109.99 ± 7.22	35.14

Table 4.2 Polarization curves extracted data along with cavity depth extracted from AFM analysis.

NMM specimen	population of interfaces in coating #	Individual layer thickness (nm)	maximum cavity depth (nm)	i_{corr} (nA/cm2)	Voc (V)
A	374	2.5 ± 0.3	40	0.61 ± 0.5	- 0.164 ± 0.017
B	156	5.2 ± 0.6	36	7.24 ± 1.0	- 0.330 ± 0.014
C	136	11.4 ± 1.1	67	62.16 ± 54.0	- 0.393 ± 0.167
D	60	30 ± 1.5	133	105.37 ± 5.6	- 0.484 ± 0.015

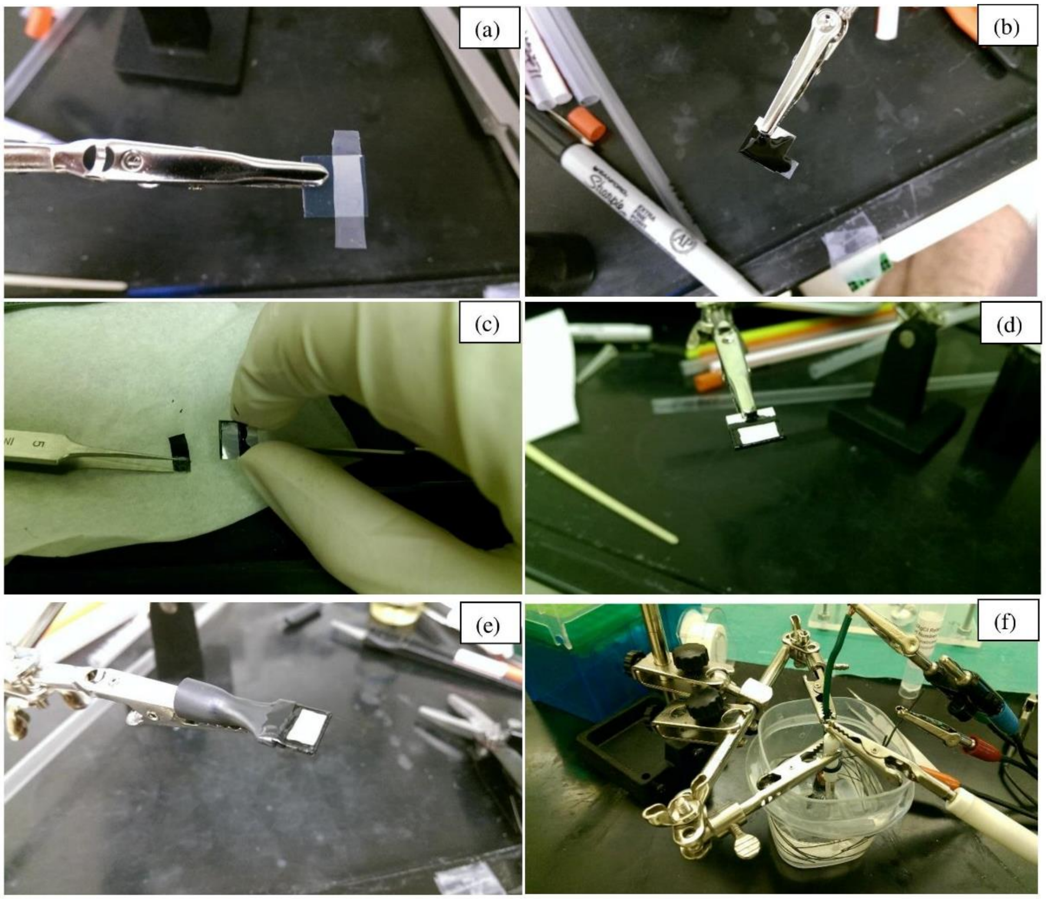

Figure 4.1 Sample preparation steps prior to corrosion testing. a) Covering specimen surface using an adhesive tape to separate it from sealing materials. b) Applying sealing material over sample surface using a small brush. c) Removing the tape from sample surface after curing of sealing material for 24 hours. d) Adding more sealing materials around the target surface and waiting another 24 hours for sealing to dry. e) Using heat shrink material to exclude the surface of corrosion from electrodes connectors and applying M-Bond adhesive and sealing material several times. f) Test environment showing reference electrode, corrosion cell, sample and other components.

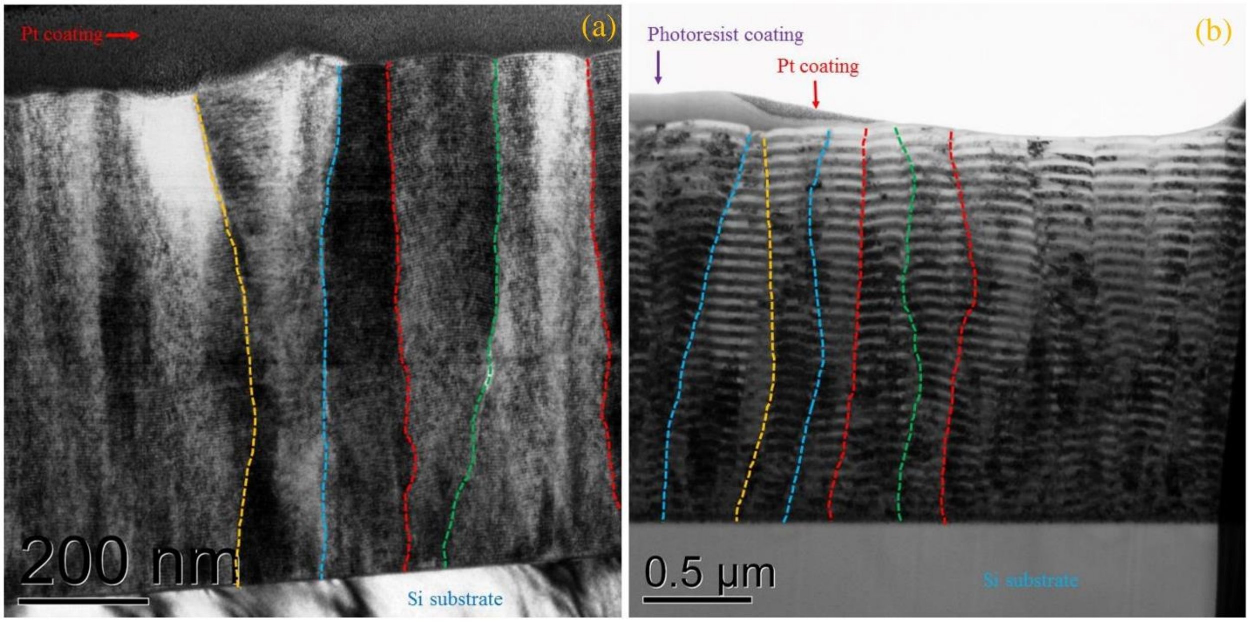

Figure 4.2 (a) and (b) low magnification TEM images from modulation structure of sample A and D respectively. Columnar grain boundaries are highlighted using yellow dash lines showing the through thickness grain size remains almost constant (i.e. there is no increase or decrease in grains size going from substrate to surface). (b) and (d) HR-TEM images of specimens A and D respectively.

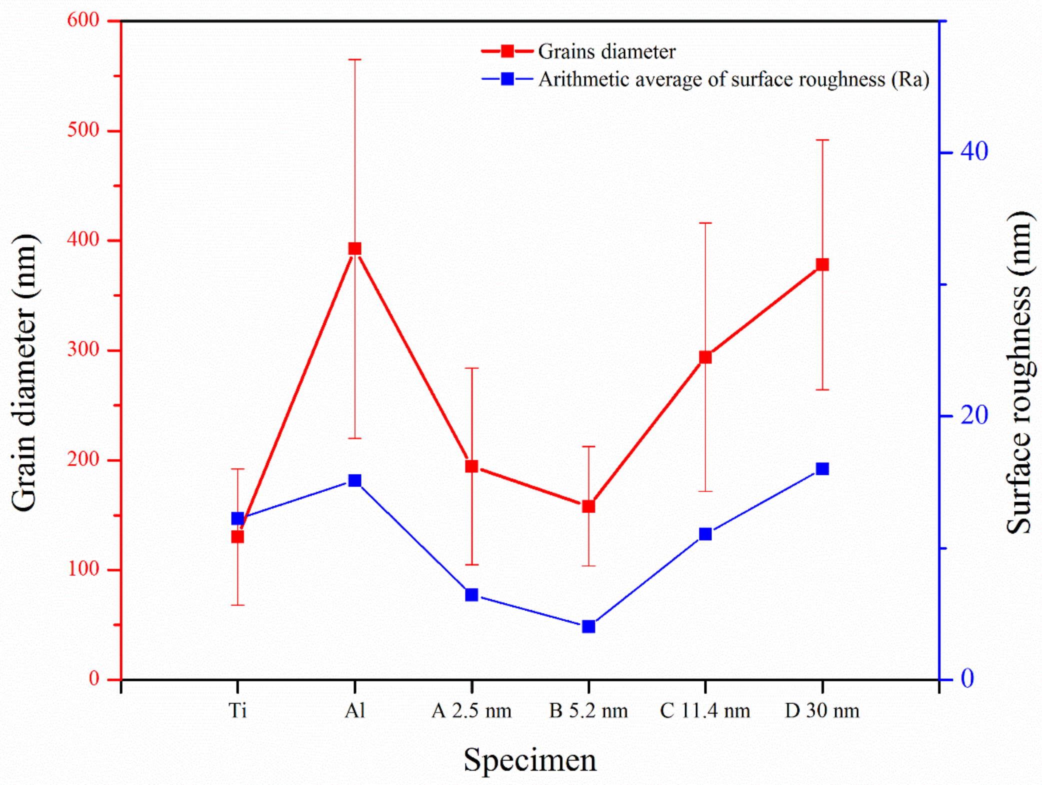

Figure 4.3 Columnar grains diameter and arithmetic average of surface roughness (Ra) extracted from AFM height images by averaging 100 data points extracted from 5 × 5 μm^2 scans. Monolithic aluminum and titanium specimens are also included for comparison.

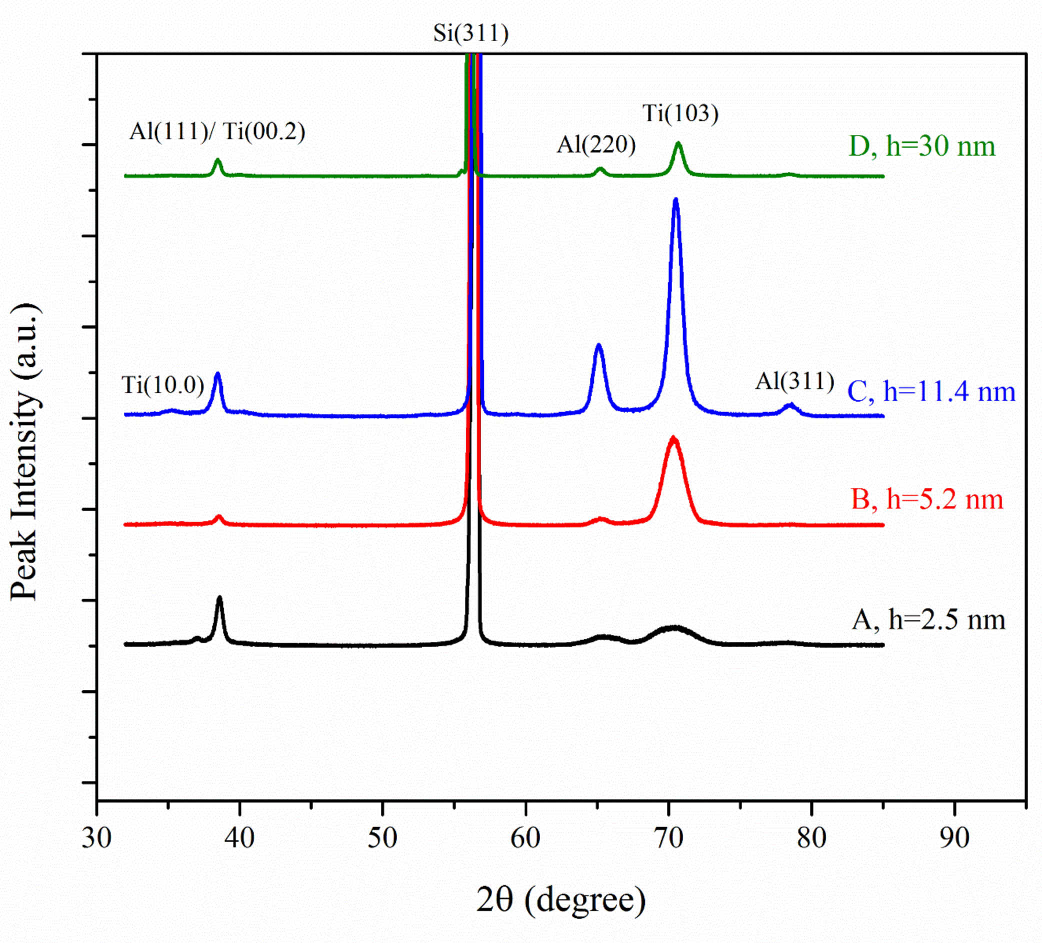

Figure 4.4 GIXRD diffracted patterns for all Al/Ti NMMs.

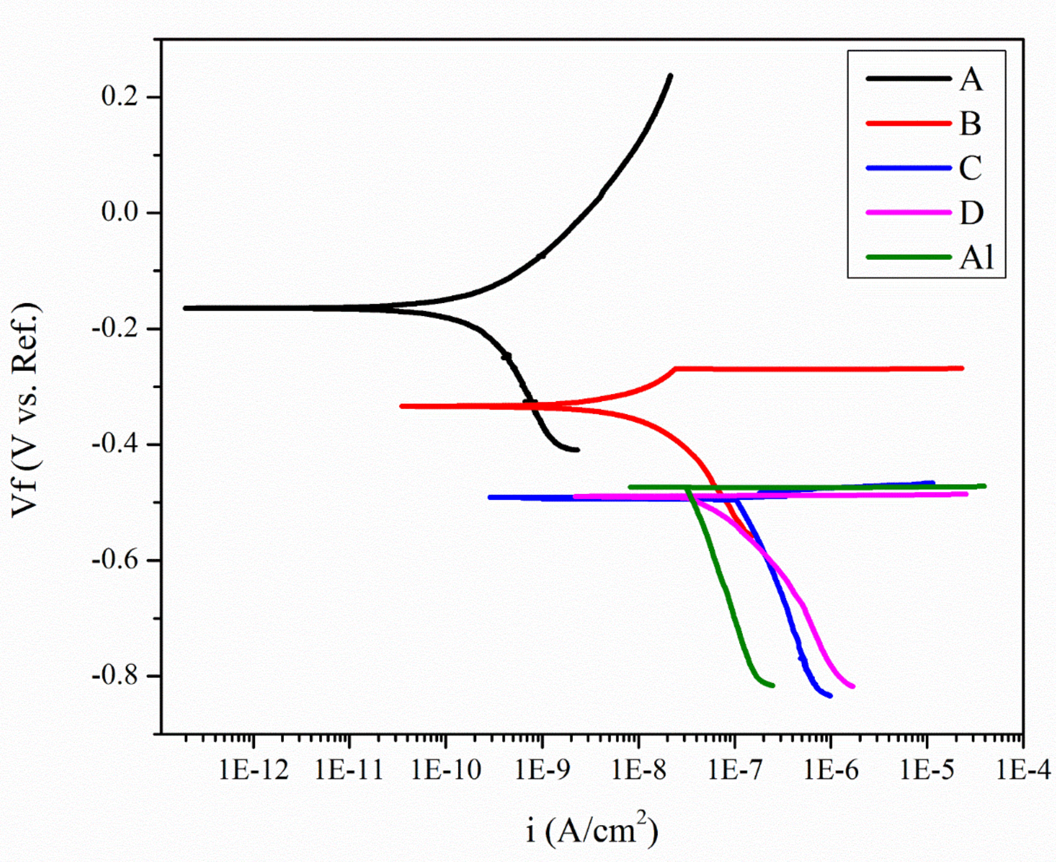

Figure 4.5 Polarization curves for specimen A, B, C, D and monolithic Al, generated using Gamry Echem Analyst software.

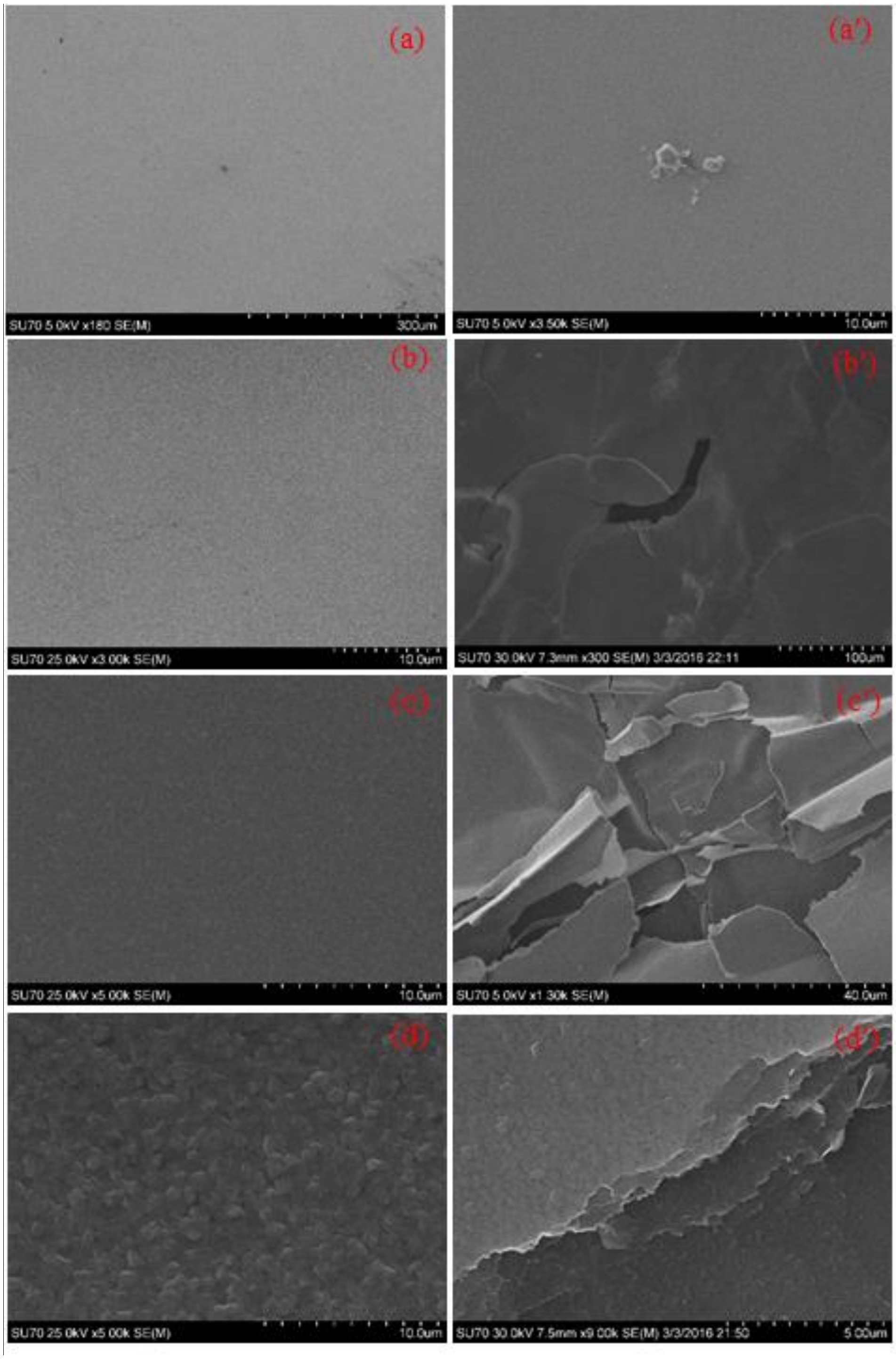

Figure 4.6 On the left side a, b, c and d indicate SEM image from surface of sample A, B, C and D before potentiodynamic test. On the right a′, b′, c′ and d′ demonstrate the samples surface after potentiodynamic tests.

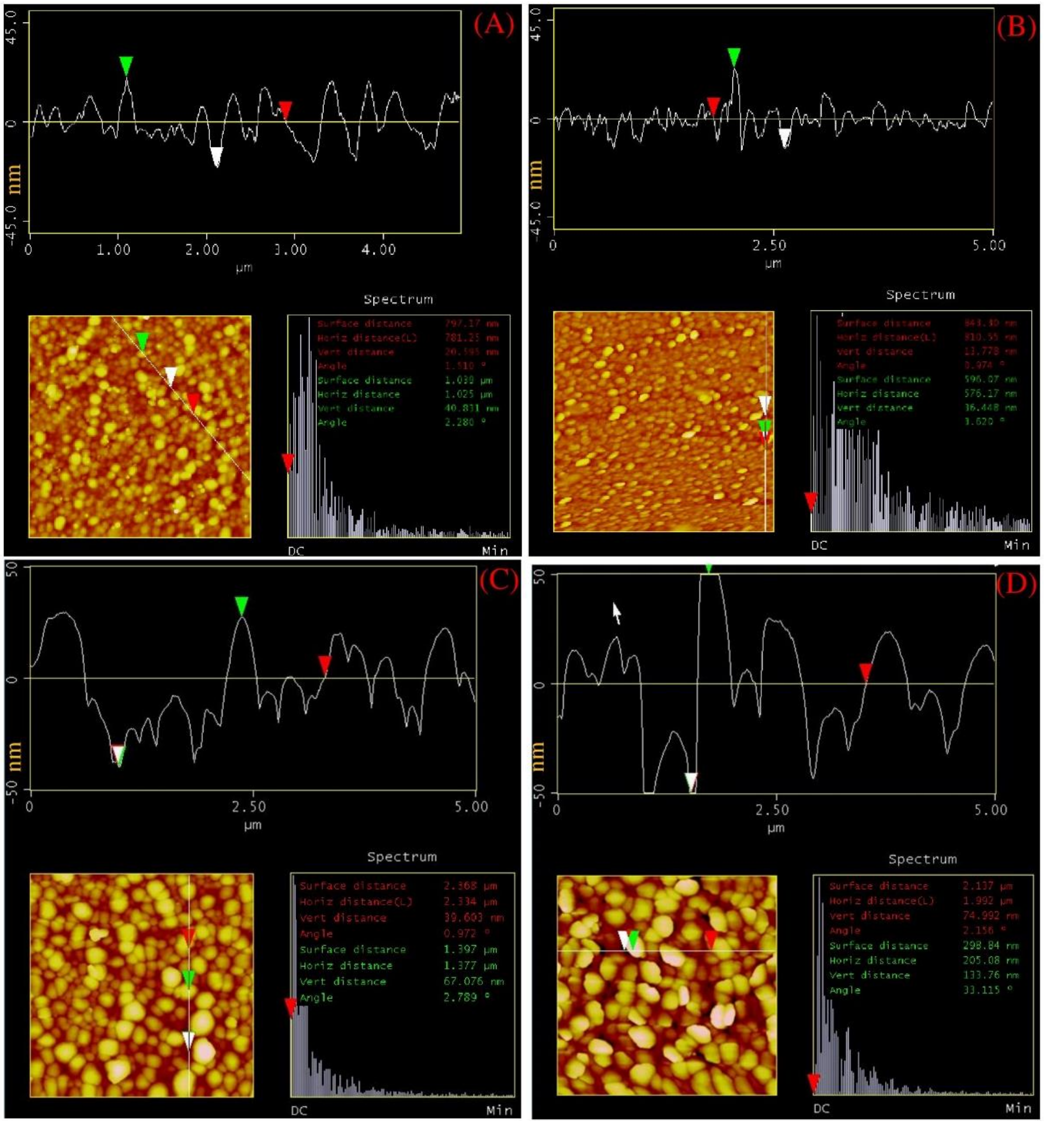

Figure 4.7 AFM images of Al/Ti NMMs. Line cross section profiles were used to measure the depths between surface nodules. Green arrows indicate the highest peaks, white (overlap of green and red) arrows demonstrate the deepest valleys and red arrows index the neutral level.

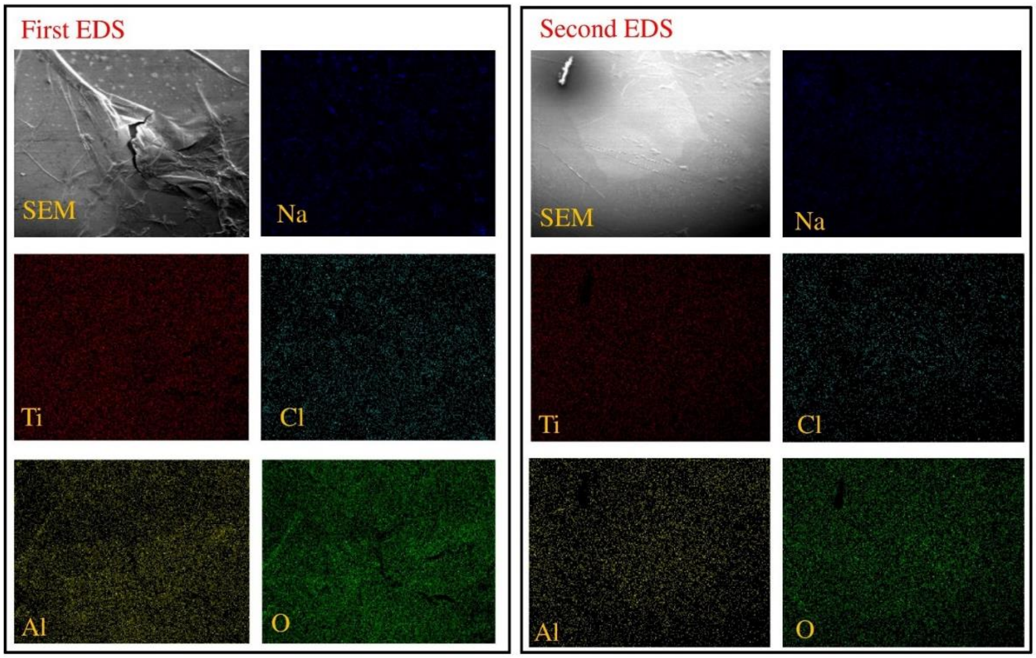

Figure 4.8 EDS analyses of sample C right after potentiodynamic test (left box) and after removing the delamination (right box). Both images are taken from the same location.

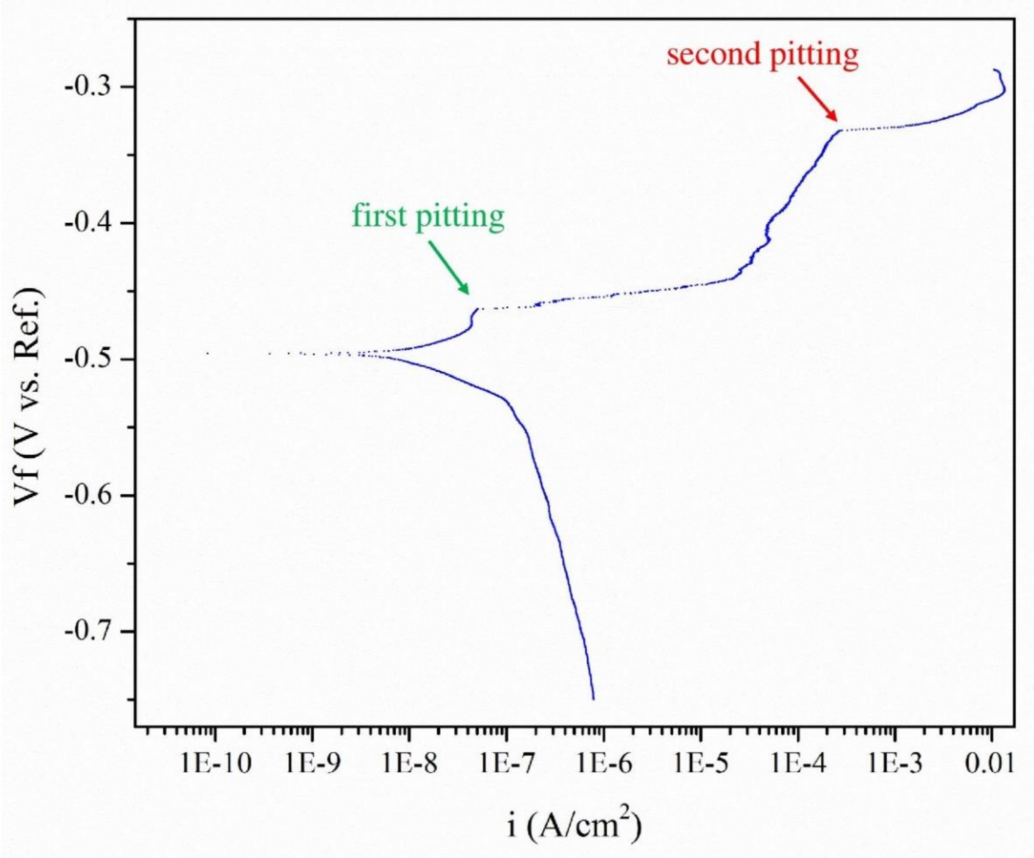

Figure 4.9 Polarization curve for sample C.

APPENDIX A: COPYRIGHT PERMISSIONS

A.1 Copyright Permission for Figure 1.1

3/31/2016 RightsLink Printable License

ELSEVIER LICENSE
TERMS AND CONDITIONS

Mar 31, 2016

This is a License Agreement between sina izadi ("You") and Elsevier ("Elsevier") provided by Copyright Clearance Center ("CCC"). The license consists of your order details, the terms and conditions provided by Elsevier, and the payment terms and conditions.

All payments must be made in full to CCC. For payment instructions, please see information listed at the bottom of this form.

Supplier	Elsevier Limited The Boulevard,Langford Lane Kidlington,Oxford,OX5 1GB,UK
Registered Company Number	1982084
Customer name	sina izadi
Customer address	2916 network place LUTZ, FL 33559
License number	3839261258661
License date	Mar 31, 2016
Licensed content publisher	Elsevier
Licensed content publication	Acta Materialia
Licensed content title	Length-scale-dependent deformation mechanisms in incoherent metallic multilayered composites
Licensed content author	A. Misra,J.P. Hirth,R.G. Hoagland
Licensed content date	October 2005
Licensed content volume number	53
Licensed content issue number	18
Number of pages	8
Start Page	4817
End Page	4824
Type of Use	reuse in a thesis/dissertation
Portion	figures/tables/illustrations
Number of figures/tables/illustrations	1
Format	both print and electronic
Are you the author of this Elsevier article?	No
Will you be translating?	No
Title of your thesis/dissertation	Al/Ti Nanostructured Multilayers: from Mechanical, Tribological, to Corrosion Properties
Expected completion date	Apr 2016
Estimated size (number of pages)	99
Elsevier VAT number	GB 494 6272 12
Permissions price	0.00 USD
VAT/Local Sales Tax	0.00 USD / 0.00 GBP
Total	0.00 USD
Terms and Conditions	

A.2 Copyright Permission for Figure 1.2

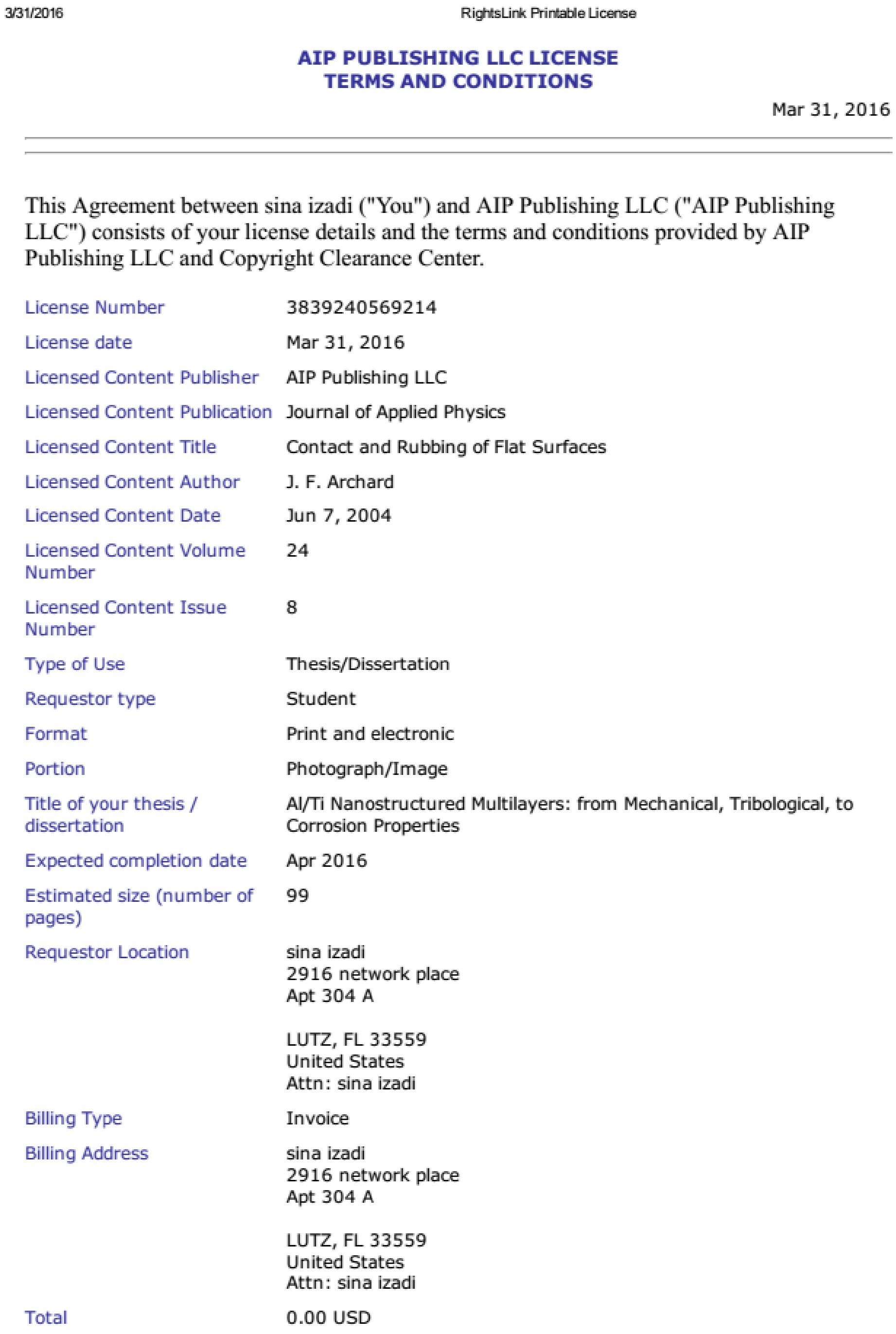

3/31/2016 RightsLink Printable License

AIP PUBLISHING LLC LICENSE
TERMS AND CONDITIONS

Mar 31, 2016

This Agreement between sina izadi ("You") and AIP Publishing LLC ("AIP Publishing LLC") consists of your license details and the terms and conditions provided by AIP Publishing LLC and Copyright Clearance Center.

License Number	3839240569214
License date	Mar 31, 2016
Licensed Content Publisher	AIP Publishing LLC
Licensed Content Publication	Journal of Applied Physics
Licensed Content Title	Contact and Rubbing of Flat Surfaces
Licensed Content Author	J. F. Archard
Licensed Content Date	Jun 7, 2004
Licensed Content Volume Number	24
Licensed Content Issue Number	8
Type of Use	Thesis/Dissertation
Requestor type	Student
Format	Print and electronic
Portion	Photograph/Image
Title of your thesis / dissertation	Al/Ti Nanostructured Multilayers: from Mechanical, Tribological, to Corrosion Properties
Expected completion date	Apr 2016
Estimated size (number of pages)	99
Requestor Location	sina izadi 2916 network place Apt 304 A LUTZ, FL 33559 United States Attn: sina izadi
Billing Type	Invoice
Billing Address	sina izadi 2916 network place Apt 304 A LUTZ, FL 33559 United States Attn: sina izadi
Total	0.00 USD

A.3 Copyright Permission for Figure 1.3

3/31/2016 RightsLink Printable License

ELSEVIER LICENSE
TERMS AND CONDITIONS

Mar 31, 2016

This is a License Agreement between sina izadi ("You") and Elsevier ("Elsevier") provided by Copyright Clearance Center ("CCC"). The license consists of your order details, the terms and conditions provided by Elsevier, and the payment terms and conditions.

All payments must be made in full to CCC. For payment instructions, please see information listed at the bottom of this form.

Supplier	Elsevier Limited The Boulevard,Langford Lane Kidlington,Oxford,OX5 1GB,UK
Registered Company Number	1982084
Customer name	sina izadi
Customer address	2916 network place
	LUTZ, FL 33559
License number	3839270094472
License date	Mar 31, 2016
Licensed content publisher	Elsevier
Licensed content publication	Thin Solid Films
Licensed content title	Corrosion behavior of nanolayered TiN/NbN multilayer coatings prepared by reactive direct current magnetron sputtering process
Licensed content author	Harish C Barshilia,M Surya Prakash,Aithu Poojari,K.S Rajam
Licensed content date	22 July 2004
Licensed content volume number	460
Licensed content issue number	1-2
Number of pages	10
Start Page	133
End Page	142
Type of Use	reuse in a thesis/dissertation
Intended publisher of new work	other
Portion	figures/tables/illustrations
Number of figures/tables/illustrations	1
Format	both print and electronic
Are you the author of this Elsevier article?	No
Will you be translating?	No
Title of your thesis/dissertation	Al/Ti Nanostructured Multilayers: from Mechanical, Tribological, to Corrosion Properties
Expected completion date	Apr 2016
Estimated size (number of pages)	99
Elsevier VAT number	GB 494 6272 12
Permissions price	0.00 USD
VAT/Local Sales Tax	0.00 USD / 0.00 GBP
Total	0.00 USD

A.4 Copyright Permission for Previously Published Materials in Chapter 3

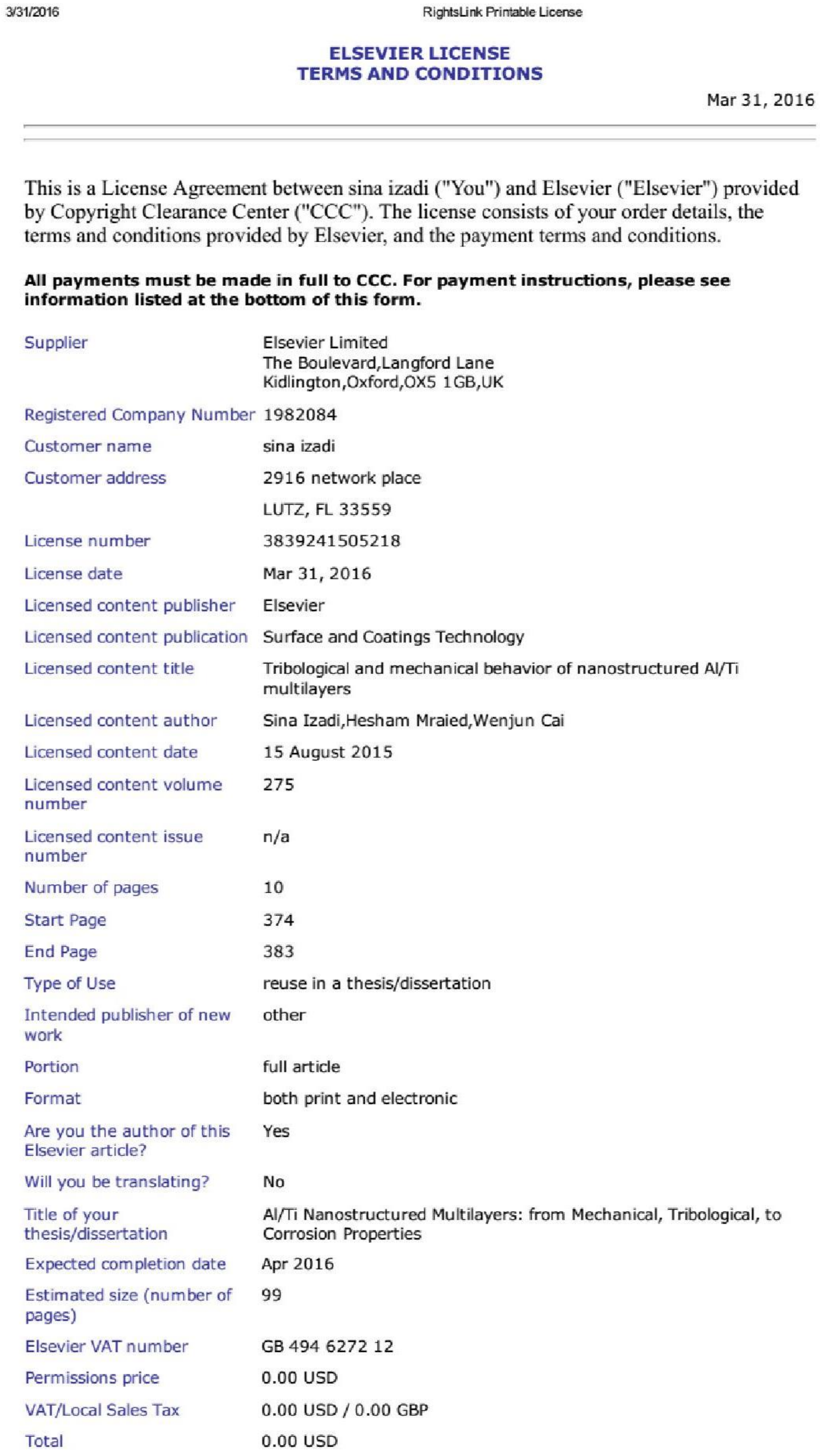

3/31/2016 RightsLink Printable License

ELSEVIER LICENSE
TERMS AND CONDITIONS

Mar 31, 2016

This is a License Agreement between sina izadi ("You") and Elsevier ("Elsevier") provided by Copyright Clearance Center ("CCC"). The license consists of your order details, the terms and conditions provided by Elsevier, and the payment terms and conditions.

All payments must be made in full to CCC. For payment instructions, please see information listed at the bottom of this form.

Supplier	Elsevier Limited The Boulevard,Langford Lane Kidlington,Oxford,OX5 1GB,UK
Registered Company Number	1982084
Customer name	sina izadi
Customer address	2916 network place
	LUTZ, FL 33559
License number	3839241505218
License date	Mar 31, 2016
Licensed content publisher	Elsevier
Licensed content publication	Surface and Coatings Technology
Licensed content title	Tribological and mechanical behavior of nanostructured Al/Ti multilayers
Licensed content author	Sina Izadi,Hesham Mraied,Wenjun Cai
Licensed content date	15 August 2015
Licensed content volume number	275
Licensed content issue number	n/a
Number of pages	10
Start Page	374
End Page	383
Type of Use	reuse in a thesis/dissertation
Intended publisher of new work	other
Portion	full article
Format	both print and electronic
Are you the author of this Elsevier article?	Yes
Will you be translating?	No
Title of your thesis/dissertation	Al/Ti Nanostructured Multilayers: from Mechanical, Tribological, to Corrosion Properties
Expected completion date	Apr 2016
Estimated size (number of pages)	99
Elsevier VAT number	GB 494 6272 12
Permissions price	0.00 USD
VAT/Local Sales Tax	0.00 USD / 0.00 GBP
Total	0.00 USD